CrystEngComm

HIGHLIGHT

View Article Online
View Journal | View Issue

Cite this: *CrystEngComm*, 2014, **16**, 10332

Hybrid vanadates constructed from extended metal–organic arrays: crystal architectures and properties

Roberto Fernández de Luis,[ab] Joseba Orive,[a] Edurne S. Larrea,[a] M. Karmele Urtiaga[a] and María I. Arriortua*[ab]

Received 14th March 2014,
Accepted 8th September 2014

DOI: 10.1039/c4ce00532e

www.rsc.org/crystengcomm

The hybrid vanadates exhibit structural archetypes between the hybrid zeotypes, in which the inorganic framework is surrounding an organic cation acting as a template, and metal–organic frameworks whose crystal structures are constructed from metal nodes or clusters linked by organic bridges. Here we present the summary of the studies carried out on hybrid vanadates constructed from extended metal–organic arrays. The crystal structures are systematically described and classified according to the dimensionality of the inorganic and metal–organic frameworks. Finally, the magnetic, thermal and catalytic properties of different structural archetypes are discussed.

Introduction

The research on the area of open framework materials has progressively become an important field since the discovery of the stilbite mineral by Crönstedt and the synthesis of artificial zeolites by Barrer and Milton.[1] Later, Flanigen *et al.* proposed the substitution $Si^{4+} \rightarrow Al^{3+} + P^{5+}$, opening a new route to synthesize microporous aluminophosphates.[2] Since these pioneering studies, the search for open framework materials has extended to other anions, such as oxyfluoride, phosphite,[3] arsenate, germanate,[4] sulphate, and sulphite, among others.[5] The crystal structures of these compounds are generally formed by the combination of tetrahedral or pseudotetrahedral oxoanions and transition metals in six, five or four coordination polyhedra, sharing vertices between them. Usually, organic amine molecules are used as templates, structure directing agents, or space fillers,

[a] *Departamento de Mineralogía y Petrología, Facultad de Ciencia y Tecnología, Universidad del País Vasco (UPV/EHU), Apdo. 644, 48080 Bilbao, Spain. Fax: +34 946 013 500; Tel: +34 946 015 984*
[b] *BCMaterials (Basque Centre for Materials, Applications & Nanostructures), Technological Park of Zamudio, Camino de Ibaizabal, Bndg. 500-1st, 48160, Derio, Spain. E-mail: roberto.fernandez@ehu.es, edurne.serrano@ehu.es, joseba.orive@ehu.es, karmele.urtiaga@ehu.es, maribel.arriortua@ehu.es*

Roberto Fernández de Luis

Roberto Fernández de Luis got his PhD (Materials Science, 2009) from the University of the Basque Country. His research is focused on crystal structure determination and thermal stability of the crystal frameworks after the loss and uptake of guest and coordinated species. For these studies, he has specialized on single crystal and powder X-ray diffraction at non-ambient temperature. During the last three years, as a postdoctoral research associate to the Crystallography group at the UPV/EHU, he has focused his work on the room temperature and hydrothermal synthesis of nanostructured hydrogels of silver vanadium oxides for battery applications.

Joseba Orive

Joseba Orive got both his BSc (Geology, 2005) and PhD (Materials Science, 2011) from the UPV/EHU, where he works as a postdoctoral research associate to the Crystallography group. His thesis work was focused on the search for materials with new structural archetypes with potential technological applications, involving the structural resolution of complex systems, in both powder and single crystal forms, and the analysis of the spectroscopic, luminescence, magnetic, and catalytic properties of new transition metal compounds. He is currently interested in new systems of inorganic–organic hybrid materials for electrochemical applications.

enhancing the interaction with the inorganic framework and increasing the thermodynamic stability of the hybrid compounds through the establishment of hydrogen bonds, van der Waals and/or other weak interactions. One of the barriers that hinder the synthesis of real porous materials from these inorganic–organic zeotypes is the fact that the anionic skeleton often collapses during the extraction of the cationic template, owing to the strong electrostatic host–guest interactions, which energetically represent an important contribution to the lattice energy.

The present interest is focused on the construction of metal–organic frameworks (MOFs) through the combination of rigid polyhedral secondary building units of metal ions or clusters connected by organic ligands. There are other auxiliary components, such as blocking ligands, counteranions, and non-bonding guests or template molecules. The structures and properties of coordination polymers can be well-designed and systematically tuned by the judicious choice of metal-based building blocks and organic linkers, in principle.[6]

This work is focused on hybrid vanadates (here and after, HV), a family of inorganic–organic materials sharing structural characteristics of MOFs and zeolite-type compounds. HV combines vanadium oxide-based structural units with discrete or polymeric metal–organic subunits. In the first studies on HV, the use of chelating amines avoided the increase in the framework dimensionality through metal–ligand–metal links. Thus the discrete metal–organic units were linked through the vanadium oxide subunits (hear and after VOS), giving rise to 0D, 1D, 2D or 3D inorganic scaffolds. In this regard, the work of Zubieta *et al.*[7] is mainly focused on the construction of HV from organic components that usually chelate the secondary metal centres. In HV, the secondary metal centres are defined as metal cations that are connected to the organic ligands and usually also to the VOS. A schematic example of HV combining metal–organic discrete units linked through VOS is shown in Fig. 1. The molecular complexes generated by the metal centres and the chelating ligands are connected by the VOS, giving rise to a 1D crystal structure.

The use of bridging ligands allows the combination of the inorganic substructures (defined as the framework constructed from the VOS and the secondary metal centres) with metal–organic subnets, giving rise to more complex crystal architectures. Indeed, as it is observed in Fig. 1, metal centres of a square planar metal–organic net can be connected through the VOS, giving rise to a crystal structure combining both 2D inorganic and metal–organic arrays. As in MOFs, the interpenetration or catenation phenomena of the nets are observed in several HV. Moreover, the linkage

Edurne S. Larrea

Edurne Serrano received her PhD in 2009 from the University of the Basque Country (UPV/EHU), where she now is a postdoctoral research associate to the Crystallography Group. Her thesis work was focused on the search of open inorganic–organic compounds based on the vanadate oxoanion, involving crystal structure resolution and analysis, and the study of their thermal, spectroscopic and magnetic properties. She has specialized on the study of the catalytic properties of inorganic–organic materials. During her postdoctoral trajectory, she has studied M'MOF materials, designed by the metallo-ligand approach, and focused on how to obtain porous crystal frameworks with open metal sites for enhanced catalytic activity.

M. Karmele Urtiaga

Miren Karmele Urtiaga Greaves received her PhD in Geology in 1993 from the University of the Basque Country (UPV/EHU), although a great part of her doctoral work was carried out in the University of Barcelona, in collaboration with Prof. Xabier Solans. She joined the Crystallography group at the UPV/EHU, where, since 2003, she has been a Full Professor of Crystallography. Her research in the field of crystallography focuses on the structural resolution and physico-chemical properties of coordination polymers. She has been the director of the Mineralogy and Petrology Department (2010–2013) and the academic secretary of the PhD and Master School of the UPV/EHU since 2013.

María I. Arriortua

Maria Isabel Arriortua's (PhD 1981, UPV/EHU) interest in solid state chemistry dates back to her work in the University of Louvain-la-Neuve, where she did part of her PhD thesis. Upon returning to the University of the Basque Country, she set up the Crystallography group at this university and her work has resulted in over 300 scientific articles. Since 1992, she has been a Full Professor of Crystallography and Mineralogy at the UPV-EHU. She is an Expert Committee Member of the Design of Basic Strategic Lines of Science, Technology and Innovation for the Basque Government and the Coordinator of Materials Science and Technology for the National Evaluation and Foresight Agency (ANEP) of the Spanish Government (2010–2013).

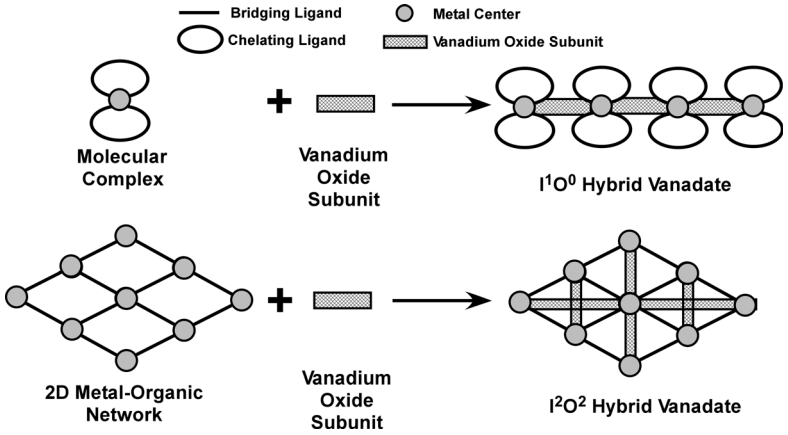

Fig. 1 Schematic representations of the combination between coordination metal–organic complexes plus vanadium oxide subunits (top) and the combination of extended metal–organic nets with vanadium oxide subunits (bottom).

of these interpenetrated or catenated nets through the VOS gives rise to self-catenated structures.[8]

Since the pioneering work of Zubieta *et al.*,[7] a great number of transition hybrid vanadium oxides containing polymeric metal–organic substructures have been reported. Therefore, a generalized highlight comprising the wide range of HV containing extensive metal–organic substructures, reported during the past years, and even a descriptive systematization of these architectures are urgent. Hybrid vanadium oxides constructed from chelating ligands are extensively described in the literature. They possess several common characteristics with the HV containing bridging ligands, thus we are going to discuss these points during the description of the crystal structures.

This highlight is divided into four sections dealing with: i) a brief discussion about the crystal chemistry, ii) classification, iii) crystal structure archetypes and iv) thermal, magnetic and catalytic properties of HV.

1. Hybrid vanadate archetypes: from zeotypes to MOFs

Despite the difficulties to control the final crystal architectures in HV, the analysis of the synergistic interactions between the inorganic and the organic components allows a partial degree of "crystal engineering" towards more open or condensed structural archetypes. The three main factors that define the obtained crystal structures in HV are: i) the coordination preferences and oxidation state of the secondary metal centres; ii) the length, geometry, degree of flexibility and relative position of the donor groups of the ligand; and iii) the structural influence of the vanadate anion on the framework organization and assembly adopted by the different metal–organic moieties.

The coordination preferences and geometry of the metal centres are key issues, just as in classical coordination chemistry. A systematic search in the CSD (Cambridge Structural Database) reveals the existence of 218 different crystal structures for HV in which the metal centres are linked through M–O–V linkage to the VOS. Up to now, Mn(II), Fe(II), Co(II), Ni(II), Cu(II), Cu(I), Zn(II), Ag(I) and Cd(II) secondary metal centres have been used to obtain HV.

Ni(II), Co(II), Mn(II) and Cd(II) cations in HV usually present regular octahedral coordination environments, although a few examples of HV with five coordinated Co(II) cations are known. The great diversity of coordination modes, octahedral, five-coordinated and tetrahedral, for Cu(II) and Zn(II) atoms allows one to obtain several crystal structures with different metal coordination environments. This fact makes more difficult the prediction of the structural archetypes obtained with these cations, but enlarges the rich structural diversity of Zn(II) and Cu(II) vanadates in comparison with those obtained from cations possessing regular octahedral coordination spheres. For Cu(I) and Ag(I), the coordination spheres are less predictable, but with certain types of ligands, these ions are only able to support the formation of one-dimensional metal–organic substructures due to their linear coordination.

The length, geometry and position of the donor groups of the ligand determine its role in the construction of the final crystal structure. Chelating ligands, such as 2,2-bipyridine,[9,10] 1,10-phenanthroline[11,12] and terpyridine,[13,14] give rise to discrete metal–organic units. On the other hand, dipodal or multi-podal bridging ligands such as pyrazine, 4,4′-bipyridine, and 1,2-di(4-pyridyl)ethylene allow obtaining extended metal–organic nets (see Tables 1–3). These polytopic organic amino ligands serve to link the metal sites, propagating the structural information expressed by the metal coordination preferences through the extended structure. Fig. 2 and 3 show the dipodal and multi-podal amino ligands found in HV with extended metal–organic frameworks. The ligands combining both amino and carboxylate donor groups have been also used in the synthesis of HV, allowing an increase in the connectivity of the metal centres through the organic ligand. Another interesting strategy is the use of unsymmetrical ligands to obtain noncentrosymmetric microporous compounds. The most common ligands containing carboxylate groups observed in HV are depicted in Fig. 4.

Table 1 Hybrid vanadium oxides constructed from pyrazine and pyrimidine. (The coordination environment of the vanadium cations is briefly described as 4-c, 5-c, and 6-c for tetrahedral, square pyramid and octahedral coordination spheres, respectively. In the same sense the oxidation states for the vanadium atoms are depicted as V(v) and V(iv))

Compound	Vanadium oxide subunit	Metal–organic subnet	Class.	Ref.
Pyrazine (Pz)				
$\{M(Pz)\}(VO_3)_2$, M = Ni, Co	Metavanadate chains. 4-c V(v)	M(Pz) crossed chains (1D)	I^3O^1, 3D + 1D → 3D	POCNIF,[36] QOXFEO[37]
$\{M(Pz)\}(V_4O_{10})$, M = Ni, Co, Zn	Vanadium oxide layers constructed from corner-shared double metavanadate chains. 5-c V(v)/V(iv)	M(Pz) chains parallel to the vanadium oxide layers (1D)	I^3O^1, 3D + 1D → 3D	XEHYAL, XEHXUE, XEHYEP[38]
$\{Ni_2(H_2O)_2(Pz)\}(V_4O_{12})$	$\{V_4O_{12}\}$ cycles. 4-c V(v)	Ni(Pz) chains (1D)	I^2O^1, 2D + 1D → 3D	GICDEC[39,40]
$\{Ni_3(Pz)_3\}(V_8O_{23})$	Metavanadate chains of corner-sharing VO_4 tetrahedra, linked through V_2O_7 dimers. 4-c V(v)	Ni(Pz) chains (1D)	I^3O^1, 3D + 1D → 3D	GICDAY[39]
$[\{Cu(Pz)_2\}(V_6O_{16})]\cdot 0.22H_2O$	Vanadium oxide layers constructed from corner-sharing double metavanadate chains. 5-c V(v)	$Cu(Pz)_2$ square-like metal–organic layers (2D)	I^3O^2, 3D + 2D → 3D	IJUCIZ[41]
$\{Cu_2(Pz)\}(V_4O_{12})$	$\{V_4O_{12}\}$ cycles. 4-c V(v)	$Cu_2(Pz)$ discrete units (0D)	I^3O^0, 3D + 0D → 3D	MUJSAL[42]
Pyrimidine (Pym)				
$\{Co(Pym)\}(VO_3)_2$	Metavanadate chains of edge-sharing VO_5 polyhedra. 5-c V(v)	Co(Pym) chains (1D)	I^1O^3, 3D + 1D → 3D	KOPHEE[43]

Table 2 Hybrid vanadium oxides constructed from 4,4′-bipyridine. (The coordination environment of the vanadium cations is briefly described as 4-c, 5-c, and 6-c for tetrahedral, square pyramid and octahedral coordination spheres, respectively. In the same sense, the oxidation states of the vanadium atoms are depicted as V(v) and V(iv))

Compound	Vanadium oxide subunit	Metal–organic subnet	Class.	Ref.
4,4′-Bipyridine (4Bpy)				
$[\{M_2(H_2O)_2(4Bpy)_3\}(VO_3)_4]\cdot 2.5H_2O$, M = Ni, Co	Metavanadate chains of corner-sharing VO_4 tetrahedra. 4-c V(v)	Interpenetrated $M_2(4Bpy)_3$ square-like metal–organic layers (2D + 2D)	I^3O^2, 3D + (2D + 2D) → 3D	OCAQOY,[44] FIYDOH[45]
$[\{Ni_6(H_2O)_{10}(4Bpy)_6\}(V_{18}O_{51})]\cdot 1.5H_2O$	Metavanadate chains of edge-sharing VO_5 polyhedra, corner linked to V_2O_7 dimers. 4-5-c V(v)	Ni(4Bpy) crossed metal–organic chains (1D)	I^3O^1, 3D + 1D → 3D	OHUQUE[46]
$[\{Ni_8(4Bpy)_{16}\}(V_{24}O_{68})]\cdot 8.5H_2O$	V_5O_{15} cycles corner linked through single VO_4 tetrahedra, generating chains. 4-c V(v)	Polycatenation of $Ni(4Bpy)_2$ "cds"-like 3D metal–organic subnet with two square-like $Ni(4Bpy)_2$ metal–organic layers (3D + 2D + 2D)	I^3O^3, 3D + (2D + 3D) → 3D	DUXKEN[47]
$\{Co(4Bpy)\}(VO_3)_2$	$\{V_4O_{12}\}$ cycles. 4-c V(v)	Co(4Bpy) parallel metal–organic chains (1D)	I^2O^1, 2D + 1D → 3D	QOXFAK[37]
$[\{Ag(4Bpy)\}_4(V_4O_{12})]\cdot 2H_2O$	$\{V_4O_{12}\}$ cycles. 4-c V(v)	Ag(4Bpy) parallel chains (1D)	I^2O^1, 2D + 1D → 3D	EGOGUD[48]
$\{M(4Bpy)\}(V_4O_{10})$, M = Cu, Ag	Vanadium oxide layers constructed from corner-sharing double metavanadate chains. 5-c V(v)	M(4Bpy) parallel chains (1D)	I^3O^1, 3D + 1D → 3D	WIMHUW,[49] WIMJAE[49]
$[\{Cu(4Bpy)\}_4(V_4O_{12})]\cdot 2H_2O$	$\{V_4O_{12}\}$ cycles. 4-c V(v)	$Cu_2(4Bpy)_2$ double chains (1D)	I^1O^1, 1D + 1D → 3D	PAVDAS[50]
$[\{Mn(4Bpy)\}(VO_3)_2]\cdot 1.16H_2O$	Metavanadate chains of edge-sharing VO_5 polyhedra. 5-c V(v)	Mn(4Bpy) layers (2D)	I^2O^2, 2D + 2D → 3D	TAQYER[51]
$[\{Mn(4Bpy)_{0.5}\}(VO_3)_2]\cdot 0.62H_2O$	Metavanadate chains of edge-sharing VO_5 polyhedra. 5-c V(v)	$Mn(4Bpy)_{0.5}$ discrete layers (2D)	I^2O^2, 2D + 2D → 3D	TAQYIV[51]

At this point, the transition metal HV constructed from dipodal ligands have common characteristics with MOFs because of the generation of metal–organic sub-structures through the linkage of metal and ligands. Usually, the VOS are located in the channels of the metal–organic framework and directly linked to the secondary metal centres. The combination of metal–organic nets based on nitrogen donor dipodal bridging ligands and VOS has also become a great chemical strategy to synthesize self-catenated and/or highly connected nets.[15] One of the keys to explain the crystal

Table 3 Hybrid vanadium oxides constructed from Bpe (1,2-di(4-pyridyl)ethylene) and Bpa (1,2-di(4-pyridyl)ethane. (The coordination environment of the vanadium cations is briefly described as 4-c, 5-c, and 6-c for tetrahedral, square pyramid and octahedral coordination spheres, respectively. In the same sense, the oxidation states of the vanadium atoms are depicted as V(v) and V(iv))

Compound	Vanadium oxide subunit	Metal–organic subnet	Class.	Ref.
1,2-Di(4-pyridyl)ethylene (Bpe)				
$\{Ni(Bpe)\}(VO_3)_2$	Metavanadate chains of corner-sharing VO_4 tetrahedra. 4-c V(v)	Interpenetrated Ni(Bpe) rhombic-like metal–organic layers (2D + 2D)	I^2O^2, 2D + (2D + 2D) → 3D	TIGHOH[52,53]
$[\{Ni(H_2O)_2(Bpe)\}(V_4O_{11})]\cdot 0.5H_2O$	Double metavanadate chain. 5-c V(v)	Crossed Ni(Bpe) metal–organic chains (1D)	I^3O^1, 3D + 1D → 3D	OHURAL[46]
$\{Co(HBpe)_2\}(V_4O_{12})$	$\{V_4O_{12}\}$ cycles. 4-c V(v)	$Co(HBpe)_2$ discrete units (0D)	I^1O^0, 1D + 0D → 1D	DIWXUD[54,55]
$[\{M(H_2O)_2(Bpe)_2\}(V_4O_{12})]\cdot 4H_2O\cdot Bpe$; M = Ni, Co	$\{V_4O_{12}\}$ cycles. 4-c V(v)	M(Bpe) metal–organic chains (1D)	I^2O^1, 2D + 1D → 3D	DEYJIC, DEYJOI[56]
1,2-Di(4-pyridyl)ethane (Bpa)				
$[\{Ag(Bpa)\}_4(V_4O_{12})]\cdot 4H_2O$	$\{V_4O_{12}\}$ cycles. 4-c V(v)	Ag(Bpa) corner-linked chains giving rise to metal–organic layers (2D)	I^2O^2, 2D + 2D → 3D	EGOHAK[48]
$[\{Ni(H_2O)(Bpa)\}(VO_3)_2]\cdot 2H_2O$	$\{V_4O_{12}\}$ cycles. 4-c V(v)	Ni(Bpa) chains (1D)	I^2O^1, 2D + 1D → 3D	ZEFWIS[57]
$[\{Ni_3(H_2O)_3(Bpa)_4\}(V_6O_{18})]\cdot 8H_2O$	$\{V_6O_{18}\}$ cycles. 4-c V(v)	Three $Ni_3(Bpa)_4$ interpenetrated "mot"-like 3D nets (3D + 3D + 3D)	I^3O^3, 3D + (3D + 3D + 3D) → 3D	CAWZUX[58]
$\{Ni_2(H_2O)_2(Bpa)_2\}(V_6O_{17})$	Metavanadate chains. 4-c V(v)	Ni(Bpa) parallel chains (1D)	I^3O^1, 3D + 1D → 3D	[59]
$\{Co(Bpa)\}(VO_3)_2$	$\{V_4O_{12}\}$ cycles. 4-c V(v)	Co(Bpa) parallel chains (1D)	I^2O^1, 2D + 1D → 3D	XOJKUD01 (ref. 57)

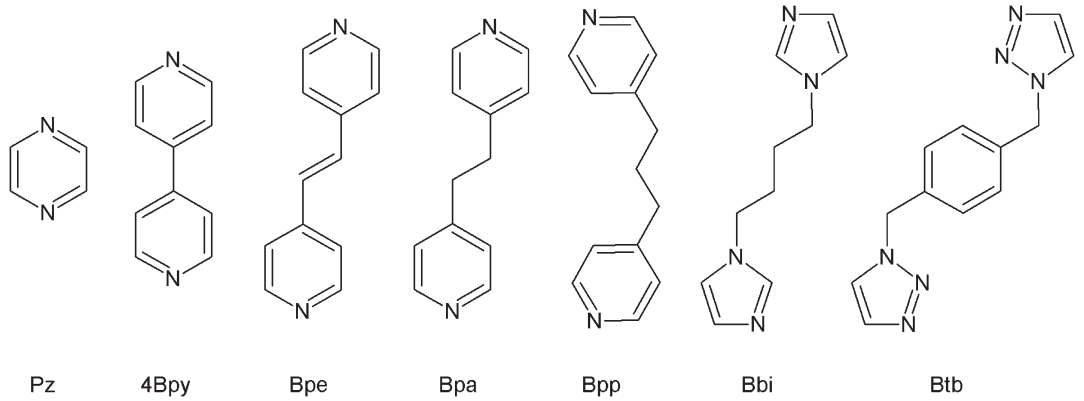

Fig. 2 Bipodal organic ligands observed in HV: Pz (pyrazine), 4Bpy (4,4′-bipyridine), Bpe (1,2-di(4-pyridyl)ethylene), Bpa (1,2-di(4-pyridyl)ethane), Bpp (1,3-bis(4-pyridyl)propane), Bbi (1,4-bis(imidazol-1-yl)butane), and Btb (1,4-bis(triazol-1-ylmethyl)benzene).

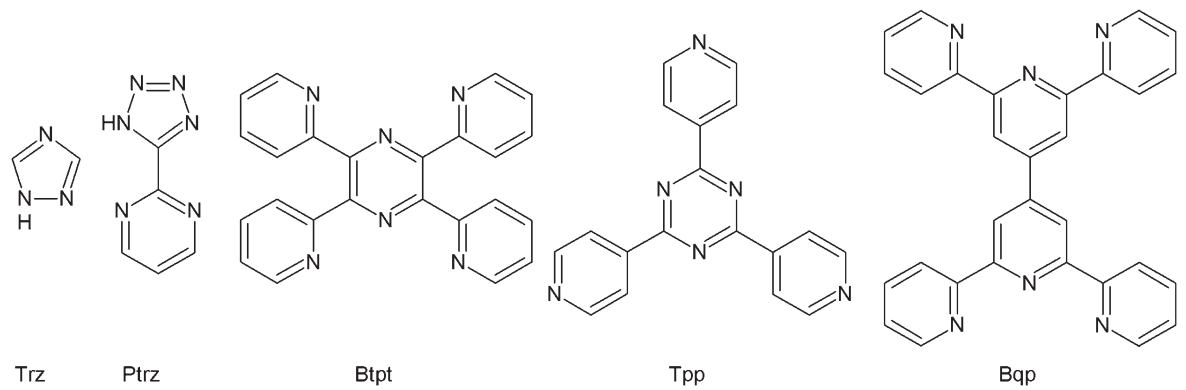

Fig. 3 Multi-podal organic ligands observed in HV: Trz (1,2,4-triazole), Ptrz (5-(pyrimidin-2-yl)tetrazole), Btpt (tetra-2-pyridylpyrazine), Tpp (2,4,6-tri(4-pyridyl)-1,3,5-triazine), and Bqp (6′,6″-bis(2-pyridyl)-2,2′:4′,4″:2″,2‴ -quaterpyridine).

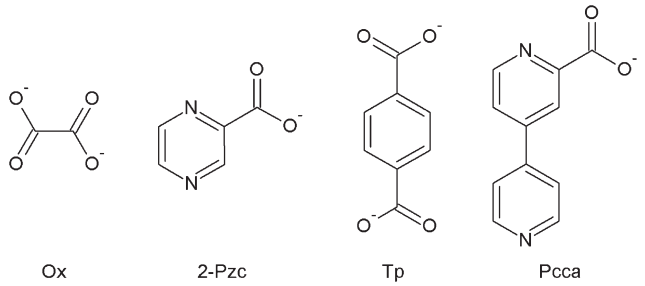

Fig. 4 Multi-podal carboxylic organic ligands observed in HV: Ox (oxalate), 2-Pzc (2-pyrazinecarboxylate), Tp (terephthalate), and Pcca (4,4′-bipyridine-2-carboxylate).

chemistry of HV is the connectivity between the metal–organic subnets and the VOS, in addition to the role of VOS itself.

Vanadium commonly adopts V(v), V(iv) and V(iii) oxidation states. The coordination environments, as well as the V–O bond distances, are clearly related to the vanadium oxidation state. The coordination environment of V(iii) is a regular octahedron. V(iv) exhibits five or six coordination environments, while V(v) ranges from six to four coordination. The most common coordination environments shown by vanadium atoms in HV are the regular tetrahedron and the distorted square pyramid. Similarly, the most common oxidation state of vanadium atoms in HV is V(v), but several architectures containing five-coordinated mixed valence V(v)/V(iv) have been reported. For an extensive study about the oxidation states and coordination environments of vanadium, the reader should refer to the work of Schindler *et al.*[16]

Vanadium polyhedra may fuse to provide different VOS, such as discrete oligomers (dimers, cycles or clusters), 1D chains or 2D layers, constructed from the same polyhedron or mixtures of various polyhedral types. The most comprehensive study of inorganic structures was provided by Wells in the book *Structural Inorganic Chemistry*,[17] but no specific information about vanadium oxides was included. Later studies by Zavalij and Whittingham[18] and Zubieta *et al.*[7] are extensive studies of the structural chemistry of vanadium oxides with open frameworks and the influence of organic components on vanadium oxide architectures, respectively. Zavalij and Whittingham[18] deeply described and systematized the VOS, classifying them according to the coordination environment of vanadium polyhedra and the connectivity between them.

In HV containing bridging ligands and more polymerized VOS constructed from six coordinated vanadium seem to be avoided, while more open subunits constructed from VO_4 tetrahedra and/or VO_5 polyhedra are favoured. In this regard, the most common VOS are the metavanadate $(VO_3)^-$ chains and the $\{V_4O_{12}\}$ cycles, both formed by corner-sharing (VO_4) tetrahedra. Both units possess the ability to link to metal centres or to other VOS in different directions of the crystal structure. In this sense, the $\{V_4O_{12}\}$ cycle can act as a two, four or six connector. Besides the $\{V_4O_{12}\}$ cycles, different $\{V_xO_y\}$ cyclic discrete units have been observed, depending on the number of polyhedra that compose them, $\{V_2O_7\}$, $\{V_5O_{15}\}$, $\{V_6O_{18}\}$, $\{V_8O_{25}\}$, $\{V_{10}O_{30}\}$, and $\{V_{12}O_{36}\}$, among others (Fig. 5).

With regard to the metavanadate chains, they also could act as multidirectional connectors. This unit possesses a certain degree of adaptability to the crystal environment due to the reorientation and reorganization ability of the (VO_4) tetrahedra. Fig. 6 shows some metavanadate chains belonging to different vanadates. The number of tetrahedra that by translation gives rise to the whole chain increases progressively from two, in $Ba(VO_3)\cdot 2H_2O$,[19] to twelve, in $\{Ni(en)_3\}(VO_3)_2$,[20] depending on the connectivity between the metavanadate chains and their crystal environment.

There is also a very rich crystal chemistry of vanadate chains and layers constructed from five- and six-coordinated vanadium atoms, but these structural subunits are not commonly observed in HV constructed from bridging ligands. The reader should consult the work of Zavalij and Whittingham[18] for a more thorough study about VOS in open framework vanadates. Only one type of metavanadate chains constructed from five-coordinated vanadium has been reported. This consists of edge-sharing (VO_5) square pyramids, as observed in Fig. 7.

The structural diversity of inorganic–organic vanadates is not only based on the great variety of VOS, but also on their ability to link to each other, giving rise to more complex one-, two- or three-dimensional architectures. There are several vanadates whose crystal structures are constructed from the combination of some of the previously described VOS. Examples of them are the chains constructed from corner-sharing $\{V_6O_{18}\}$ cycles, the chains formed by the connectivity between $\{V_4O_{12}\}$ cycles and $\{V_2O_7\}$ dimers,[25,26] sheets of corner-sharing VO_4 polyhedra and metavanadate

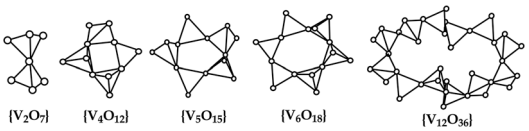

Fig. 5 Several vanadium oxide cycles observed in hybrid vanadates.

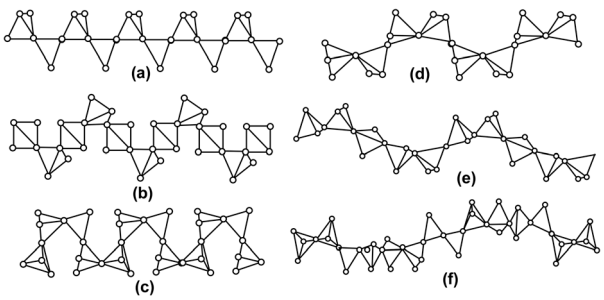

Fig. 6 Metavanadate chains of corner-sharing VO_4 tetrahedra: (a) $Ba(VO_3)\cdot 2H_2O$,[19] (b) $NH_3(CH_2)_4NH_3(VO_3)_2$,[21] (c) $M(Hdpa)V_4O_{12}$ (M = Co, Ni),[22] (d) $Cu(2Bpy)V_2O_6$,[23] (e) $Co_3(Bpp)_4V_6O_{18}\cdot 2H_2O$,[24] and (f) $\{Ni(en)_3\}(VO_3)_2$.[20]

chains combined with $\{V_2O_7\}$ dimers (for more information, see Tables 1–6). There are also a few examples of HV constructed from vanadium oxide V_xO_y layers. These layers can be described as the combination of corner-linked metavanadate chains of edge-sharing VO_5 polyhedra, as the ones observed in Fig. 7.

2. Classification of hybrid vanadates

The studies by Zavalij and Whittingham[18] and Zubieta *et al.*[7] summarize the crystal chemistry of these materials. They proposed two different but complementary classifications. Zavalij and Whittingham based their classification of the open framework vanadium oxides on the coordination environment of the vanadium atom. Seven categories can be distinguished according to the presence of tetrahedra (T), square pyramids (SP) and/or octahedra (O) in the crystal structures. As a complementary point of view, Zubieta *et al.* take into account the role of the metal–organic or the organic moiety in the crystal structure, distinguishing four different classes of HV:

a) compounds in which the organic component or the metal–organic discrete coordination complex acts as an isolated cation, compensating for the charge of the vanadium oxide host;

b) phases in which the organic molecule serves as a ligand directly attached to the oxide array;

c) transition metal HV in which the organic ligand is coordinated to the transition metal and this secondary metal is linked to the VOS through oxygen bridges. The organic ligand coordinates only one metal centre, preventing the propagation of the crystal structure through the organic linkers; and

d) HV constructed from extended metal–organic nets (one-, two- or three-dimensional) linked to the metal centre through VOS.

The classification of Zubieta *et al.*[7] lies within the previous one described by Cheetham *et al.*[27] for hybrid inorganic–organic compounds. These authors proposed a classification based on an $\mathbf{I}^n\mathbf{O}^m$ code, in which $\mathbf{I}^n$ takes into account the dimensionality of the inorganic substructure (n = 0, 1, 2, 3) and $\mathbf{O}^m$ refers to the dimensionality of the metal–organic array (m = 0, 1, 2, 3). In this classification, for example, the zeolite-type compounds constructed from three-dimensional inorganic skeletons containing isolated organic cations are classified as $\mathbf{I^3O^0}$ materials, while the coordination polymers

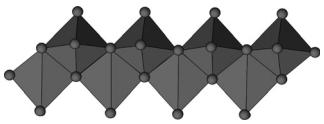

Fig. 7 Metavanadate chains of edge-sharing (VO_5) square pyramids.

Table 4 Hybrid vanadium oxides constructed from Bbi (1,4-bis(imidazol-1-yl)butane), Bpp (1,3-bis(4-pyridyl)propane and Btb (1,4-bis(triazol-1-yl-methyl)benzene). (The coordination environment of the vanadium cations is briefly described as 4-c, 5-c, and 6-c for tetrahedral, square pyramid and octahedral coordination spheres, respectively. In the same sense, the oxidation states of the vanadium atoms are depicted as V(v) and V(iv))

Compound	Vanadium oxide subunit	Metal–organic subnet	Class.	Ref.
1,4-Bis(imidazol-1-yl)butane (Bbi)				
$\{Cd(HBbi)_2\}(V_4O_{12})$	$\{V_4O_{12}\}$ cycles. 4-c V(v)	$Cd(HBbi)_2$ discrete units (0D)	I^1O^0, 1D + 0D → 1D	AHAXOX[60]
$\{Co(H_2O)(Bbi)\}(VO_3)_2$	Metavanadate chains of corner-sharing VO_4 tetrahedra. 4-c V(v)	Parallel corrugated Co(Bbi) chains (1D)	I^3O^1, 3D + 1D → 3D	TOHQAJ[61]
$\{M_2(H_2O)_2(Bbi)\}(VO_3)_4$, M = Co, Mn	Metavanadate chains of corner-sharing VO_4 tetrahedra. 4-c V(v)	Parallel $M_2(Bbi)$ chains (1D)	I^2O^1, 2D + 1D → 3D	VUTLAY, VUTLEC[62]
$[\{M_2(Bbi)_3\}(V_4O_{12})]\cdot 4H_2O$, M = Ni, Co	$\{V_4O_{12}\}$ cycles. 4-c V(v)	Two 3D $M_2(Bbi)_3$ interpenetrated metal–organic subnets. (3D + 3D)	I^1O^3, 1D + (3D + 3D) → 3D	VIRYOL,[63] VUTLIG[62]
$[\{Ni_2(H_2O)_4(Bbi)_2\}(VO_3)_4]\cdot 2H_2O$	Metavanadate chains of corner-sharing VO_4 tetrahedra. 4-c V(v)	Perpendicular Ni(Bbi) chains (1D)	I^3O^1, 3D + 1D → 3D	TOHPUC[61]
$[\{Cu(Bbi)_2\}(V_4O_{12})]\cdot 4H_2O$	$\{V_4O_{12}\}$ cycles. 4-c V(v)	$Cu(Bbi)_2$ layers (2D)	I^0O^2, 0D + 2D → 2D	NUXXUA[64]
$\{Cu_2(Bbi)_3\}(V_4O_{12})$	$\{V_4O_{12}\}$ cycles. 4-c V(v)	$Cu(Bbi)_2$ layers (2D) + Cu(Bbi) (1D) chains	I^1O^2, 1D + (2D + 1D) → 2D	VIRYIF[63]
$[\{Ag(Bbi)_4\}\{Ag_3(V_4O_{12})_2\}][Ag(Bbi)]\cdot 2H_2O$	$\{V_4O_{12}\}$ cycles. 4-c V(v)	Ag(Bbi) chains	I^1O^1, 1D + 1D → 2D	EHODIP[65]
1,3-Bis(4-pyridyl)propane (Bpp)				
$\{M_2(Bpp)_4\}(V_4O_{12})$, M = Co, Ni	$\{V_4O_{12}\}$ cycles. 4-c V(v)	Two interpenetrated $M(Bpp)_2$ layers (2D + 2D)	I^3O^2, 3D + (2D + 2D) → 3D	SAZSOC,[66] DIXNII[67]
$\{Zn(Bpp)\}(VO_3)_2$	Metavanadate chains of corner-sharing VO_4. 4-c V(v)	Perpendicular Zn(Bpp) chains (1D)	I^3O^1, 3D + (1D + 1D + 1D) → 3D	HISWUC[68]
$[\{Cu_4(Bpp)_4\}(V_4O_{12})]\cdot 3H_2O$	$\{V_4O_{12}\}$ cycles. 4-c V(v)	Cu(Bpp) metal–organic chains (1D)	I^0O^1, 0D + 1D → 3D	LIGPUN[69]
1,4-Bis(triazol-1-ylmethyl)benzene (Btb)				
$\{Co_3(H_2O)(Btb)_5\}(V_8O_{23})$	$\{V_8O_{23}\}$ units constructed from two $\{V_5O_{15}\}$ fused rings. 4-c V(v)	Polycatenated $Co_2(Btb)_3$ and $Co(Btb)_2$ layers (2D + 2D)	I^3O^2, 3D + (2D + 2D) → 3D	MUTZEH[70]

Table 5 Hybrid vanadium oxides constructed from Bpq (6′,6″-bis(2-pyridyl)-2,2′:4′,4″:2″,2‴-quaterpyridine), Btpt (tetra-2-pyridylpyrazine), Tpp (2,4,6-tri(4-pyridyl)-1,3,5-triazine), Trz (triazole), and Ptrz (5-(pyrimidin-2-yl)tetrazole). (The coordination environment of the vanadium cations is briefly described as 4-c, 5-c, and 6-c for tetrahedral, square pyramid and octahedral coordination spheres, respectively. In the same sense, the oxidation states of the vanadium atoms are depicted as V(v) and V(iv))

Compound	Vanadium oxide subunit	Metal–organic subnet	Class.	Ref.
6′,6″-Bis(2-pyridyl)-2,2′:4′,4″:2″,2‴-quaterpyridine (Bpq)				
$[\{Cu_2(Bpq)\}(V_4O_{12})]\cdot 2H_2O$	$\{V_4O_{12}\}$ cycles. 4-c V(v)	$Cu_2(Bpq)$ discrete units (0D)	I^1O^0, 1D + 0D → 2D	TIJHAW[71]
Tetra-2-pyridylpyrazine (Btpt)				
$\{Zn_2(Btpt)\}(V_4O_{12})$	$\{V_4O_{12}\}$ cycles. 4-c V(v)	$Zn_2(Btpt)$ discrete units (0D)	I^1O^0, 1D + 0D → 2D	ATAGUX[72]
$\{Co_2(Btpt)_2\}(V_4O_{12})$	$\{V_4O_{12}\}$ cycles. 4-c V(v)	$Co_2(Btpt)_2$ discrete units (0D)	I^1O^0, 1D + 0D → 1D	ATAGEH[72]
$\{Cu_2(Btpt)_2\}(V_4O_{12})$	$\{V_4O_{12}\}$ cycles. 4-c V(v)	$Cu_2(Btpt)_2$ discrete units (0D)	I^0O^0, 0D + 0D → 0D	MUJSEP[73]
$[\{Cu_2(Btpt)_2\}(V_4O_{12})]\cdot 2H_2O$	$\{V_4O_{12}\}$ cycles. 4-c V(v)	$Cu_4(Btpt)_2$ chains (1D)	I^0O^1, 0D + 1D → 2D	ATAGOR[72]
2,4,6-Tri(4-pyridyl)-1,3,5-triazine (Tpp)				
$\{Zn(Tpp)_2\}(VO_3)_2$	Metavanadate chains of corner-sharing VO_4. 4-c V(v)	$Zn(Tpp)_2$ discrete units (0D)	I^2O^0, 2D + 0D → 2D	EHODEK[74]
$[\{Cu_3(H_2O)_2(Tpp)_2\}(V_8O_{23})]\cdot 3H_2O$	Metavanadate chains of corner-sharing VO_4. 4-c V(v)	Two parallel interpenetrated $Cu_3((Tpp)_2$ layers (2D + 2D)	I^3O^2, 3D + (2D + 2D) → 3D	EHODOU[74]
$[\{Zn_3(H_2O)_2(Tpp)_2\}(VO_3)_6]\cdot 6H_2O$	Metavanadate chains of corner-sharing VO_4. 4-c V(v)	Parallel and corrugated $Zn_3(Tpp)_2$ layers (2D + 2D)	I^3O^2, 3D + (2D + 2D) → 3D	EHODIO[74]
Triazole (Trz)				
$\{Cu_3(1,2,3\text{-}Trz)_2\}(V_4O_{12})$	$\{V_4O_{12}\}$ cycles. 4-c V(v)	$Cu_3(Trz)_2$ chains (1D)	I^2O^1, 2D + 1D → 3D	MUJSIT[73]
$\{Cu_3(1,2,4\text{-}Trz)_2\}(V_4O_{12})$	Metavanadate chains of corner-sharing VO_4. 4-c V(v)	$Cu_3(Trz)_2$ layers (2D)	I^3O^2, 3D + 2D → 3D	LOQKIL[75]
5-(Pyrimidin-2-yl)tetrazole (Ptrz)				
$\{Cu_3(Ptrz)_2\}(VO_3)_4$	Metavanadate chains of corner-sharing VO_4. 4-c V(v)	$Cu_3(Ptrz)_2$ layers (2D)	I^1O^2, 1D + 2D → 3D	CIXPAD[76]

Table 6 Hybrid vanadium oxides constructed from carboxylate-based ligands. (The coordination environment of the vanadium cations is briefly described as 4-c, 5-c, and 6-c for tetrahedral, square pyramid and octahedral coordination spheres, respectively. In the same sense, the oxidation states of the vanadium atoms are depicted as V(v) and V(iv))

Compound	Vanadium oxide subunit	Metal–organic subnet	Class.	Ref.
Oxalate (Ox)				
$(en)[\{Co_2(Ox)\}(V_4O_{12})]$	$\{V_4O_{12}\}$ cycles. 4-c V(v)	$Co_2(Ox)$ discrete dimers	I^3O^0, 3D + 0D → 3D	HUVLUF[77]
$(H_2pn)[Mn_2(Ox)(V_4O_{12})]$	$\{V_4O_{12}\}$ cycles. 4-c V(v)	$Mn_2(Ox)$ discrete dimers	I^3O^0, 3D + 0D → 3D	XIRCIK[78]
2-Pyrazinecarboxylate (2-Pzc)				
$\{Co_2(H_2O)(2\text{-}Pzc)\}(VO_3)_3$	Metavanadate chains of corner-sharing VO_4. 4-c V(v)	$Co_2(2\text{-}Pzc)$ chains	I^3O^1, 3D + 1D → 3D	QOFIS[37]
$M_4(2\text{-}Pzc)_4(V_6O_{17})$, M = Ni, Co	Double $\{V_6O_{17}\}$ metavanadate chains of corner-sharing VO_4. 4-c V(v)	Connected $M_4(2\text{-}Pzc)_4$ helical chains giving rise to chiral helical tubes	I^3O^1, 3D + 1D → 3D	WOWHEV, WOWHAR[79]
$[(NH_4)_2Co_8(H_2O)_2(2\text{-}Pzc)_8(VO_3)_{10}]\cdot xH_2O$	Metavanadate chains of corner-sharing VO_4. 4-c V(v)	Connected $M_4(2\text{-}Pzc)_4\}$ helical chains giving rise to chiral helical tubes	I^3O^1, 3D + 1D → 3D	WOWHIZ[79]
$\{Ag_4(2\text{-}Pzc)_2\}(V_2O_6)$	Metavanadate chains of corner-sharing VO_4. 4-c V(v)	Three-dimensional $Ag_4(2\text{-}Pzc)_2$ metal–organic net	I^2O^3, 2D + 3D → 3D	EGOHEO[48]
Terephthalate (Tp)				
$\{Zn_2(Tp)(4\text{-}Bpy)\}(VO_3)_2$	$\{V_4O_{12}\}$ cycles. 4-c V(v)	$Zn_2(Tp)(4\text{-}Bpy)$ layers	I^0O^2, 0D + 2D → 2D + 2D	XENCUO[80]
4,4′-Bipyridine-2-carboxylate (Pcca)				
$[\{Co_2(Pcca)_2(H_2O)\}(VO_3)_2]$	$\{V_4O_{12}\}$ cycles. 4-c V(v)	$Co_2(Pcca)_2$ layers	I^1O^1, 1D + 1D → 2D	SAVWIN[81]
$[\{Co(Pcca)_2(H_2O)\}(VO_3)_2]\cdot 3.62H_2O$	Metavanadate chains of corner-sharing VO_4. 4-c V(v)	Double chains constructed from corner-linked $Co(Pcca)_2$ chains	I^1O^2, 1D + 2D → 3D	SAVWAO[82]

formed by inorganic clusters linked through organic ligands are included in the I^0O^3 archetype. It is clear that many systems combine both inorganic and metal–organic extended arrays, for example, there are several MOFs constructed from inorganic chains connected by organic linkers (I^1O^1), or coordination polymers containing inorganic layers pillared by organic ligands directly attached to the metal centres, generating also metal–ligand–metal one dimensional arrays (I^2O^1).[28]

Fig. 8(a) summarizes the structural classes described by Cheetham *et al.*,[27] while in Fig. 8(b) the occurrence of each structural class observed in HV is represented.

Cheetham *et al.* proposed a very interesting question in their work: "The question arises as to whether there are materials that could be classified within the empty boxes in the right part of the table (red boxes in Fig. 8(a))… we currently know no such materials, but the possibility exists that these may be found in compounds that have not yet been discovered". Concerning this discussion, Natarajan and Mandal (see ref. 2(d)) gave a premonitory answer to this question in their work entitled "Open-Framework Structures of Transition-Metal Compounds" suggesting that "the limits are not the imagination and creativity of the researchers but the lack of understanding of the subtler forces involved in the formation of such structures… in light of this, it should be possible to prepare compounds based on other anions, such as VO_4^{3-}, MoO_4^{2-} or ReO_4^{-}. A combination of these anionic ligands with transition metals would open exciting possibilities for new properties and would also expand the scope of research on this area".

The great crystallochemistry of HV exhibits several intermediate structural archetypes combining extended metal–organic and inorganic arrays from zeolitic types ($\mathbf{I^3O^0}$) to coordination polymers ($\mathbf{I^0O^3}$). There are several examples of HV with complex structures lying in the previously empty boxes of the Cheetham *et al.* classification. As it is shown in Fig. 8(b), the analysis of the crystal structures reveals that $\mathbf{I^3O^2}$, $\mathbf{I^3O^1}$, $\mathbf{I^2O^2}$ and $\mathbf{I^2O^1}$ architectures are the most common architectures in HV. In the same way in metal–organic frameworks, the main factors that influence the dimensionality of the metal–organic substructure are the secondary metal coordination environment and ligand–metal connectivity. But, in HV, the VOS plays a crucial role, connecting the metal centres belonging to the metal–organic substructure, and hence, giving rise to a higher dimensionality of the inorganic framework and a greater degree of complexity in the crystal structures.

Fig. 9 outlines the simplification of the main structural archetypes observed in HV based on the metal–organic and inorganic substructures dimensionalities, according to the Cheetham *et al.* terminology, within each of the $\mathbf{I^nO^m}$ groups. The inorganic scaffold (**I**) is defined by the linkage of the VOS and the secondary metal centres, while the metal–organic substructure (**O**) is built from the secondary metals and the organic linkers. It is also necessary to incorporate the information of the whole crystal structure dimensionality into the Cheetham $\mathbf{I^nO^m}$ code, since the same combination of inorganic and metal–organic moieties could give rise to crystal structures with different dimensionalities, as shown in Fig. 9. For this reason, another code based on the overall dimensionality which takes into account the interaction between both subnets has been introduced. For example, the $\mathbf{I^1O^2}$ compounds are described also as 1D + 2D → 3D. When the crystal framework contains interpenetrated or polycatenated metal–organic subnets, the metal–organic substructure dimensionality will be denoted as (2D + 1D), which would represent a crystal structure that contains metal–organic layers polycatenated with metal–organic chains.

In order to better distinguish the metal–organic substructure and the VOS, the simplified models have been represented in different colours, orange and pink for the metal–organic part and blue for VOS, as stated in the legend of Fig. 9. Within several $\mathbf{I^nO^m}$ archetypes, a picture of

Hybrid 3D Framework I^3O^0	Inorg. 3D framework + metal-organic chains I^3O^1	Inorg. 3D framework and metal-organic layers I^3O^2	3-D inorg. and organic frameworks I^3O^3	I3
Hybrid inorg. layers I^2O^0	Inorg. layers + metal-organic chains I^2O^1	Inorg. layers + metal-organic layers I^2O^2	3-D Coordination polymers with inorg. layers I^2O^3	I2
Hybrid inorg. chains I^1O^0	Mixed inorg.-organic layers I^1O^1	Inorg. chains + metal-organic layers I^1O^2	3-D Coordination polymers with inorg. chains I^1O^3	I1
Molecular Complexes I^0O^0	Chain coordination polymers I^0O^1	Layered coordination polymer I^0O^2	3-D Coordination polymers with inorg. clusters I^0O^3	I0
O0	O1	O2	O3	

(a)

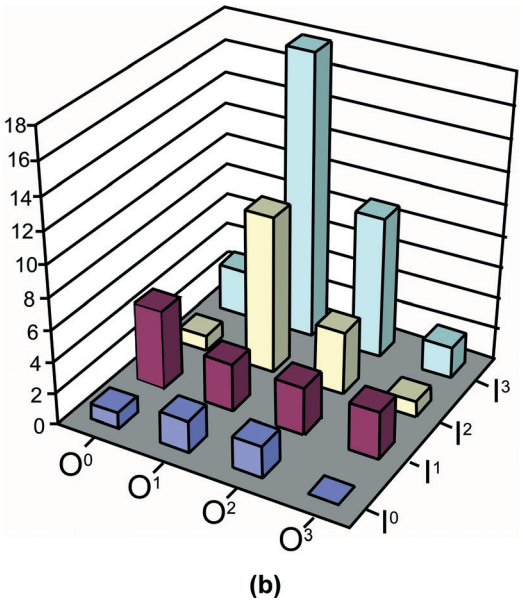

(b)

Fig. 8 (a) Cheetham *et al.* classification of inorganic–organic materials. The red boxes have been completed by taking into account the structural archetypes observed in hybrid vanadates. (b) The number of hybrid vanadates constructed from bridging ligands classified according to Cheetham *et al.* nomenclature.

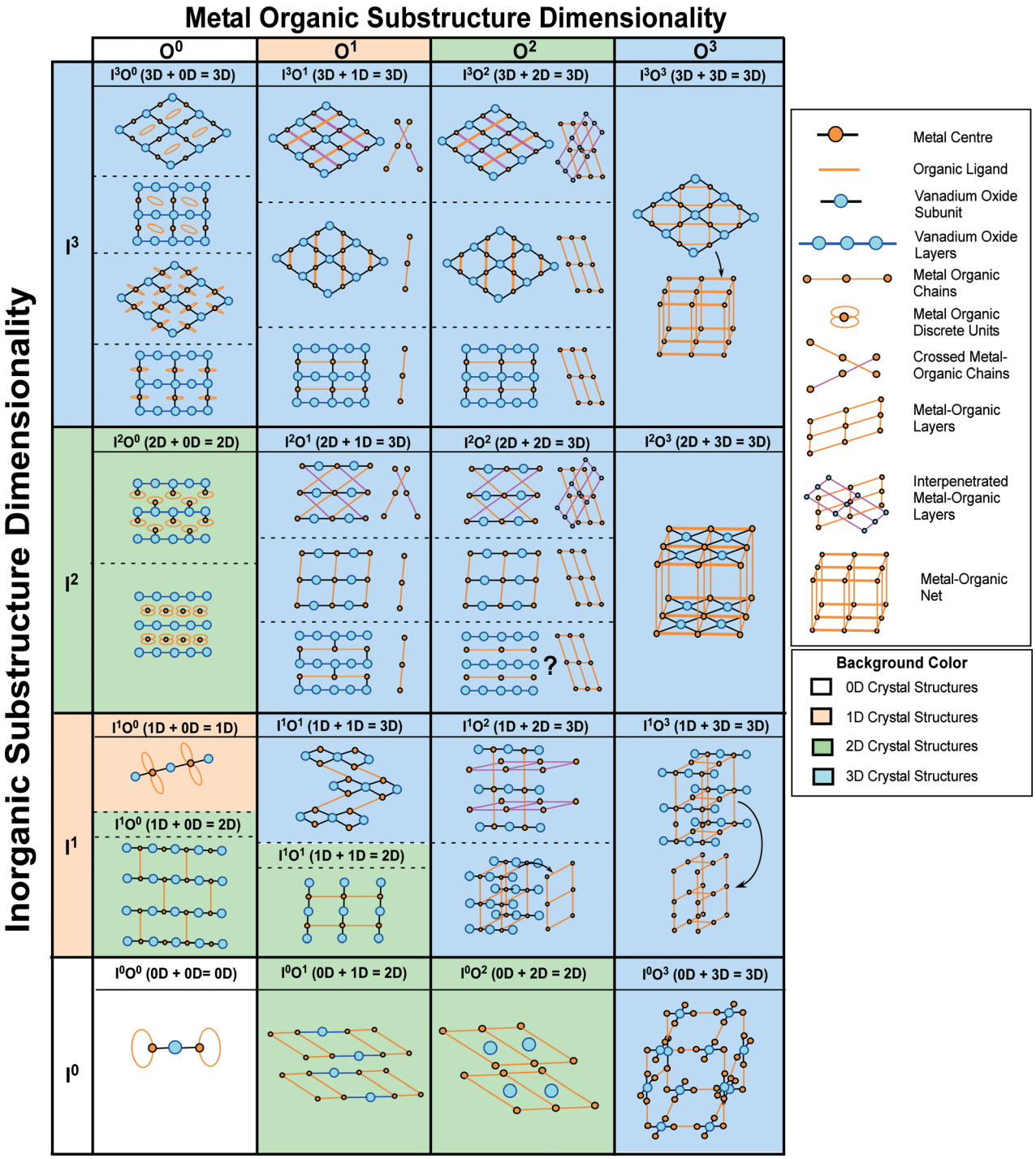

Fig. 9 Schematic representation of the different structural archetypes observed in hybrid vanadates.

metal–organic substructure simplification has been depicted next to the simplified model. The metal centres and VOS have been simplified as nodes of the nets, while the ligands have been represented as connectors between metal centres. In the specific case of chelating ligands, one line connects one metal centre twice. The vanadium oxide layers have been simplified as connected VOS.

The background colour in Fig. 9 is related to the crystal structure dimensionality within the different structural archetypes. On the other hand, we have observed that crystal structures classified within the same I^nO^m code could present different structural organizations of the metal–organic and inorganic skeletons. A clear example in regard to this is that of the I^2O^0 architectures, with two different subclasses of crystal archetypes constructed from different arrangements of the metal–organic discrete units and the vanadium oxide layers. In the first architecture, the organic ligand chelates the metal centre, and this ligand is linked directly to the

VOS, while in the second type, discrete metal–organic units are disposed between the vanadium oxide layers (see Fig. 9, I^2O^0 box).

In the following section, the crystal structures observed for each I^nO^m archetype will be described and discussed. The main discussion of this highlight will be focused on HV constructed from bridging ligands, but for the sake of comparison, several examples of HV constructed from chelating ligands have been also briefly mentioned.

In Tables 1–6, most of the HV constructed from dipodal and multi-podal organic ligands are included. The VOS and metal–organic substructure are briefly described. The coordination environment and oxidation state of the vanadium atoms are also mentioned. The crystal structures have been classified according to the metal–organic and inorganic substructure dimensionalities, as it has been previously explained. The CSD (Cambridge Structural Database) reference codes for the compounds are also shown when available.

3. Crystal architectures

3.1. I^3O^m (m = 0–3) architectures: hybrid vanadate archetypes containing three-dimensional inorganic scaffolds

The I^3O^m crystal architectures are characterized by three-dimensional inorganic substructures constructed from linkages between the secondary metal centres and the VOS. According to the metal–organic substructure dimensionality, four archetypes of I^3O^m crystal structures can be distinguished: I^3O^0, I^3O^1, I^3O^2 and I^3O^3.

Among the I^3O^0 architectures, there are four different types of structures, as shown in Scheme 1. The HV belonging to the two first types (Scheme 1(a) and (b)) possess organic molecules not bonded to the inorganic substructure, thus, in fact, the metal–organic substructure does not exist. In this sort of structure, the organic molecule is positively charged and acts compensating the charge of the inorganic skeleton. The main difference between the types observed in Scheme 1(a) and (b) is in the VOS. In the concrete case of the (b) type, the structures are constructed from vanadium oxide layers. These compounds are structurally similar to aluminophosphates or transition metal phosphates, arsenates, phosphites, germanates, *etc.* Several examples of HV belonging to this group are known, such as $\{Mn_3(en)\}(V_4O_{16})$,[29] $[\{Ni(enMe)_2\}_{0.5}(V_6O_{14})]\cdot(H_2enMe)_{0.5}$,[30] $[N(CH_3)_4]_2[Co(H_2O)_4(V_{12}O_{28})]$,[31] $[enH_2][Mn_3(V_2O_7)_2(H_2O)_2]$,[32] and $[C(NH_2)_3]_2[M^{II}(H_2O)_4(VO_3)_4]\cdot 4H_2O$, where M = Ni, Co, Mn.[33]

In the other two types of I^3O^0 vanadates (Scheme 1(c) and (d)), the organic molecule chelates the metal centre, and therefore the dimensionality of the metal–organic substructure does not extend, being 0D. Two examples of this architecture are $[\{Ni(Ht)\}(VO_3)_2]\cdot 0.33H_2O$ (Fig 10) and $[\{Cu(Ht)\}(VO_3)_2]\cdot 0.33H_2O$ (Ht = 5,5,7,12,12,14-hexamethyl-1,4,8,11-tetraazacyclotetradecane) vanadates.[34] The equatorial plane of nickel(II) and copper(II) atoms consists of four nitrogen atoms belonging to the Ht organic ligand. The axial oxygen atoms of the secondary metal centre are shared with the metavanadate chains, generating porous 3D frameworks whose channels are filled with crystallization water molecules.

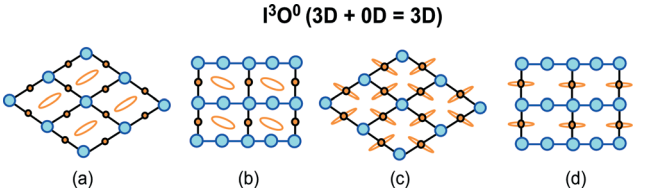

Scheme 1 Structural types in the I^3O^0 group.

Another I^3O^0 (b) type compound is the $\{Cu_2(Pz)\}(V_4O_{12})$[42] HV, in which two copper(II) atoms are linked through the Pz ligand, generating discrete metal–organic units. Within this category, a great number of HV with chelating ligands, such as ethylenediamine, *N*,*N*-bis(3-aminopropyl)ethylenediamine, and 1,3-diaminopropane, among others, have been reported.[35]

Two interesting examples of the I^3O^0 group containing bridging oxalate ligands are $(en)[\{Co_2(Ox)\}(V_4O_{12})]$ and $(H_2pn)[Mn_2(Ox)(V_4O_{12})]$ HV.[77,78] These compounds combine discrete metal–oxalate dimers linked through the $\{V_4O_{12}\}$ cycles, giving rise to 3D + 0D → 3D inorganic–organic scaffolds. The protonated amines act as templates compensating for the negative charge of the inorganic–organic skeleton, stabilizing the framework *via* weak interactions.

When the ligand acts as a bridge between metal centres, a polymeric metal–organic substructure is generated and the crystal architectures are classified as I^3O^1 when the linkage between metal centres and bridging ligands produces chains, I^3O^2 when it generates layers, and I^3O^3 when it gives rise to 3D metal–organic nets.

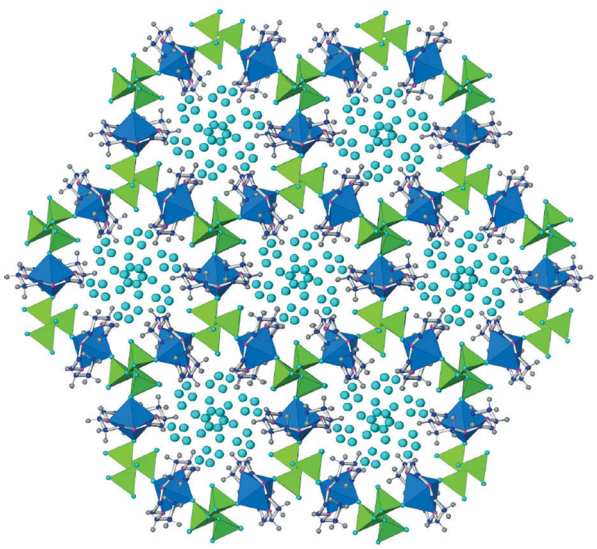

Fig. 10 Crystal structure of $[\{Ni(Ht)\}(VO_3)_2]\cdot 0.33H_2O$ (green polyhedra: metavanadate chains constructed from corner-linked VO_4 tetrahedra, blue polyhedra: NiN_4O_2 octahedra, cyan spheres: crystallization water molecules).[34]

Among the I^3O^1 crystal structures, the disposition of the metal–organic chains with respect to each other and the vanadate substructure are the main characteristics that define the three different types within this group (see Scheme 2). The structural archetypes shown in Scheme 2(a) and (b) correspond to three-dimensional crystal structures constructed from crossed or parallel metal–organic chains linked through the VOS. The connectivity between the VOS and the transition metal centres gives rise to three dimensional inorganic frameworks.

The metal–organic chains can present a crossed disposition (see Scheme 2(a)), as in $\{M(Pz)\}(VO_3)_2$, where M = Ni, Co, $[\{Ni_6(H_2O)_{10}(4Bpy)_6\}(V_{18}O_{51})]\cdot 1.5H_2O$, and $[\{Ni(H_2O)_2(Bpe)\}(V_4O_{11})]\cdot 0.5H_2O$ HV, as shown in Fig. 11.[36,38,46] The crystal structures of these compounds exhibit a rhombic-like inorganic skeleton stabilized by the organic ligands. The Ni–Pz, Ni–4Bpy and Ni–Bpe metal–organic chains show a crossed disposition within the crystal structure. The main difference between these crystal structures lies in the VOS. The $[\{Ni_2(H_2O)_4(Bbi)_2\}(VO_3)_4]\cdot 2H_2O$ (ref. 61) compound exhibits a similar crystal architecture, however, the metal–organic chains are undulated due to the flexibility of the Bbi ligand.

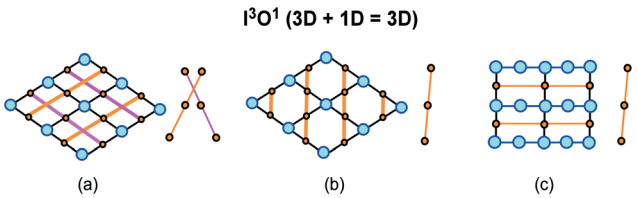

Scheme 2 Structural types in the I^3O^1 group.

A parallel disposition of the metal–organic chains to each other is observed in the second type of I^3O^1 (see Scheme 2(b)). In the specific case of $\{Ni_3(Pz)_3\}(V_8O_{23})$[40] HV, the metal–organic chains possess a *trans–trans–cis* connectivity, instead of the linear linkage observed for the previously described compounds. The same structural arrangement showed by the previously described compounds is observed for $\{Co(H_2O)(Bbi)\}(VO_3)_2$ (ref. 61) HV, with $\{Co(Bbi)\}$ undulated metal–organic chains.

In $\{Ni_2(H_2O)_2(Bpa)_2\}(V_6O_{17})$,[59] the Ni(II) octahedra are directly coordinated to the Bpa ligands, generating $\{NiBpa\}_n$ chains parallel to the vanadium oxide chains. Fig. 12(a) shows the crystal structure of $\{Ni_2(H_2O)_2(Bpa)_2\}(V_6O_{17})$. Each metal–organic chain is connected to vanadium oxide chains in three different directions, while the VOS are linked to six different metal–organic chains. Fig. 12(b) shows the connectivity between the V_2O_7 dimers and the $\{V_4O_{12}\}$ cycles with the Ni(II) cations. The Bpa organic ligands have been simplified as connectors between the Ni(II) metal centres.

$M_4(2\text{-Pzc})_4(V_6O_{17})$, where M = Ni, Co, and $[(NH_4)_2Co_8(H_2O)_2(2\text{-Pzc})_8(VO_3)_{10}]\cdot xH_2O$ compounds also exhibit the I^3O^1 crystal architecture constructed from $\{M(2\text{-Pzc})\}$ metal–organic chiral tubes based on metal–ligand helical chains.[79] The disposition of these tubular metal–organic

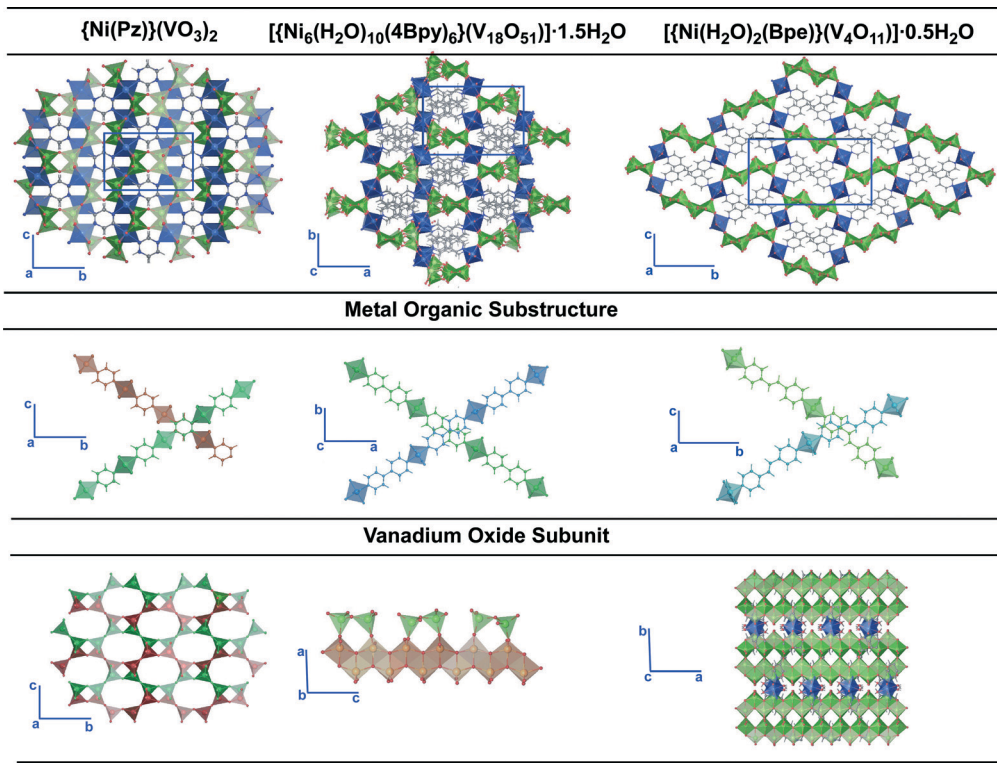

Fig. 11 Crystal structures, metal–organic substructures and vanadium oxide subunits for $\{M(Pz)\}(VO_3)_2$, (M = Ni, Co), $[\{Ni_6(H_2O)_{10}(4Bpy)_6\}(V_{18}O_{51})]\cdot 1.5H_2O$ and $[\{Ni(H_2O)_2(Bpe)\}(V_4O_{11})]\cdot 0.5H_2O$.[36,40,46]

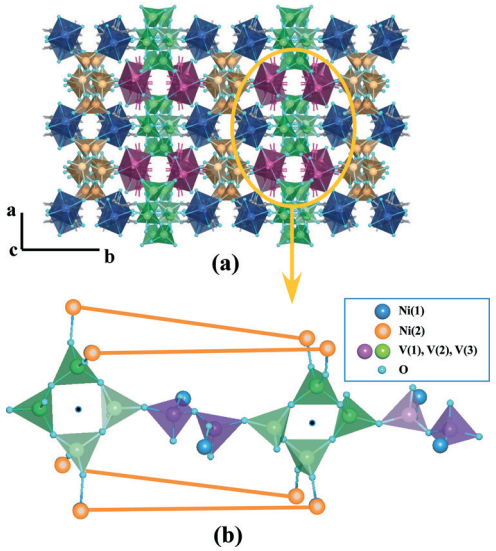

Fig. 12 (a) Crystal structure of $\{Ni_2(H_2O)_2(Bpa)_2\}(V_6O_{17})$ (blue and purple: $NiN_2O_3(H_2O)$ polyhedra; orange and green: metavanadate chains). (b) Connectivity between the $\{V_4O_{12}\}$ cycles and $\{V_2O_7\}$ dimers and the metal–organic chains in $\{Ni_2(H_2O)_2(Bpa)_2\}(V_6O_{17})$. The Bpa ligands have been simplified as lines.[59]

chains (purple polyhedra in Fig. 13) and the double metavanadate chains (green polyhedra in Fig. 13) in the 3D porous crystal structures of $M_4(2\text{-Pzc})_4(V_6O_{17})$, where M = Ni, Co, and $[(NH_4)_2Co_8(H_2O)_2(2\text{-Pzc})_8(VO_3)_{10}]\cdot xH_2O$ are shown in Fig. 13.

Another I^3O^1 compound is $\{Co_2(H_2O)(2\text{-Pzc})\}(VO_3)_3$.[38] The metal–organic chains in $\{Co_2(H_2O)(2\text{-Pzc})\}(VO_3)_3$ (ref. 38) are constructed from Co(II) dimeric units linked by the 2-Pzc ligand. The metavanadate chains are also parallel to the metal–organic chains, and their linkage generates a 3D compact crystal structure, instead of the porous framework observed within the helical tubes of $M_4(2\text{-Pzc})_4(V_6O_{17})$ (M = Ni, Co) and $[(NH_4)_2Co_8(H_2O)_2(2\text{-Pzc})_8(VO_3)_{10}]\cdot xH_2O$. The choice of unsymmetrical ligands such as 2-Pzc introduces chirality into the structures, demonstrating that this may be a good approach to obtain microporous chiral compounds.[79]

Finally, there are some I^3O^1 architectures exhibiting metal–organic chains arranged parallel between vanadium oxide layers (see Scheme 2(c)). There is only one example belonging in this group, the $\{M(Pz)\}(V_4O_{10})$ (M = Ni(II), Co(II), Zn(II)) HV. This family of compounds is characterized by their vanadium oxide layers formed by the corner linkage of double zigzag chains of edge-sharing VO_5 polyhedra. The layers contain a mixture of V(V)/V(IV) with a five coordination environment. The VO_5 polyhedra are connected to the metal centres through oxo groups, giving rise to a three-dimensional inorganic framework.

Within the I^3O^2 archetype, two different arrangements of the metal–organic layers have been observed, interpenetrated (Scheme 3(a)) and parallel (Scheme 3(b) and (c)) metal–organic layers. The main difference between the structural models shown in Scheme 3(b) and (c) is the VOS. In the type shown in Scheme 3(b), the parallel metal–organic layers are connected through the VOS, generating a three-dimensional inorganic framework. In the structural type shown in Scheme 3(c), the metal–organic layers are parallel to the vanadium oxide layers. The metal centres act as bridges between adjacent vanadium oxide layers, establishing a three-dimensional inorganic framework.

In the first group of I^3O^2 architectures (Scheme 3(a)), the metal centres are connected in two different directions through a dipodal ligand, generating a square-like architecture as in $(\{M_2(Bpp)_4\}(V_4O_{12})$ (M = Ni, Co) and $\{Co_3(H_2O)(Btb)_5\}(V_8O_{23}))$, or rectangular-like tilted interpenetrated metal–organic sheets as in $([\{M_2(H_2O)_2(4Bpy)_3\}(V_4O_{12})]\cdot 2.5H_2O$, M = Ni(II), Co(II))[44,45,66,67,70] The crystal structure and metal–organic network of the latest compound are shown in Fig. 14. The vanadate chains (green polyhedra in Fig. 14(a)) are located between the metal centres of different metal–organic layers, connecting them to generate a three-dimensional inorganic framework. The crystal structure shows rhombic channels along the [001] direction in which crystallization water molecules are located

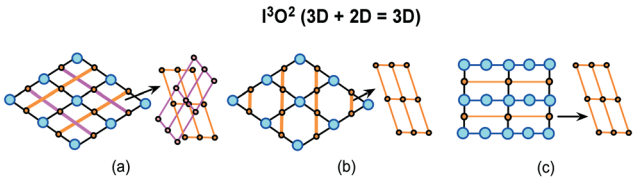

Scheme 3 Structural types in the I^3O^2 group.

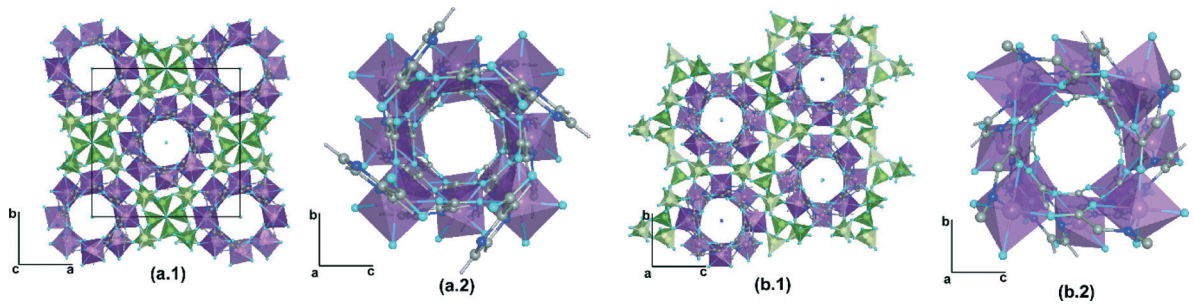

Fig. 13 Crystal structures of (a.1) $M_4(2\text{-Pzc})_4(V_6O_{17})$, where M = Ni, Co, and (b.1) $[(NH_4)_2Co_8(H_2O)_2(2\text{-Pzc})_8(VO_3)_{10}]\cdot xH_2O$ showing the metal–organic chiral tubes ((a.2) and (b. 2)) (purple polyhedra) connected by the metavanadate chains (green polyhedra).[79]

(red spheres). The interpenetration between the rectangular like metal–organic layers is observed in Fig. 14(b).

The $[\{Cu_3(H_2O)_2(Tpp)_2\}(V_8O_{23})]\cdot 3H_2O$ and $[\{Zn_3(H_2O)_2(Tpp)_2\}(VO_3)_6]\cdot 6H_2O$ (ref. 74) compounds exhibit a three-dimensional inorganic framework and parallel interpenetration of hexagonal-like metal–organic layers (3D + (2D + 2D) → 3D), instead of the previously described inclined interpenetration (see Scheme 3(b)).

Fig. 15(a) shows the crystal structure of $[\{Cu_3(H_2O)_2(Tpp)_2\}(V_8O_{23})]\cdot 3H_2O$.[74] The three-dimensional inorganic framework is similar to those observed in the I^3O^1 structural group, with honeycomb-like arrangement of the metal centres and the VOS. As shown in Fig. 15(b), the hexagonal-like metal–organic substructures are clearly related to the geometry of the Tpp ligand. The crystal structure contains two parallel interpenetrated hexagonal metal–organic nets (Fig. 15(b)). $[\{Cu_3(H_2O)_2(Tpp)_2\}(V_8O_{23})]\cdot 3H_2O$ is a unique HV that exhibits 2D undulated vanadium oxide layers constructed exclusively from four coordinated vanadium (Fig. 15(c) and (d)). These inorganic layers are interconnected with the interpenetrated metal–organic sheets, generating one of the most amazing and complicated examples of crystal structures observed in HV.

While the previous examples of I^3O^2 crystal architectures are constructed from interpenetrated metal–organic frameworks, the $\{Cu_3(1,2,4Trz)_2\}(V_4O_{12})$ compound possesses parallel non-interpenetrated $\{Cu_3(1,2,4Trz)_2\}$ metal–organic layers (Scheme 3(b)). Fig. 16(a) shows the six-coordinated copper cations. These octahedra share edges to form trimeric units. Each trimetric unit is connected to other four *via* triazole ligands, giving rise to two-dimensional $\{Cu_2(1,2,4\text{-}Trz)_3\}$ ruffled layers with an amplitude of about 4.75 Å and a period of 8.87 Å (Fig. 16(b)). Metavanadate chains are located between adjacent ruffled layers connecting Cu(II) metal centres

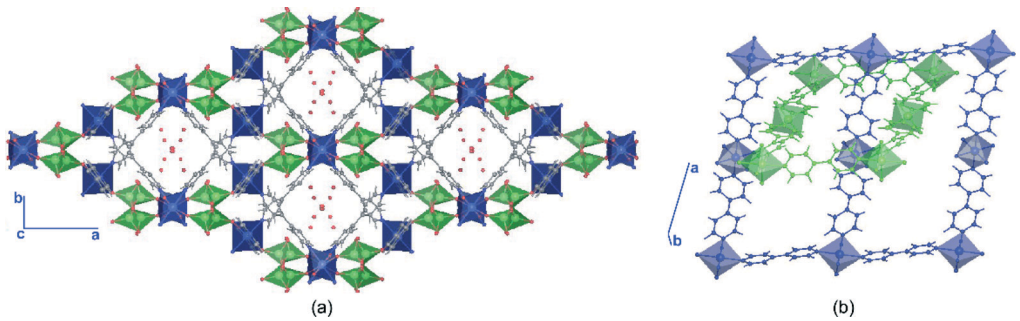

Fig. 14 (a) 3D porous crystal structure of $[\{M_2(H_2O)_2(4Bpy)_3\}(VO_3)_4]\cdot 2.5H_2O$ (M = Ni, Co) (green polyhedra: metavanadate chains, blue polyhedra: Ni(II) octahedra, red spheres: crystallization water molecules). (b) Metal–organic substructure constructed from the interpenetration of two rectangular-like layers. The metal–organic layers have been represented with different colours (green and blue) in order to easily visualize the interpenetration of the nets.[44,45]

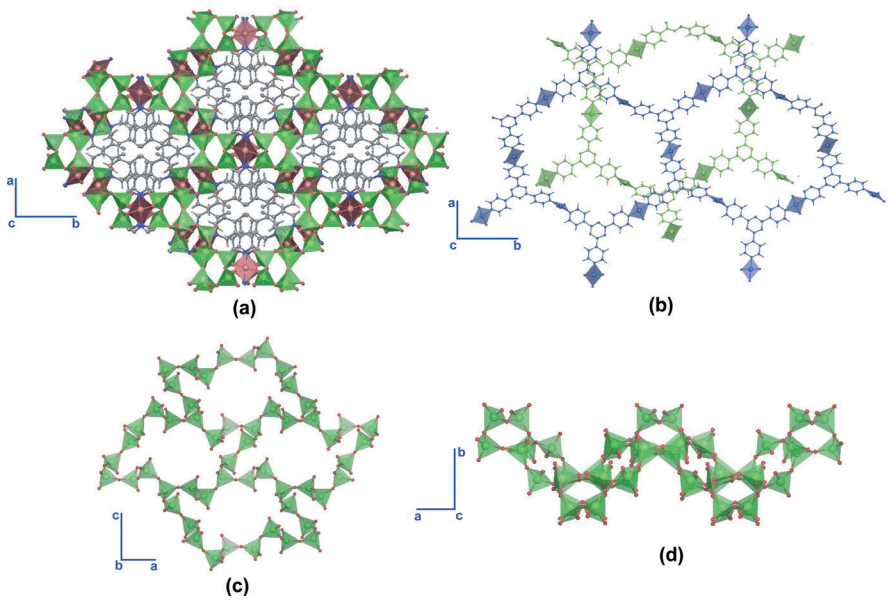

Fig. 15 (a) Crystal structure of $[\{Cu_3(H_2O)_2(Tpp)_2\}(V_8O_{23})]\cdot 3H_2O$ (green polyhedra: metavanadate chains, brown polyhedra: copper square planar polyhedra). (b) Parallel interpenetration of hexagonal-like metal–organic layers. (c) and (d) Vanadium oxide layers constructed from corner-sharing VO_4 tetrahedra.[74]

(Fig. 16(c)). The linkage between the vanadate chains and the copper cations generates a three-dimensional inorganic framework.

In $[\{Cu(Pz)_2\}(V_6O_{16})]\cdot 0.22H_2O$, an example of the third type of the I^3O^2 structural group (Scheme 3(c)), there are no interpenetrated layers. In contrast, the metal–organic sheets are disposed between the vanadium oxide layers and parallel to them. In the $[\{Cu(Pz)_2\}(V_6O_{16})]\cdot 0.22H_2O$ structure,[41] Cu(II) cations are linked in two directions through the Pz ligands, generating square-like metal–organic layers. The octahedral coordination environment of the Cu(II) cations is completed by two oxygen atoms shared by the adjacent vanadium oxide layers.

The I^3O^3 archetype is characterized by the coexistence of both 3D inorganic and metal–organic substructures (Scheme 4).

$[\{Ni_8(4Bpy)_{16}\}(V_{24}O_{68})]\cdot 8.5H_2O$ (ref. 47) and $[\{Ni_3(H_2O)_3(Bpa)_4\}(V_6O_{18})]\cdot 8H_2O$ (ref. 58) are examples of this structural group. The metal–organic substructure of $[\{Ni_8(4Bpy)_{16}\}(V_{24}O_{68})]\cdot 8.5H_2O$ consists of the polycatenation of a cadmium sulphate "CdS"-like 3D metal–organic net with two square-like metal–organic layers (Fig. 17(a)). The vanadium oxide chains are located in the channels of the metal–organic substructure and linked *via* corners to the Ni(II) cations (Fig. 17(b)). Fig. 17(c.1) and (c.2) depict the connectivity between the VO_4 tetrahedra belonging to the metavanadate chains and the Ni(II) metal centres within the metal–organic substructure.

The metal–organic substructure of $[\{Ni_3(H_2O)_3(Bpa)_4\}(V_6O_{18})]\cdot 8H_2O$ (ref. 58) is constructed from the interpenetration of three 3D metal–organic nets. The VOS consists of $\{V_{12}O_{36}\}$ vanadate cycles, which act as four connectors between metal centres of two different metal–organic nets. The combination of both the 3D metal–organic and the inorganic scaffolds generates a ten-connected porous crystal structure. Remarkable characteristics of this compound are the coexistence of the Bpa ligand in both "*gauche*" and "*trans*" conformations and the fact that the Ni(II) dimers belonging to the metal–organic nets lie inside the $\{V_{12}O_{36}\}$ cycles connected to them *via* oxo groups.

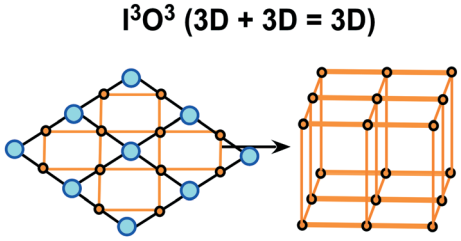

Scheme 4 Structural type in the I^3O^3 group.

3.2. I^2O^n (n = 0–3) architectures: hybrid vanadate archetypes containing two-dimensional inorganic layers

In I^2O^n architectures, the inorganic substructure is 2D. Depending on the dimensionality of the metal–organic substructures, four archetypes can be described: I^2O^0, I^2O^1, I^2O^2 and I^2O^3.

Two major types of I^2O^0 architectures can be distinguished (Scheme 5). In the first arrangement of the I^2O^0 archetype, the secondary metal is bonded to the vanadate layers and the ligand chelates the metal, generating 2D inorganic–organic layers stabilized by weak interactions (Scheme 5(a)), while the second arrangement is characterized by having discrete metal–organic complexes between the vanadate layers (Scheme 5(b)).

Examples of these kind of architectures are: $\{Co(Phen)_3\}(V_{10}O_{27})$,[83] $\{Co_2(2Bpy)_2\}(V_6O_{17})$,[84] $\{Co_2(Phen)_4\}(V_8O_{23})$,[85] and $\{Zn(Tpp)_2\}(VO_3)_2$,[74] among others.[86]

In I^2O^1 and I^2O^2 structural groups, three closely related types have been observed (see Schemes 6 and 7). The main difference between the I^2O^1 and I^2O^2 structures is the existence of metal–organic chains or metal–organic layers within the crystal framework.

In the I^2O^1 and I^2O^2 structures observed in Schemes 6(a)–(b) and 7(a)–(b), respectively, the VOS are linked to the metal centres, generating inorganic layers. The ligand is directly attached to the metal centres and acts as a pillar between the inorganic layers. The metal–organic chains or layers can acquire a crossed (Schemes 6(a) and 7(a)) or a parallel disposition (Schemes 6(b) and 7(b)) within the crystal structures.

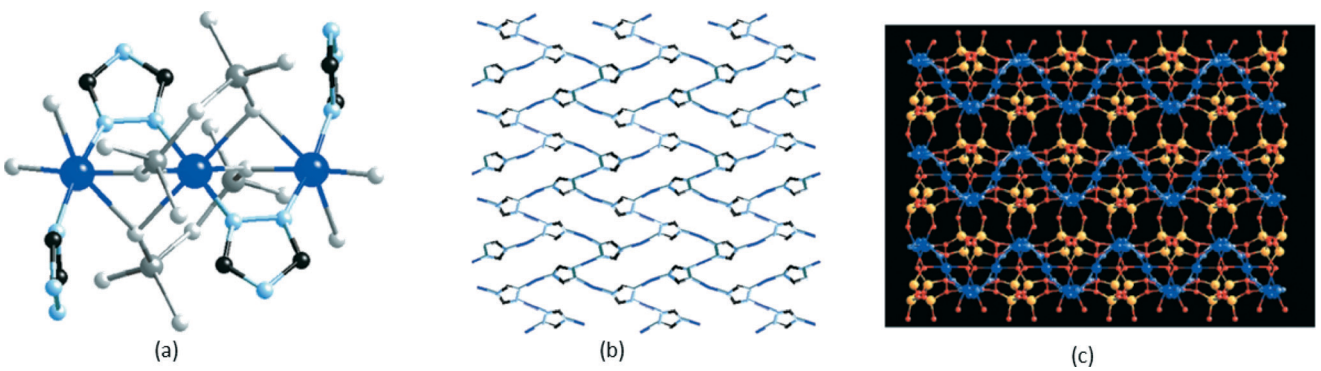

Fig. 16 (a) Trimeric units of $\{Cu_3(1,2,4\text{-}Trz)_2\}(V_4O_{12})$ (blue: copper atoms, grey: VO_4 tetrahedra, pale blue: nitrogen atoms, black: carbon atoms), (b) $\{Cu_3(1,2,4Trz)_2\}$ metal–organic layers, and (c) the crystal structure of $\{Cu_3(1,2,4Trz)_2\}(V_4O_{12})$ (blue: metal–organic layers, yellow: metavanadate chains). Reproduced from ref. 75 with permission of The Royal Society of Chemistry.

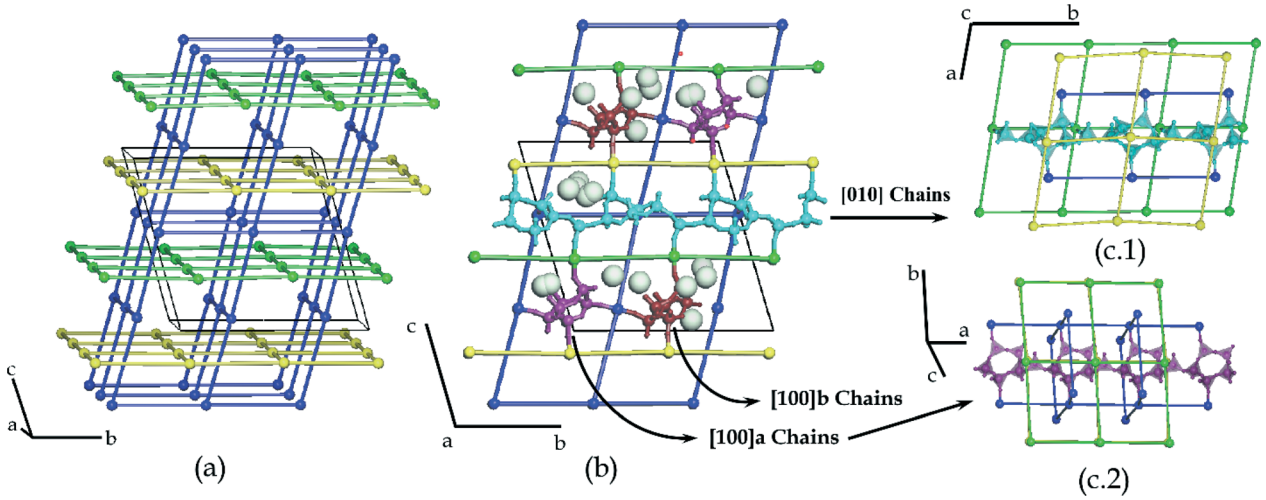

Fig. 17 (a) Metal–organic substructure of $[\{Ni_8(4Bpy)_{16}\}(V_{24}O_{68})]\cdot 8.5H_2O$ constructed from a "CdS"-like 3D net (blue) and two square-like (4,4)-c nets (yellow and green nets) (the Bpy organic ligands have been simplified as connectors, while the NiN_2O_4 octahedra have been simplified as the nodes of the metal–organic nets). (b) View of the crystal structure of $[\{Ni_8(4Bpy)_{16}\}(V_{24}O_{68})]\cdot 8.5H_2O$. The metavanadate chains (cyan, purple and maroon atoms) are located in the [100] and [010] channels. (c.1) and (c.2) Views of the connectivity between the metavanadate chains and the Ni(II) metal centres belonging to the metal–organic nets.

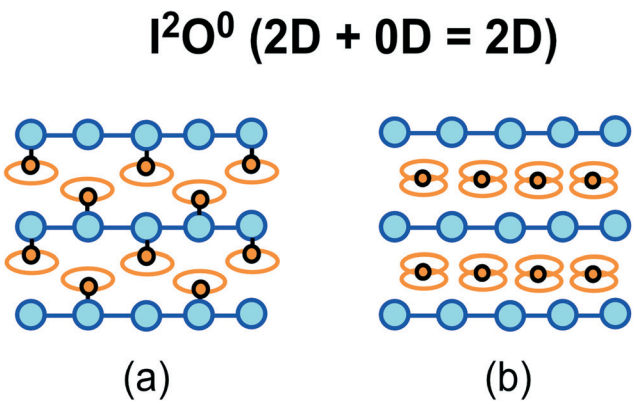

Scheme 5 Structural types in the I^2O^0 group.

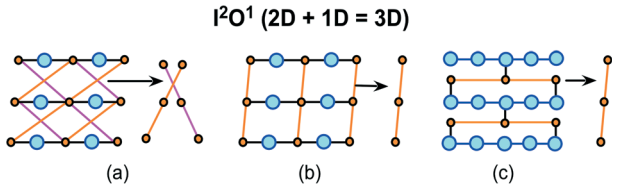

Scheme 6 Structural types in the I^2O^1 group.

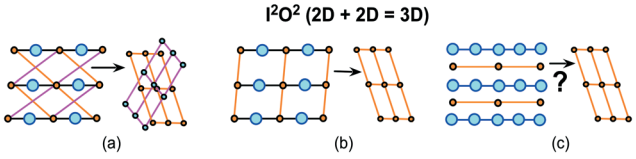

Scheme 7 Structural types in the I^2O^2 group.

Examples of the I^2O^1 structural archetype shown in Scheme 6(a) are the $[\{M(H_2O)_2(Bpe)_2\}(V_4O_{12})]\cdot 4H_2O\cdot Bpe$ (M = Ni, Co) hybrid vanadates. These compounds exhibit a crossed disposition of the M(Bpe) chains within the crystal structure. Moreover, the crystal structure possesses Bpe solvent molecules located in the channels between the inorganic layers. The hydrogen bonding network between the Bpe guest molecules and the crystallization and coordination water molecules is a key factor in the stabilization of the crystal framework.

$\{Ni_2(H_2O)_2(Pz)\}(V_4O_{12})$, $\{Co(4Bpy)\}(VO_3)_2$, $\{Co(Bpa)\}(VO_3)_2$, $[\{Ni(H_2O)(Bpa)\}(VO_3)_2]\cdot 2H_2O$, $\{M_2(H_2O)_2(Bbi)\}(VO_3)_4$ (M = Mn(II), Co(II)), $[\{Ag(4Bpy)\}_4(V_4O_{12})]\cdot 2H_2O$ and $\{Cu_3(Trz)_2\}(V_4O_{12})$ HV belong to the I^2O^1 structural types shown in Scheme 6(b).[39,40,48,57,73] Fig. 18(a.1), (b.1) and (c.1) show the crystal structures of $\{Co(4Bpy)\}(VO_3)_2$, $\{Co(Bpa)\}(VO_3)_2$ and $[\{Ni(H_2O)(Bpa)\}(VO_3)_2]\cdot 2H_2O$, respectively. The inorganic layers of these three compounds are constructed from $\{V_4O_{12}\}$ cycles connected to six metal centres, and each metal centre is linked to three $\{V_4O_{12}\}$ cycles (Fig. 18(a.2), (b.2) and (c.2)). The most remarkable differences between these crystal structures are the coordination environment of the metal centres and the tilt angle of the organic ligand.

In $\{Ni(Bpe)\}(VO_3)_2$ (ref. 52 and 53), the metal centres share edges with each other, generating dimeric units. Each dimeric unit is connected to another four through the organic ligand, giving rise to interpenetration of two square-like metal–organic layers within the crystal structure (Fig. 19). The metal centres are also connected through the metavanadate chains, giving rise to a ten-connected self-catenated crystal structure. This compound is an example of the I^2O^2 structural group with the interpenetrated metal–organic layers shown in Scheme 7(a). Fig. 19 shows the crystal structure of $\{Ni(Bpe)\}(VO_3)_2$, as well as the crossed disposition of the Bpe organic ligands between the inorganic layers.

The second type of I^2O^2 compounds presents parallel instead of crossed metal–organic layers (see Scheme 7(b)). Examples of this I^2O^2 architectures are $[\{Mn(4Bpy)\}(VO_3)_2]\cdot$

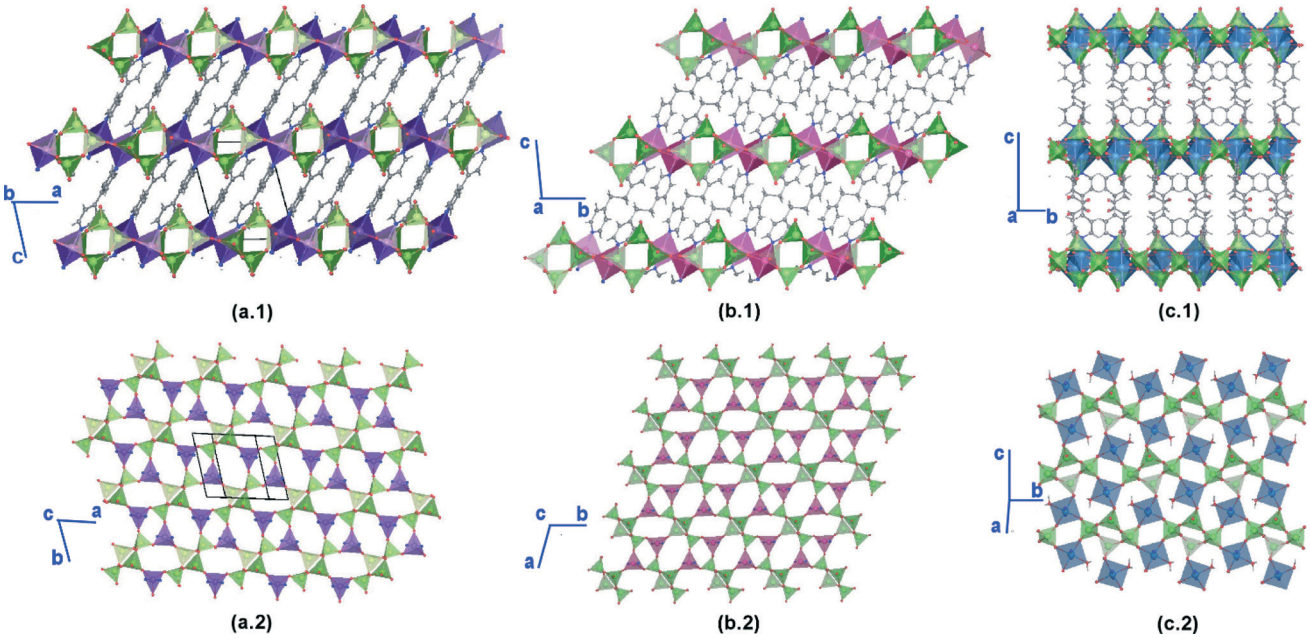

Fig. 18 (a.1), (b.1) and (c.1) Crystal structures of $\{Co(4Bpy)\}(VO_3)_2$, $\{Co(Bpa)\}(VO_3)_2$ and $[\{Ni(H_2O)(Bpa)\}(VO_3)_2]\cdot 2H_2O$. (a.2) and (b.2) Inorganic layers constructed from CoN_2O_3 and $\{V_4O_{12}\}$ cycles. (c.2) Inorganic layers constructed from $Ni(H_2O)N_2O_3$ octahedra and $\{V_4O_{12}\}$ cycles (green polyhedra: $\{V_4O_{12}\}$ cycles; purple, pink and blue polyhedra: coordination spheres of the secondary metal centres (Ni(II) and Co(II)).[57]

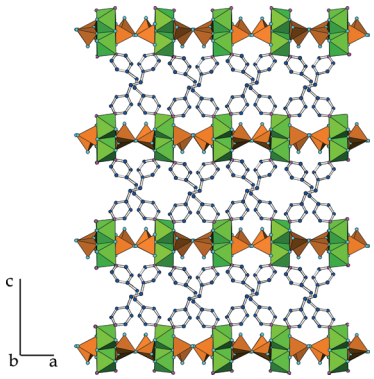

Fig. 19 Crystal structure of $\{Ni(Bpe)\}(VO_3)_2$ (green polyhedra: nickel octahedra, orange polyhedra: metavanadate chains).

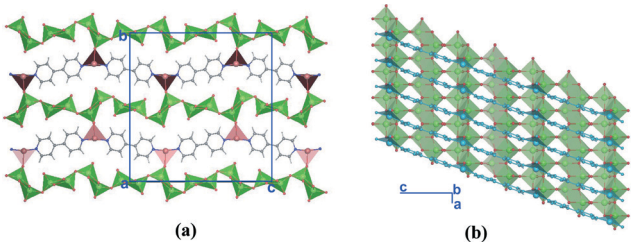

Fig. 20 (a) Crystal structure of $\{M(4Bpy)\}(V_4O_{10})$ (M = Cu, Ag). (b) Connectivity between the metavanadate layers (green polyhedra) and the metal–organic chains (brown polyhedra linked by the (Bpy) organic ligand in (a) and blue spheres in (b)).[49]

$1.16H_2O$, $[\{Mn(4Bpy)_{0.5}\}(VO_3)_2]\cdot 0.62H_2O$ (see Fig. 30, in section 4) and $[\{Ag(Bpa)\}_4(V_4O_{12})]\cdot 4H_2O$.[48,51] These structures present metal–organic Mn(4Bpy) and $\{Ag(Bpa)\}_4$ layers in which metal centres are connected through the vanadium oxide subunit, giving rise also to inorganic sheets.

In the third arrangement observed for I^2O^1 and I^2O^2 structural archetypes, the metal–organic chains or layers are disposed between vanadium oxide layers (see Schemes 6(c) and 7(c)). In the specific case of this type of I^2O^2 architectures, we have not found real examples. Regarding the third type of I^2O^1 (Scheme 6(c)), only one example is known, $\{M(4Bpy)\}(V_4O_{10})$ (M = Cu(I), Ag(I)).[38,49] Fig. 20(a) shows the crystal structure of $\{M(4Bpy)\}(V_4O_{10})$ (M = Cu(I), Ag(I)) HV. Cu(I)–Bpy metal–organic chains are located between the vanadium oxide layers, and the copper metal centres are connected *via* oxo groups to the VO_5 polyhedra of one layer. If the connectivity through the organic ligand is taken into account, the crystal structure is three-dimensional, but the inorganic framework is two-dimensional, because the copper atoms only connect one of the layers through oxo groups. The disposition of the Cu–Bpy metal–organic chains in the vanadium oxide layers is shown in Fig. 20(b).

There is only one example of the I^2O^3 architecture, $\{Ag_4(2\text{-}Pzc)_2\}(V_2O_6)$ (see Scheme 8). In this HV, clusters of four Ag atoms (Ag_4) are linked through two multi-podal 2-Pzc ligands, giving rise to a three-dimensional metal–organic

I^2O^3 (2D + 3D = 3D)

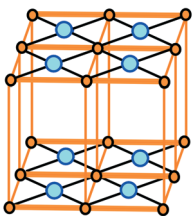

Scheme 8 Structural type in the I^2O^3 group.

framework. The metavanadate chains are located in the channels of the metal–organic substructure sharing corners with the silver clusters. In this case, the connectivity between the silver Ag_4 clusters and the metavanadate chains generates inorganic layers.

3.3. I^1O^n (n = 0–3) architectures: hybrid vanadate archetypes containing one-dimensional inorganic chains

There are few examples of HV containing 1D inorganic chains combined with different metal–organic units (I^1O^0), chains (I^1O^1), layers (I^1O^2) or nets (I^1O^3). The presence of dipodal ligands seems to favour the crystallization of the previously described structural archetypes instead of the crystal structures containing one-dimensional inorganic substructures. Despite this fact, this type of HV shows very interesting crystal structures and has more in common with the classic MOFs than the previously described HV.

In I^1O^0 archetypes, discrete metal–organic units are connected through discrete vanadium oxide units, giving rise to bimetallic inorganic chains (Scheme 9(a)) or layers (Scheme 9(b)).

Examples of the first type of I^1O^0 (Scheme 9(a)) are $\{Co(HBpe)_2\}(V_4O_{12})$,[54,55] $\{Cd(HBbi)_2\}(V_4O_{12})$,[60] $[\{Mn(Phen)\}(V_4O_{12})]\cdot 0.5H_2O$,[87] and $\{Co(2Bpy)_2\}(V_4O_{12})$,[88] among others. In these crystal structures, metal–organic complexes are joined through VOS, giving rise to a one-dimensional inorganic framework. The second type of I^1O^0 architecture (Scheme 9(b)) is observed in $[\{Cu_2(Bpq)\}(V_4O_{12})]\cdot 2H_2O$, $\{Zn_2(Btpt)\}(V_4O_{12})$ and $\{Co_2(Btpt)_2\}(V_4O_{12})$ HV.[72] In these structures, the metal centres of adjacent inorganic chains are connected through the organic ligand. The metal–organic substructure is 0D, but the connectivity through the organic molecule generates an increase in the crystal structure dimensionality, 1D + 0D → 2D.

Two different arrangements have been described for I^1O^1 (Scheme 10). Both types of I^1O^1 architectures consist of inorganic chains connected by the ligand. The linkage between the metal centres and the ligand also gives rise to 1D metal–organic chains. Consequently, an increase in the dimensionality of the crystal structure is observed. The difference between the crystal arrangements within this group lies in the final dimensionality of the crystal structure. The connectivity between metal–organic and inorganic chains could give rise to 3D (Scheme 10(a)) or 2D (Scheme 10(b)) crystal structures.

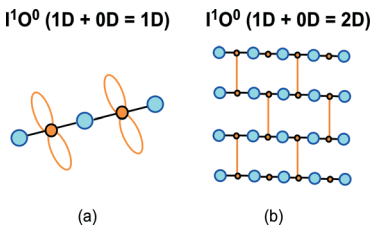

Scheme 9 Structural types in the I^1O^0 group.

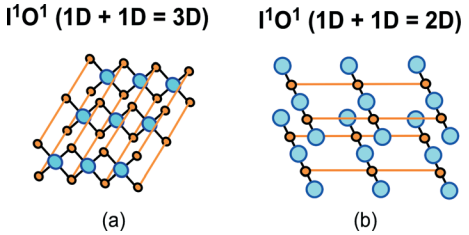

Scheme 10 Structural types in the I^1O^1 group.

The $[\{Cu(4Bpy)\}_4(V_4O_{12})]\cdot 2H_2O$ compound[50] (Fig. 21) is an example of the first type of I^1O^1 architecture (Scheme 10(a)). The inorganic chains of $[\{Cu(4Bpy)\}_4(V_4O_{12})]\cdot 2H_2O$ are formed by $\{V_4O_{12}\}$ cycles linked through Cu(I) cations, as shown in Fig. 21(a). A single inorganic chain is observed in Fig. 21(b) and a view of the structure of $[\{Cu(4Bpy)\}_4(V_4O_{12})]\cdot 2H_2O$ is shown in Fig. 21(c). Each inorganic chain is connected to another six through the organic ligand, generating a 3D crystal structure, 1D + 1D = 3D (Fig. 21(c)).

$[\{Co_2(Pcca)_2(H_2O)\}(VO_3)_2]$ is a unique example of the second type of I^1O^1 (Scheme 10(b)). This compound contains double metal–organic chains of $Co_2(Pcca)_2$. The metavanadate chains are parallel to the metal–organic chains and connect four $Co_2(Pcca)_2$ adjacent metal–organic chains, giving rise to a 2D inorganic–organic structure.[81]

The I^1O^2 crystal structures combine both inorganic chains and metal–organic layers. Two different arrangements have been observed for the I^1O^2 archetype (Scheme 11).

Only one example of the first type of I^1O^2 (Scheme 11(a)) has been described: $\{Cu_2(Bbi)_3\}(V_4O_{12})$.[76] The inorganic–organic layer of $\{Cu_2(Bbi)_3\}(V_4O_{12})$ HV has copper(II) cations that are linked alternatively to $\{V_4O_{12}\}$ cycles *via* vertexes, generating 1D inorganic chains (Fig. 22(a.1)). The copper(II) cations of adjacent inorganic chains are connected by Bbi ligands, as shown in Fig. 22(a.1). The metal–organic layer is a $\{Cu(Bbi)_2\}$ rhomboid-like sheet (Fig. 22(a.2)). Fig. 22(a.3) and (a.4) show two different views of the interpenetration between the $Cu(Bbi)(V_4O_{12})$ inorganic–organic layers and the $Cu(Bbi)_2$ metal–organic layers. The layers are represented with different colours (blue: inorganic–organic layers, green: metal–organic layers) in order to visualize better the arrangement between the two types of sheets. The interpenetration of these two types of layers generates a 3D framework without an increase in the dimensionality for the inorganic substructure because the metal–organic layers are not directly attached to the inorganic–organic ones, the interpenetration of which generates an increase in the dimensionality (Fig. 22(a.3) and (a.4)).

Two examples of the second type of I^1O^2 (Scheme 11(b)) have been reported, $\{Cu_3(Ptrz)_2\}(VO_3)_4$ (ref. 76) and $[\{Co(Pcca)_2(H_2O)\}(VO_3)_2]\cdot 3.62H_2O$.[82] $\{Cu_3(Ptrz)_2\}(VO_3)_4$ combines $\{Cu_3(PTrz)_2\}$ undulated layers (Fig. 22(b.2)) linked through metavanadate chains (Fig. 22(b.1)). The copper(II) metal centres connect the metavanadate chains, generating also 1D inorganic chains (Fig. 22(b.3)). The crystal structure is also described as 1D + 2D → 3D. $[\{Co(H_2O)(Pcca)_2\}(VO_3)_2]\cdot 3.62H_2O$ contains $\{Co(H_2O)(Pcca)_2\}$ metal–organic layers pillared by the $\{V_4O_{12}\}$ cycles, giving rise to a 3D architecture. The linkage between the Co(II) cations

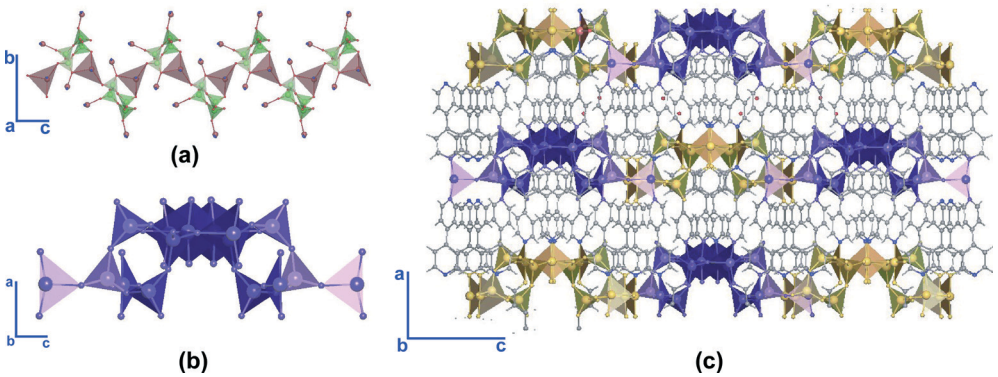

Fig. 21 (a) Inorganic chains (green polyhedra: $\{V_4O_{12}\}$ cycles, brown polyhedra: coordination sphere of copper cations). (b) View of the inorganic chains along the [010] direction. (c) Crystal structure of $[\{Cu(4Bpy)\}_4(V_4O_{12})]\cdot 2H_2O$. The inorganic chains have been represented with two different colours in order to help the reader to visualize the crystal structure.[50]

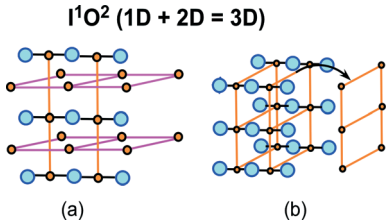

Scheme 11 Structural types in the I^1O^2 group.

and the $\{V_4O_{12}\}$ cycles generates $\{Co(V_4O_{12})\}$ inorganic chains running perpendicular to the metal–organic sheets (see Fig. 28).

The I^1O^3 structural group is similar to the I^1O^2 group, however, the metal centres are connected parallel to metal–organic layers through the ligands, generating a 3D metal–organic substructure (Scheme 12).

Concerning this type of architecture, $[\{M_2(Bbi)_3\}(V_4O_{12})]\cdot 4H_2O$ (M = Ni(II), Co(II))[62,63] possesses two interpenetrated 3D six-connected metal–organic nets (Fig. 23(a) and (b)). The dimers, belonging to the metal–organic substructure, are connected through $\{V_4O_{12}\}$ cycles giving rise to inorganic chains (Fig. 23(c)). Each dimer connects also six dimers through the organic linker. The crystal structure can be described as an eight-connected and self-catenated net, as shown in Fig. 23(d).

3.4. I^0O^n (n =0–3) architectures: hybrid vanadate archetypes containing discrete inorganic units

In the I^0O^m architectures, the inorganic substructure is 0D and acts as a node connected through the ligand, like in MOFs. Four different archetypes are described according

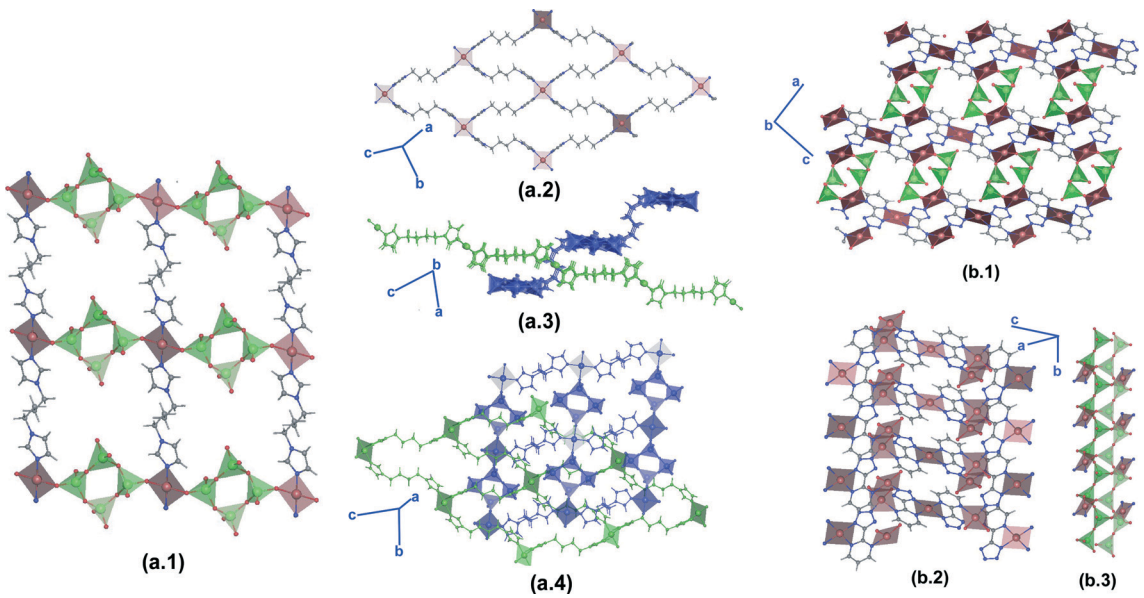

Fig. 22 (a.1) Inorganic–organic layers. (a.2) $\{Cu(Bbi)_2\}$ metal–organic layers. (a.3) and (a.4) Interpenetration of the metal–organic and inorganic–organic layers of $\{Cu_2(Bbi)_3\}(V_4O_{12})$.[60] (b.1) Crystal structure of $\{Cu_3(PTrz)_2\}(VO_3)_4$.[76] (b.2) $\{Cu_3(PTrz)_2\}$ metal–organic layers. (b.3) Inorganic chains (green polyhedra: $\{V_4O_{12}\}$ cycles, brown polyhedra: coordination environment of the copper cations). For (a.3) and (a.4), blue: inorganic–organic layers and green: metal–organic layers of $\{Cu_2(Bbi)_3\}(V_4O_{12})$.

to the metal–organic dimensionality, I^0O^0, I^0O^1, I^0O^2 or I^0O^3, for discrete, one-dimensional, two-dimensional or three-dimensional metal–organic substructures, respectively.

The I^0O^0 archetype is discrete coordination complexes commonly generated from chelating ligands (Scheme 13). The metal centres are linked to discrete VOS. This type of structural archetype in HV was deeply described by Zubieta *et al.*[7] An example of this architecture is the $[\{Cu_2(Btpt)_2\}(V_4O_{12})]$ compound.[73]

The I^0O^1 crystal structures contain metal–vanadate discrete units linked through the organic ligand. The connectivity between the metal centres and the organic ligand generates metal–organic chains. Two different types have been described (see Scheme 14).

The unique example of the first type of I^0O^1 archetype (see Scheme 14(a)) is $[\{Cu_2(Btpt)_2\}(V_4O_{12})]\cdot 2H_2O$. The main building block of this crystal structure is the Cu(Btpt) metal organic chains, which are linked through $\{V_4O_{12}\}$ cycles, giving rise to a 2D framework.

A very interesting example of the I^0O^1 group is the $[\{Cu_4(Bpp)_4\}(V_4O_{12})]\cdot 3H_2O$ vanadate.[71] This is the second type of I^0O^1 crystal architecture shown in Scheme 14(b). Each $Cu_4(V_4O_{12})$ inorganic cluster is connected to another eight, generating an unprecedented eight-connected self-catenated crystal structure (Fig. 24). The connectivity between the

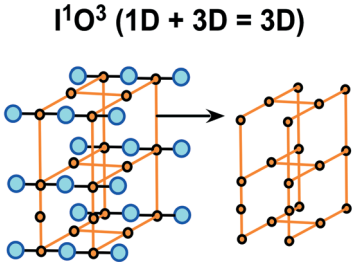

Scheme 12 Structural archetypes in the I^1O^3 group.

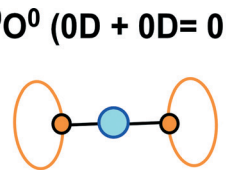

Scheme 13 Structural type in the I^0O^0 group.

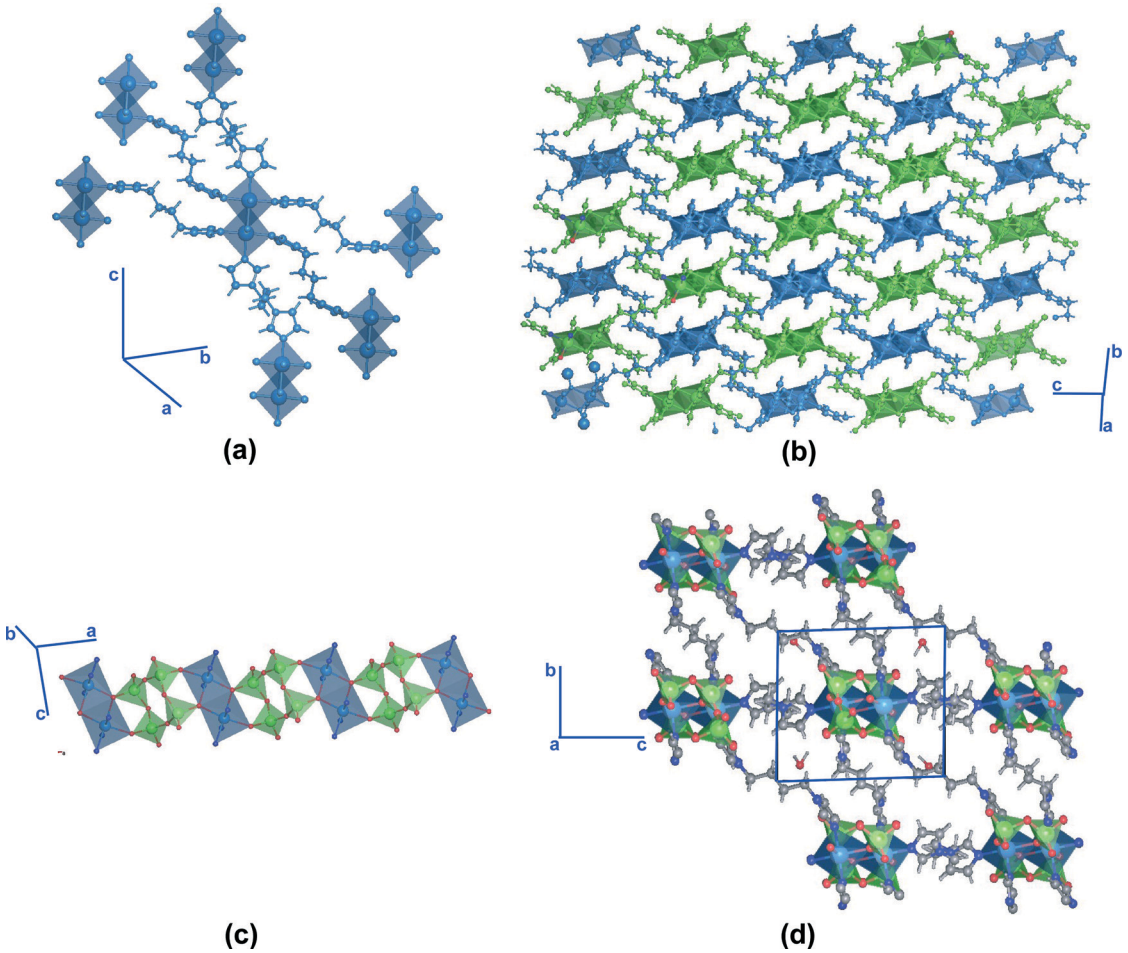

Fig. 23 (a) Six-connected dimeric units. (b) Two interpenetrating 3D metal–organic substructure. (c) Inorganic chains (green polyhedra: $\{V_4O_{12}\}$ cycles, blue polyhedra: Ni(II) octahedral coordination environment). (d) Eight-connected self-catenated structure constructed from inorganic chains and the metal–organic net of $[\{M_2(Bbi)_3\}(V_4O_{12})]\cdot 4H_2O$, where M = Ni(II), Co(II).[62,63]

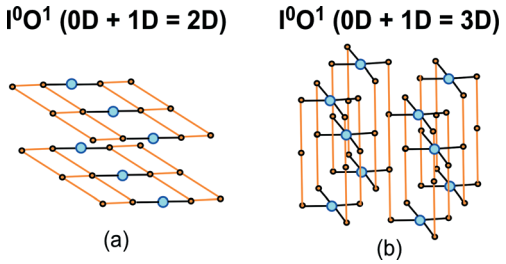

Scheme 14 Structural types in the I^0O^1 group.

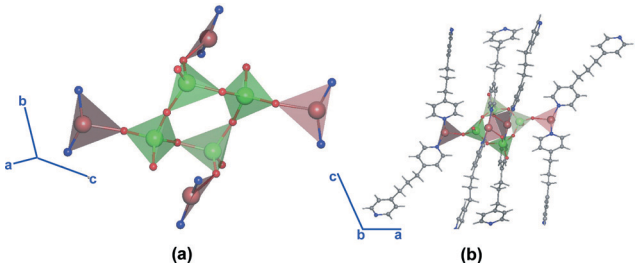

Fig. 24 (a) $Cu_4V_4O_{12}$ inorganic clusters present in the $[\{Cu_4(Bpp)_4\}(V_4O_{12})]\cdot 3H_2O$ structure. (b) Eight connected nodes (green polyhedra: $\{V_4O_{12}\}$ cycles, brown polyhedra: coordination polyhedra of the copper atoms).[71]

copper cations and the ligand generates metal–organic chains, rendering the linkage through the $\{V_4O_{12}\}$ cycles necessary to obtain the 3D eight-connected crystal structure.

The I^0O^2 architectures are very common in MOFs, however, only two examples are known in HV (Scheme 15).

In the first I^0O^2 structural archetype, the metal centres or clusters are linked through ligands in two different directions generating metal–organic layers, while the VOS are discrete and isolated in the structure (Scheme 15(a)) or act as connectors between the metal–organic layers (Scheme 15(b)).

Examples of I^0O^2 archetypes are $[\{Cu(Bbi)_2\}(V_4O_{12})]\cdot 4H_2O$ (ref. 64) and $\{Zn_2(Tp)(4\text{-}Bpy)\}(VO_3)_2$.[80] $[\{Cu(Bbi)_2\}(V_4O_{12})]\cdot 4H_2O$ is an example of the first type of I^0O^2 architecture (Scheme 15(a)). The crystal structure consists of $\{Cu(Bbi)_2\}$ metal–organic layers linked through weak interactions to $\{V_4O_{12}\}$ cycles. A very different I^0O^2 crystal structure is that of $\{Zn_2(Tp)(4\text{-}Bpy)\}(VO_3)_2$, a unique example of the second type of I^0O^2 crystal frameworks (see Scheme 15(b)). This compound combines both carboxylic terephthalate- and nitrogen-based 4,4′-bipyridine ligands. The mixed organic bridges interlink the Zn(II) dimers to generate cationic rectangular metal–organic grids. Zn ions of two adjacent metal–organic grids are connected through the $\{V_4O_{12}\}$ cycles to form a pillared double-layered sheet. As in many other MOF compounds, the double layers are polycatenated.

Despite the I^0O^3 crystal structures being extensively represented in MOFs, there are no examples in HV. In MOFs, the combination of metal centres or metal clusters and carboxylic ligands generates different families of coordination polymers exhibiting I^0O^3 architectures with very interesting physicochemical properties. A hypothetical HV of the I^0O^3 structural archetype is shown in the Scheme 16.

Hypothetically, the construction of I^0O^3 HV is possible through clusters constructed from discrete vanadium oxide subunits linked to secondary metal centres. This type of MOFs could be build from heterometallic clusters.

4. Physicochemical properties of hybrid vanadates

Physicochemical properties of HV depend on the crystal structures itself and on the fundamental building blocks used for the construction of these architectures. Establishing direct structure–property relationships that comprise the majority of the compounds is difficult due to the great structural diversity observed in these materials, but in the case of magnetic and thermal properties, some general trends can be suggested. Besides the classical studies on magnetic and thermal properties, recently several research groups have started to test the hybrid vanadates as catalysts and photocatalysts. In this section, the physicochemical properties of HV are described, and in the concrete case of the thermal properties, future trends and scopes are suggested.

4.1. Thermal properties

The thermal properties of HV will be focused on the 3D and 2D crystal structures. Unfortunately, most of the thermal studies carried out on HV consist of thermogravimetric measurements, which only give information about the temperature ranges in which the different decomposition processes (such as loss of crystallization or coordination water molecules or calcination of the organic ligand) occur. There are

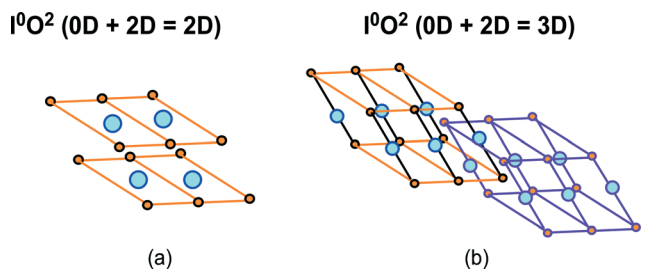

Scheme 15 Structural types in the I^0O^2 group.

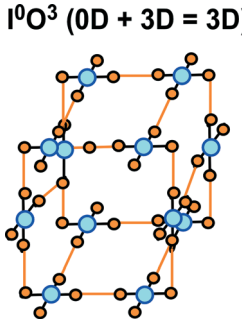

Scheme 16 Structural type in the I^0O^3 group.

few examples in which temperature-dependent X-ray diffractometry studies (thermodiffractometry) have been carried out. These measurements complement the thermogravimetric studies and give a lot of information about the thermal response of the crystal structure to the loss of solvent or coordinated species, or simply, to the increase in temperature (thermal expansion or structural transitions).

The thermal properties of HV will be discussed in two different subsections, concerning the structural response of the crystal frameworks to the loss of coordinated water molecules and to the reversible release of solvent water molecules. Several examples of the thermal response of different 3D and 2D HV will be described.

4.1.1 Thermal response to the loss and uptake of coordinated water molecules. The crystal structures of $[\{Ni_6(H_2O)_{10}(4Bpy)_6\}(V_{18}O_{51})]\cdot 1.5H_2O$ and $[\{Ni(H_2O)_2(Bpe)\}(V_4O_{11})]\cdot 0.5H_2O$ (ref. 46) are classified as $\mathbf{I^3O^1}$ (for more information see Fig. 9, section 2), being the rigid inorganic frameworks stabilized by crossed organic ligands their most relevant characteristic (Fig. 14, section 3.1). The crystallization water molecules are encapsulated between the inorganic scaffold and the organic ligand, and the coordination environment of the metal centres is completed by water molecules. For both compounds, the loss of crystallization water molecules finishes at high temperatures (180 °C). No structural response of the crystal structures to the loss of crystallization water molecules is observed. The removal of coordinated water molecules is a continuous and irreversible process (180–280 °C), which involves a drastic crystallinity reduction and important changes in the IR absorption bands related to the V=O and V–O–V stretching vibration modes.

In this regard, Fig. 25 shows the progressive replacement of the most intense maximum of $[\{Ni(H_2O)_2(Bpe)\}(V_4O_{11})]\cdot 0.5H_2O$ HV (2θ = 8.2°) by the maximum located at 9.0° in 2θ(°), related to the high-temperature anhydrous compound. The evolution of the position for the (020) and (011) reflections indicates a contraction in "*c*" and an increase in the "*b*" parameter.

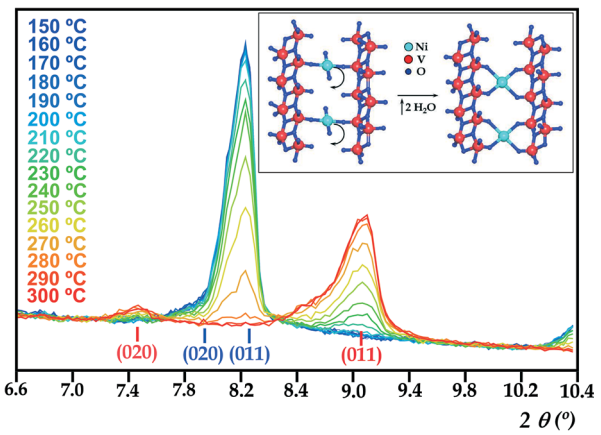

Fig. 25 Displacement of the (020) and (011) reflections during the structural transformation of $[\{Ni(H_2O)_2(Bpe)\}(V_4O_{11})]\cdot 0.5H_2O$. Inset: the qualitative model for the transformation due to the loss of coordinated water molecules. Reproduced from ref. 46 with permission of Wiley-VCH Verlag GmbH and Co. KGaA. Copyright (2009).

Taking into account the changes in the XRD patterns and IR spectra, Fernández de Luis *et al.*[46] proposed a transformation mechanism, involving the generation of two new Ni–O bonds with the V=O terminal oxygen atoms of the VO_5 polyhedra. As shown in Fig. 25 (inset), the equatorial plane of the Ni(II) coordination environment is completed, establishing two new bonds with terminal oxygen atoms belonging to VO_5 polyhedra within the adjacent metavanadate chain.

Another irreversible structural transformation due to the loss of coordinated water molecules is also observed in $\{Ni_2(H_2O)_2(Pz)\}(V_4O_{12})$.[39,40] This HV possesses a $\mathbf{I^2O^1}$ crystal architecture (see Fig. 9, section 2). As it is observed in Fig. 26, the inorganic layers are constructed from two edge-sharing Ni(II) octahedra corner linked to $\{V_4O_{12}\}$ cycles. The inorganic layers are linked through Pz ligands. The coordination environment of the Ni(II) atoms is completed by one coordination water molecule. An important feature that stands out in Fig. 26 is the hydrogen bond established between the coordinated water molecule and the terminal oxygen atom belonging to the V=O terminal groups within the (VO_4) tetrahedra.

The crystal structure of the anhydrous compound could not be solved due to the loss of crystallinity resulting from the removal of the coordinated water molecules. However, according to the X-ray diffractograms, it is very likely that the six coordination environment of the nickel(II) atoms is maintained during the structural transformation through a slight rotation of the nickel dimers along the hydrogen bond and towards the V=O vanadyl groups, which allows the generation of a new Ni–O bond, compensating for the loss of coordinated water molecules. This transformation mechanism is pointed in Fig. 26 with arrows.

This solid state transformation mechanism was confirmed by synchrotron radiation X-ray diffraction in the case of $\{Ni_2(H_2O)_2(Bpa)_2\}(V_6O_{17})$ (Fig. 27). This $\mathbf{I^3O^1}$ HV (see Fig. 9) retains its crystallinity after the loss of coordinated water molecules. Thermodiffractometry studies show a solid state reaction involving a strong structural transformation. The crystal structure of the anhydrous compound could be solved by rigid body refinement of the room temperature model. Fig. 27(a) and (b) depict the transformation mechanism in this compound. The main difference between the hydrated and the anhydrous crystal structures lies in the connectivity between the Ni(II) cations and the VOS. The loss of coordination water molecules from the Ni(II) metal centres is compensated for by the incorporation of the terminal oxygen atoms belonging to the VO_4 tetrahedra into the coordination sphere of the Ni(II) cations (Fig. 27(b)).[59] The structural transformation also involves changes in the cell parameters and the reorientation of the Bpa ligand and the $\{V_4O_{12}\}$ cycles as well as the $\{V_2O_7\}$ dimers that form the vanadate chains (see Fig. 12, section 3.1).

Dynamic structural changes induced by the removal/readsorption of coordinated species from the framework

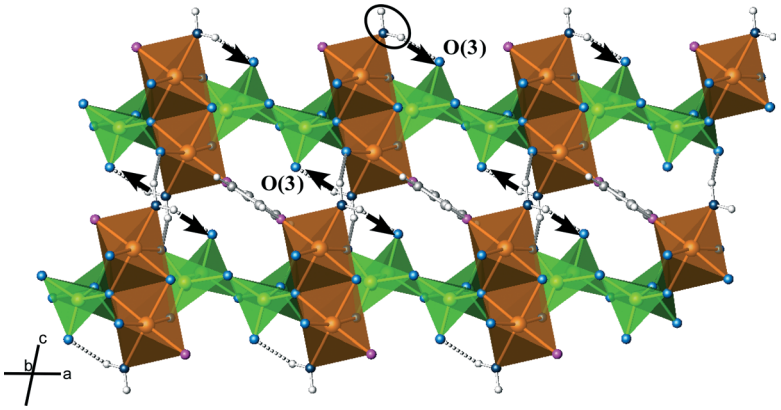

Fig. 26 Structural transformation pathway proposed for the dehydration of $\{Ni_2(H_2O)_2(Pz)\}(V_4O_{12})$. Adapted from ref. 39 with permission of Elsevier. Copyright (2007).

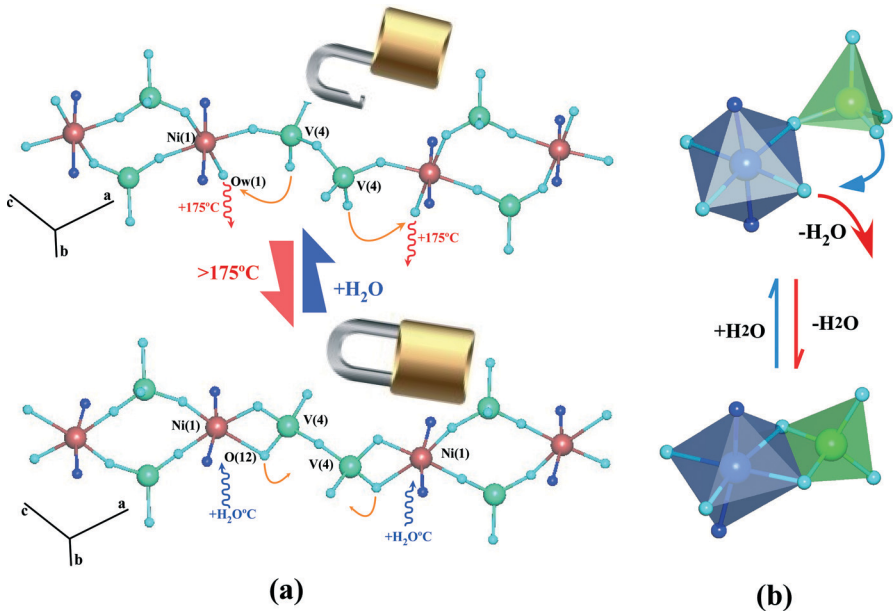

Fig. 27 (a) Structural transformation pathway proposed for the dehydration of $\{Ni_2(H_2O)_2(Bpa)_2\}(V_6O_{17})$. Adapted from ref. 59 with permission of the American Chemical Society. Copyright (2014). (b) Coordination polyhedra involved in the transformation mechanism observed in $\{Ni_2(H_2O)_2(Bpa)_2\}(V_6O_{17})$.

itself are rare, and certain thermal stability after the removal of coordinated water molecules is necessary. In this sense, the $[\{Co_2(Pcca)_2(H_2O)\}(V_4O_{12})_{0.5}]\cdot 3.62H_2O$ $\mathbf{I^1O^2}$ vanadate (see structural description in section 3.3) undergoes two distinct reversible single-crystal-to-single-crystal transformations.

The removal of the guest molecules generates the shrinkage of the framework, while the loss of the coordinated water molecule involves an unusual change in the coordination environment of the cobalt centre, from six (octahedral) to five (bipyramidal). Fig. 28(a) and (b) show the crystal structure of the hydrated and anhydrous compounds, revealing the coordination environment of the Co(II) cations in both crystal structures. Together with this change in the cobalt coordination environment, there is a colour change of the compound from red to brown. Whereas the removal of the guest water molecules leads to a small decrease in volume, it is the removal of the coordinated water molecules that initiates the more substantial channel collapse.

4.1.2 Thermal response to the loss of crystallization water molecules. The effect of the loss of crystallization water molecules on $\mathbf{I^3O^3}$ compounds $[\{Ni_8(4Bpy)_{16}\}(V_{24}O_{68})]\cdot 8.5H_2O$ and $[\{Ni_3(H_2O)_3(Bpa)_4\}(V_6O_{18})]\cdot 8H_2O$ is related to the rigid and flexible natures of the 4Bpy and Bpa organic ligands, respectively. The crystal structures have been previously described in section 3.1 (see Fig. 17).

For $[\{Ni_8(4Bpy)_{16}\}(V_{24}O_{68})]\cdot 8.5H_2O$, despite having a 3D inorganic scaffold and a rigid ligand such as 4Bpy, the crystal structure volume contracts by 0.6% during the loss of crystallization water molecules. Fig. 29(a) shows the thermal evolution of the cell volume obtained from a cyclic Rietveld refinement. The initial contraction is ascribed to the loss of crystallization water molecules.

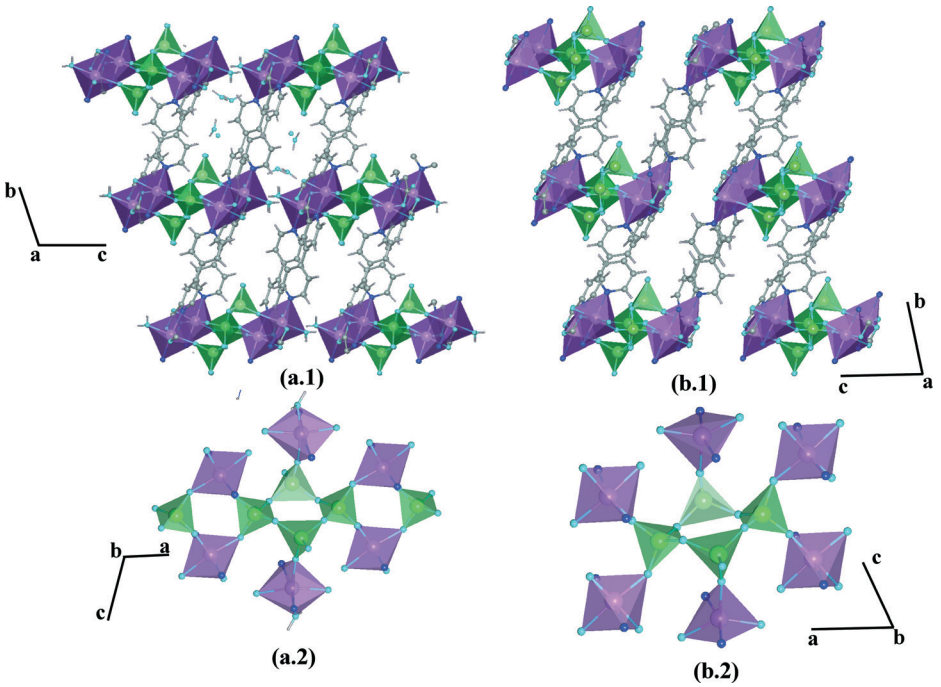

Fig. 28 (a.1 and a.2) Views of the $[\{Co_2(Pcca)_2(H_2O)(V_4O_{12})_{0.5}\}_n]$ framework containing hydrated Co(II) in an octahedral coordination environment. (b.1 and b.2) Views of the dehydrated $[\{Co_2(Pcca)_2(V_4O_{12})_{0.5}\}_n]$ framework containing Co(II) in a trigonal–bipyramidal coordination environment. Reproduced from ref. 81 with permission of Wiley-VCH Verlag GmbH and Co. KGaA. Copyright (2005).

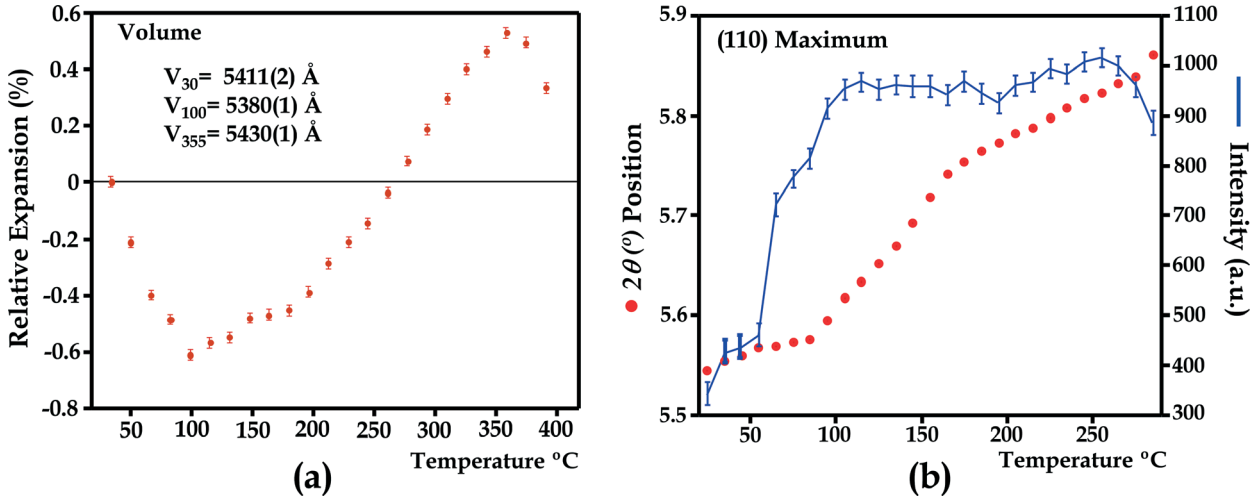

Fig. 29 (a) Thermal evolution of the cell volume for $[\{Ni_8(4Bpy)_{16}\}(V_{24}O_{68})]\cdot 8.5H_2O$. (b) Thermal displacement of the (110) reflection for the $[\{Ni_3(H_2O)_3(Bpa)_4\}(V_6O_{18})]\cdot 8H_2O$ hybrid vanadate. Adapted from ref. 47 and 58 with permission of The Royal Society of Chemistry, Copyright (2010), and the American Chemical Society, Copyright (2012).

The I^3O^3 $[\{Ni_3(H_2O)_3(Bpa)_4\}(V_6O_{18})]\cdot 8H_2O$ framework possesses a more dynamic structural response to the loss of solvent, probably due to the presence of the more flexible Bpa organic ligand in the crystal structure. The thermal evolution of the $2\theta(°)$ position and intensity for the (110) reflection is shown in Fig. 29(b). The intensity variation suggests the existence of three different processes, the first one between 25 °C and 80 °C, the second one in the 80 °C to 200 °C range, and the third one above 200 °C.

The removal of eight crystallization water molecules per formula unit takes place between room temperature and 80 °C and involves the contraction of the [100] channels in which the guest is located. After the loss of crystallization water molecules and in the second temperature range, between 80 and 200 °C, the crystal structure continues its contraction, showing a negative thermal expansion. In the third step (200–275 °C), the loss of coordinated water molecules takes place, generating an irreversible and strong structural transformation, which promotes a reduction in the crystal domains, lowering the crystallinity of the compound (Fig. 29(b)). The main difference between the thermal response of $[\{Ni_8(4Bpy)_{16}\}(V_{24}O_{68})]\cdot 8.5H_2O$ and

$[\{Ni_3(H_2O)_3(Bpa)_4\}(V_6O_{18})]\cdot 8H_2O$ compounds to the loss of solvent is the range of cell volume contraction. Both compounds exhibit a reversible and dynamical structural response, however while the crystal framework of $[\{Ni_8(4Bpy)_{16}\}(V_{24}O_{68})]\cdot 8.5H_2O$ responds with a cell volume reduction of 0.6%, the $[\{Ni_3(H_2O)_3(Bpa)_4\}(V_6O_{18})]\cdot 8H_2O$ compound exhibits a contraction of approximately 6%. Both compounds possess complex 3D structures, combining both 3D inorganic and metal–organic substructures; however, the flexibility of the Bpa ligand is larger than that of the 4Bpy ligand. While the pyridyl rings of the Bpa organic molecules could rotate and orient itself through the ethane group, leading to a reduction in the distance between the nitrogen donor atoms, the 4Bpy ligand acts as a rigid pillar.

Amazing examples of the dynamic and reversible response of the crystal structures due to the loss of guest water molecules are those of the manganese HV $[\{Mn(4Bpy)\}(VO_3)_2]\cdot 1.16H_2O$ and $[\{Mn(4Bpy)\}_{0.5}(VO_3)_2]\cdot 0.62H_2O$.[51]

As it has been described previously, these I^2O^2 crystal architectures are constructed from inorganic layers pillared by the 4Bpy organic ligand (see section 3.2). The crystallization water molecules are located between the organic pillars and the inorganic layers. The crystal structures of both compounds before and after the loss of crystallization water molecules are shown in Fig. 30. The changes in the unit cell parameters and angles are represented in the same figure. The response of the different structural subunits during the transformation is also indicated by arrows.

For both compounds, two important displacements and intensity changes of some X-ray diffraction reflections take place during the heating process near room temperature. The loss of solvent leads to the tilting of 4Bpy pillars between the inorganic layers, and hence an increase in the "β" angle value. However, surprisingly, the major structural changes are directly associated with the compression of the inorganic layers, which generates the reduction of the "a" parameter. In this way, the opposite tilt of the vanadate and manganese octahedral chains explains, qualitatively, the variation in the unit cell parameters for both compounds due to the removal of the solvent (Fig. 30).

It is difficult to establish general temperature ranges for the loss of crystallization and coordinated water molecules, because these processes strongly depend on the crystal

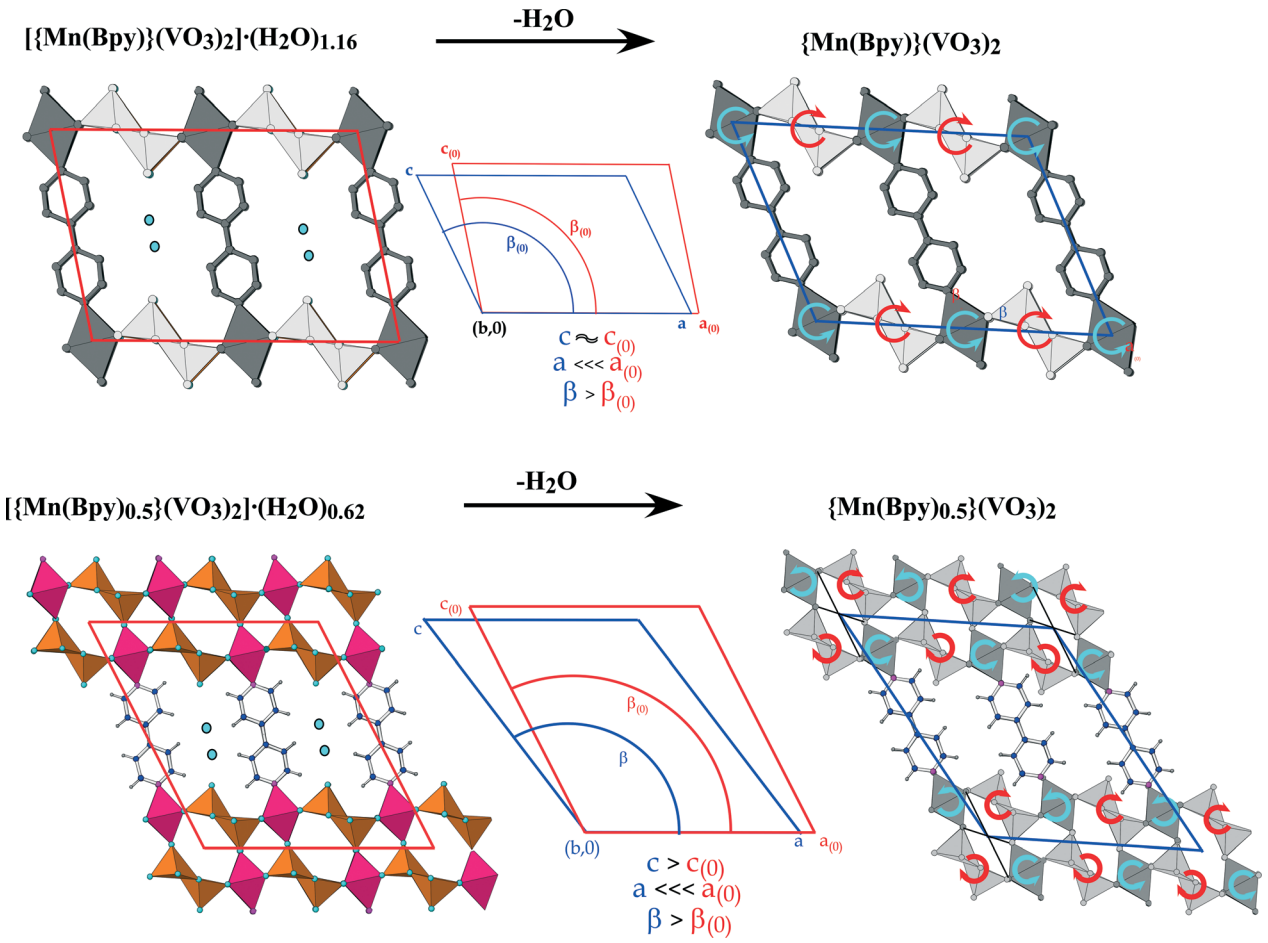

Fig. 30 Qualitative description of the crystal response to the loss of crystallization water molecules in $[\{Mn(4Bpy)\}(VO_3)_2]\cdot 1.16H_2O$ (top) and $[\{Mn(4Bpy)\}_{0.5}(VO_3)_2]\cdot 0.62H_2O$ (bottom). Reprinted from ref. 51 with permission of the American Chemical Society. Copyright (2010).

structure itself. In the same way, it is also difficult to predict the crystal structure response to the loss of crystallization and/or coordinated water molecules. From a general point of view, these vanadates containing rigid organic linkers and compact inorganic frameworks, such as $[\{Ni_6(H_2O)_{10}(4Bpy)_6\}(V_{18}O_{51})]\cdot 1.5H_2O$ and $[\{Ni(H_2O)_2(Bpe)\}(V_4O_{11})]\cdot 0.5H_2O$, do not show strong structural responses to the loss of guest molecules, but the crystal structures are not able to accommodate the removal of coordination water molecules, leading to an irreversible amorphization of the compounds.

In the case of HV containing less rigid inorganic frameworks and organic linkers, such as $[\{Ni_3(H_2O)_3(Bpa)_4\}(V_6O_{18})]\cdot 8H_2O$, the loss of crystallization water molecules induces a dynamic response of the crystal structures, and the removal of coordinated water molecules is reversible, even when the process gives rise to amorphous or poor crystalline compounds. In these processes involving the removal and uptake of species that form an integral part of the crystal framework, the crystal structure adaptability is a key point to obtain crystalline compounds after the transformations. In fact, the $\{Ni_2(H_2O)_2(Bpa)_2\}(V_6O_{17})$ and $[\{Co_2(Pcca)_2(H_2O)\}(V_4O_{12})_{0.5}]\cdot 3.62H_2O$ crystal structures are examples of this. The rational design of the crystal structures and more specifically the rational choice of initial structural building blocks with enough degree of freedom to establish new weak interactions and/or bonds are essential tasks to avoid crystalline to pseudoamorphous transformations after the loss of coordinated species. Different possible strategies can be adopted, such as: (i) the synthesis of crystal structures containing non-rigid inorganic substructures formed by corner-sharing polyhedra (for more information about the hydrothermal synthesis of HV, the reader is referred to the studies by Fernández de Luis *et al.*,[59,89] Livaje *et al.*[90] and Chirayil *et al.*);[91] (ii) the choice of secondary metal centres that could adopt different coordination environments, such as Co(II) and Cu(II); and (iii) the use of flexible organic ligands that not only could adopt different conformations, but also do not incorporate extra donor atoms that could complete the coordination sphere of the secondary metal centres.

4.2. Magnetic properties

4.2.1 Hybrid vanadates with diamagnetic V(v) vanadium oxide subunits. The connectivity of the metal centres in HV usually takes place through VO_4 tetrahedra and organic linkers, thus the length of the M–O–V–O–M magnetic exchange pathways and the length and electronic structure of the organic ligands play a crucial role in the magnetic coupling of the metal centres. Even for those species showing polymerization, the connectivity of the polymerized units occurs *via* vanadate bridges and/or organic ligands. This has an obvious consequence in the magnetic behaviour of those systems, in such a way that the strength of the magnetic exchange along these pathways is inevitably reduced compared with that in a M–O–M link.

Several HV are constructed from magnetically isolated atoms showing a typical paramagnetic behaviour. Common magnetic structural building blocks are the dimeric units constructed from metal octahedra sharing an edge. Examples of these are the $\mathbf{I^2O^1}$ $\{Ni_2(H_2O)_2(Pz)\}(V_4O_{12})$ and $\mathbf{I^2O^2}$ $\{Ni(Bpe)\}(VO_3)_2$ crystal structures that contain inorganic layers interconnected by metal–ligand chains (see Fig. 26 and 19 and sections 4.1 and 3.1 for more information about the crystal structures).[39,53] The Ni(II) octahedra share one edge, giving rise to dimeric units in both crystal structures. However, the distance and number of atoms between adjacent dimeric units are large enough to avoid any interdimer magnetic interaction. The magnetic susceptibilities are well fitted to typical intradimer antiferromagnetic (AF) interactions with J/k values of −22.4 and −59.4 K for $\{Ni_2(H_2O)_2(Pz)\}(V_4O_{12})$ and $\{Ni(Bpe)\}(VO_3)_2$, respectively. The magneto-structural correlations in dimeric complexes show that the J exchange parameter is directly connected with the Ni–O–Ni bridging angle with a crossover value of 97° between the ferromagnetic (F) and the AF behaviour.[92] The Ni–O–Ni angle for $\{Ni_2(H_2O)_2(Pz)\}(V_4O_{12})$ (95.95°) and $\{Ni(Bpe)\}(VO_3)_2$ (92.80°) may favour the F interaction between metal centres, but the out-of-plane Ni–O–V angles and the connectivity between the metal centres and the vanadium atoms have a great influence on the final magnetic behaviour, as observed in the susceptibility measurements.[93,94]

Dimeric units of Co(II) centres linked by VO_4 tetrahedra have been reported for $\{Co(4Bpy)\}(VO_3)_2$ and $\{Co(Bpa)\}(VO_3)_2$.[57] As it has been previously described (see Fig. 18, section 3.2), the $\mathbf{I^2O^1}$ $\{Co(4Bpy)\}(VO_3)_2$ and $\{Co(Bpa)\}(VO_3)_2$ HV contain inorganic $\{CoV_2O_6\}$ layers interconnected by Co(4Bpy) and Co(Bpa) chains. The magnetic exchange across the organic ligand is expected to be very weak, thus the overall AF interaction should be mainly attributed to the superexchange coupling within the inorganic layers (see Fig. 18). The Co(II)···Co(II) distances within the layers suggest that the effective magnetic coupling is given between Co(II) atoms linked through one (VO_4) tetrahedron, generating magnetic dimeric AF units. The adjacent dimeric units are far enough to avoid significant interdimer magnetic coupling (see Fig. 18(b)). The thermal evolution of the magnetic susceptibilities for $\{Co(4Bpy)\}(VO_3)_2$ (ref. 37) and $\{Co(Bpa)\}(VO_3)_2$ (ref. 57) show broad maxima located at 36 and 20 K, respectively. The susceptibility curves can be explained based on dimeric AF interactions plus the spin–orbit coupling typical for Co(II) d^7 cations.

The metal centres can also be magnetically coupled through the VOS or the organic ligand, giving rise to one-dimensional systems, such as in $[\{Ni(H_2O)_2(Bpe)\}(V_4O_{11})]\cdot 0.5H_2O$ and $\{Co_2(2\text{-}Pzc)(H_2O)\}(VO_3)_3$ compounds.[37,46] For $[\{Ni(H_2O)_2(Bpe)\}(V_4O_{11})]\cdot 0.5H_2O$, the magnetic susceptibility continuously increases in value in the 300 to 2 K temperature range. Fig. 31 shows the thermal evolution of χ_m and $\chi_m T$. The VO_5 polyhedra and $Ni(H_2O)_2N_2O_2$ octahedra are corner-sharing, giving rise to 1D chains, with the shortest Ni(II)···Ni(II) distance of 6.26 Å. The inset of Fig. 31 shows

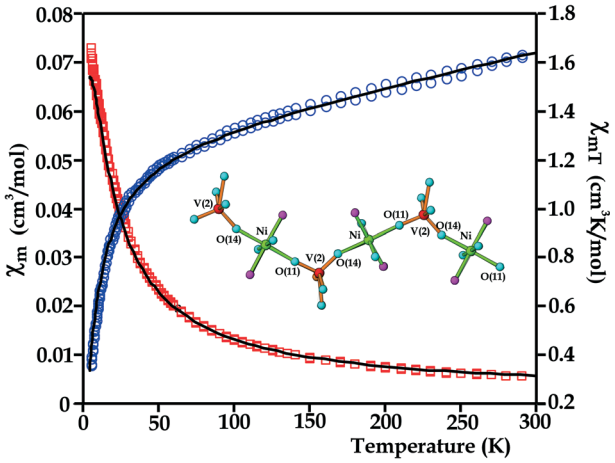

Fig. 31 χ_m and $\chi_m T$ curves of $[\{Ni(H_2O)_2(Bpe)\}(V_4O_{11})]\cdot 0.5H_2O$. The lines are the best fit for a Heisenberg isotropic AF $S = 1$ chain model. Inset: One-dimensional magnetic exchange pathway between Ni(II) cations through the VO_5 polyhedra. Reproduced from ref. 46 with permission of Wiley-VCH Verlag GmbH and Co. KGaA. Copyright (2009).

the connectivity between the Ni(II) metal centres through VO_5 polyhedra. The magnetic susceptibility was analysed with Heisenberg isotropic AF $S = 1$ chain model. The fitting is shown in Fig. 31. The best fit yields $g = 2.27$ and $J = -5.83$ K, corroborating the existence of a weak AF interaction between the metal centres through the vanadate subunit.

The $\{Co_2(2\text{-Pzc})(H_2O)\}(VO_3)_3$ $\mathbf{I^3O^1}$ structure (see section 3.1 for more information about the crystal structure) is composed of infinite $\{Co_2(2\text{-Pzc})(H_2O)\}$ metal–organic chains isolated by diamagnetic metavanadate chains. The $\{Co_2(2\text{-Pzc})(H_2O)\}$ paramagnetic chains contains corner-sharing dimers of cobalt octahedra. Magnetic data were analysed by an isotropic dimer model for $S = 3/2$ ions with the inclusion of interdimer interaction (θ). The magnetic exchange coupling is mainly attributed to the intradimer AF exchange of Co(II) metal centres through the Co–O–Co bridges ($g = 2.52$, $J = -14.8$ cm^{-1}). The weak interdimer interaction through the pyrazine group ($\theta = -0.9$ K) is in good agreement with the other pyrazine bridged compounds where only very weak AF interactions occur between the magnetic centres.

An interesting example of magnetically isolated $\{Cu(Pz)_2\}$ metal–organic layer between diamagnetic $\{V_6O_{16}\}^{2-}$ layers is the $[\{Cu(Pz)_2\}(V_6O_{16})]\cdot 0.22H_2O$ $\mathbf{I^3O^2}$ vanadate. The $\{Cu(Pz)_2\}$ layers exhibit AF ordering of the square lattice of Cu(II) ions, with χ_{max} at 8 K.[41]

Magnetic trimers of edge-sharing Cu(II) cations have been reported for $\{Cu_3(1,2,3\text{-Trz})_2\}(V_4O_{12})$ $\mathbf{I^2O^1}$ and $\{Cu_3(1,2,4\text{-Trz})_2\}(V_4O_{12})$ $\mathbf{I^3O^2}$ (see section 3.1, Fig. 16) HV.[73,75] For $\{Cu_3(1,2,3\text{-Trz})_2\}(V_4O_{12})$, χ_m shows a continuous increase with a maximum at 12 K, then decreases until 2 K, while the $\chi_m T$ product decreases continuously with temperature. The χ_m and $\chi_m T$ evolution suggest AF interactions between the Cu(II) metal centres. The magnetic data were first fitted to a relatively isolated trimeric linear units of Heisenberg $S = 1/2$ (S_{A1}-S_B-S_{A2}) model with one nearest interaction J and two different values of the g factor. Fig. 32(a) and (b) show the

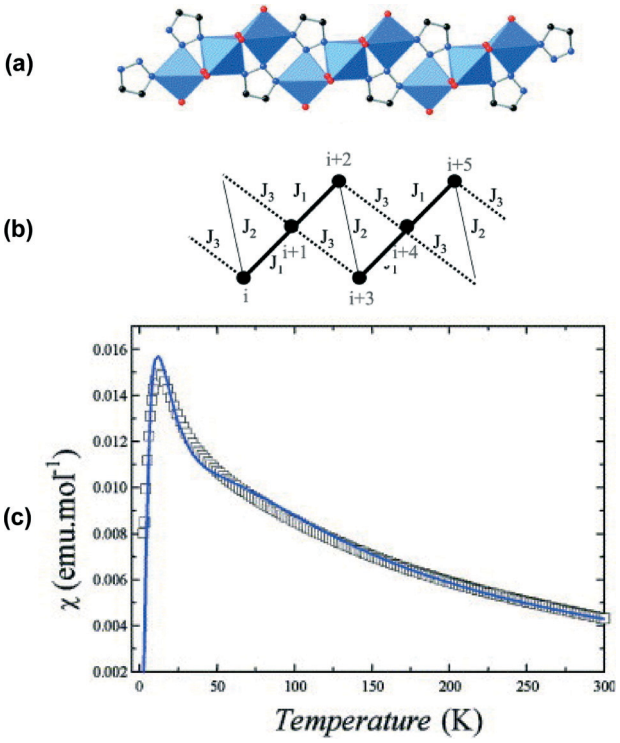

Fig. 32 (a) View of a $\{Cu_3(1,2,4\text{-Trz})_2\}_n^{4n+}$ chain of $\{Cu_3(1,2,4\text{-Trz})_2\}(V_4O_{12})$ showing the bridging of Cu(II) trinuclear units by the triazolate ligands. (b) Magnetic model of a chain of trimers with two intertrimer exchange pathways (J_2 and J_3). (c) Plot of susceptibility *vs.* T with the blue line showing the fit to the trimer chain model. Adapted from ref. 75 with permission of The Royal Society of Chemistry.

trimeric units linked through the trizolate organic ligand and the magnetic exchange pathways within the Cu(II) cations in the trimeric units. The fitting of the thermal evolution of the magnetic susceptibility and the thermal evolution of the magnetic susceptibility are shown in Fig. 32(c). The best fit was obtained for $g_A = 2.44$, $g_B = 2.27$, $J = -66$ K and $\theta = -26$ K. The high value of the interdimer magnetic exchange (θ) indicates strong interactions between trimers.

Devi *et al.*[73] described the magnetic behaviour based on a chain of trimers with two intertrimer exchange pathways (J_2 and J_3) (Fig. 32(b)). The best fitting values are $g = 2.3$, $J_1 = -98$, $J_2 = -37$, $J_3 = -16$ K, $\theta = -6.6$ K, and TIP (temperature-independent magnetism) $= 2 \times 10^{-5}$ emu mol^{-1}. If the crystal structure is taken into account, intertrimer magnetic exchange can be mainly attributed to the magnetic exchange through the triazolate bridges between trimers. The linkage of $\{Cu_3(1,2,3\text{-Trz})_2\}$ metal–organic chains through the $\{V_4O_{12}\}$ cycles involves a very long exchange pathway (Cu–O–V–O–V–O–Cu), thus the magnetic interactions are not expected to be very strong. For $\{Cu_3(1,2,4\text{-Trz})_2\}(V_4O_{12})$, a similar shape of the χ_m curve is observed, which is in good agreement with the existence of AF coupled trimetric units in the crystal structure. In comparison with the previously described copper vanadate, the Cu(II) cations within the trimetric units are linked through the triazolate and VO_4 bridges. Each

trimetric unit connects to other four *via* triazolate ligands, giving rise to two-dimensional $\{Cu_2(1,2,4\text{-}Trz)_3\}$ ruffled layers with an amplitude of about 4.75 Å and a period of 8.87 Å. (see Fig. 16, section 3.1) In the same way as that for $\{Cu_3(1,2,3\text{-}Trz)_2\}(V_4O_{12})$, attempts to fit the data for non-interacting trimetric units were unsuccessful, suggesting strong intertrimer magnetic coupling. Moreover, the susceptibility exhibits a sharp drop below 6 K and FC–ZFC divergence, suggesting long-range AF ordering.

The comparative study of the magnetic properties of $[Co(H_2O)_2(VO_3)_2]\cdot 2H_2O$ and the $\{Co(Pym)\}(VO_3)_2$ I^3O^1 HV reveals the importance of including the M–L–M magnetic exchange pathway in competition with the magnetic coupling established by the metal centres in the purely inorganic framework.[43] The inorganic scaffolds of both compounds are very similar and contain cobalt metal centres connected though double metavanadate chains giving rise a 3D scaffold. Fig. 33(a) shows a comparative view of the crystal structures of $\{Co(Pym)\}(VO_3)_2$ and $[Co(H_2O)_2(VO_3)_2]\cdot 2H_2O$. In the hybrid compound, the metal centres are connected through the pyrimidine organic ligand, giving rise to metal–organic chains aligned in the [100] crystallographic direction. The possible magnetic exchange pathways between Co(II) cations are represented in Fig. 33(b). There are two common magnetic exchange pathways across the metavanadate chains for both crystal structures, defined as J_1 and J_2. For the hybrid compound, a third magnetic pathway through the organic ligand takes place (J_3).

Fig. 34(a) and (b) show the thermal evolution of χ_m and $\chi_m T$ measured at a magnetic field of 1 kOe for $\{Co(Pym)\}(VO_3)_2$ and $[Co(H_2O)_2(VO_3)_2]\cdot 2H_2O$, respectively. For the inorganic compound, the negative value of the Weiss temperature $\theta = -33.7$ K and the decrease in the $\chi_m T$ product indicate the AF coupling of the Co(II) octahedra through the double metavanadate chains. The thermal dependence of the magnetic susceptibility χ_m for the inorganic compound shows a maximum at 2.5 K, indicating the existence of 3D AF ordering (Fig. 34(b)). The small change in the curvature in the magnetization curve registered at a critical field H_c of 6 kOe is also in good agreement with the establishment of 3D AF ordering at low temperatures. The λ peak observed in the magnetic specific heat measurements at low temperatures and its shift to lower temperatures by increasing the magnetic field confirm the AF ordering. At magnetic fields higher than 30 kOe, the maximum shifts to higher temperatures, indicating F ordering. The broad maximum could be related to an F component in the inorganic scaffold.

The $\{Co(Pym)\}(VO_3)_2$ hybrid vanadate possesses the same connectivity and structural units as those of $[Co(H_2O)_2(VO_3)_2]\cdot 2H_2O$ in the inorganic scaffold, except for the pyrimidine ligand. The linkage of the Co(II) metal centres through the pyrimidine bridges introduces a competition between the AF coupling of the Co(II) cations of the inorganic scaffold and the magnetic exchange through the organic ligand, as it is suggested by the irreversibility of the magnetic susceptibility at low temperatures which indicates the

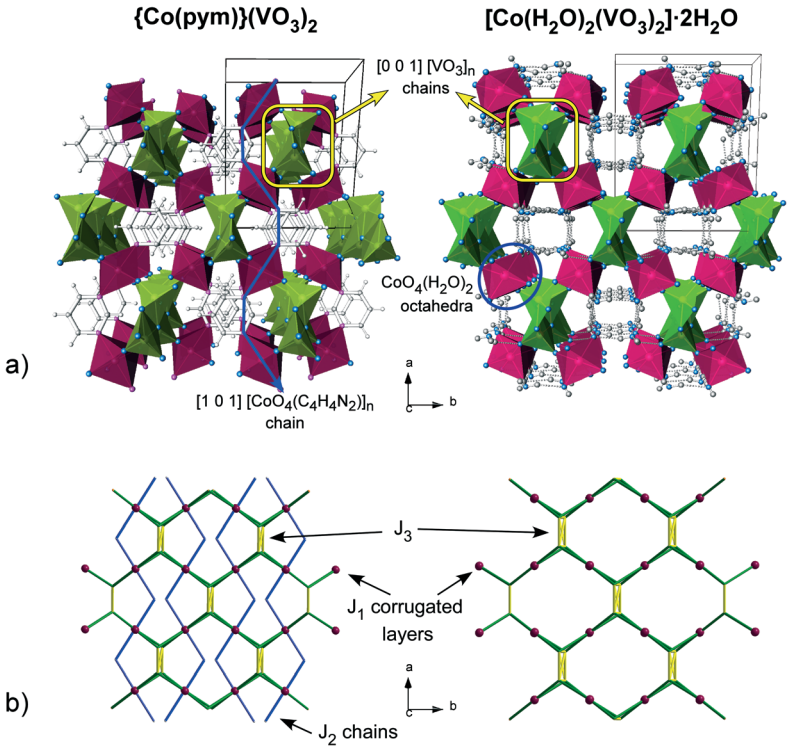

Fig. 33 (a) Polyhedral view of the three-dimensional crystal structures of $\{Co(Pym)\}(VO_3)_2$ and $[Co(H_2O)_2(VO_3)_2]\cdot 2H_2O$ in the *ab*-plane (maroon polyhedra: CoN_2O_4 octahedra; green polyhedra: metavanadate chains). (b) Schematic representation of the magnetic exchange pathways in 1 and 2. Reproduced from ref. 43 with permission of The Royal Society of Chemistry.

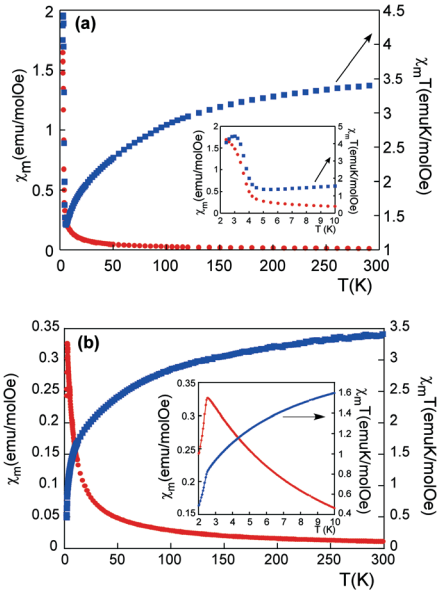

Fig. 34 Thermal evolution of χ_m and $\chi_m T$ measured at a magnetic field of 1 kOe for {Co(Pym)}$(VO_3)_2$ (a) and $[Co(H_2O)_2(VO_3)_2]\cdot 2H_2O$ (b). The insets show the low temperature region. Reproduced from ref. 43 with permission of The Royal Society of Chemistry.

existence of a weak F component. The decrease in the $\chi_m T$ product and the negative value of the Weiss temperature $\theta = -34.5$ K indicate the existence of AF interactions in the high temperature range (Fig. 34(a)). The magnetization measurements carried out at 2 K show a hysteresis loop with a coercive field value of 330 Oe and a remnant magnetization of 1604 emu mol^{-1}. The hysteresis decreases with increasing temperature, disappearing at 4.5 K. The general shape of the $M(H)$ curve, with hysteresis at low fields, and the AF behaviour at higher fields are characteristics of soft ferromagnets.

The F contribution at low temperatures is favoured by the Co–pym–Co bridges, which compete with the AF coupling of the inorganic scaffold. The increase in the applied field or the temperature favours the AF ordering of the inorganic scaffold, which is in good agreement with the AF ordering observed in the inorganic compound, revoking the F component associated with the Co–pym–Co metal–organic chains.

Other very interesting examples of the introduction of organic molecules in inorganic scaffolds are the $[\{Mn(4Bpy)\}(VO_3)_2]\cdot 1.16H_2O$ and $[\{Mn(4Bpy)\}_{0.5}(VO_3)_2]\cdot 0.62H_2O$ $\mathbf{I^2O^2}$ hybrid Brannerites (hereafter denoted as MnBpy and $MnBpy_{0.5}$), closely related in structure to the inorganic MnV_2O_6 vanadate.[51] In all of the crystal structures, the Mn(II) octahedra are edge-sharing, giving rise to chains extended along the "*b*" axis. It is well known that, in the different Brannerite inorganic compounds reported, the metal cations are F coupled within the chains and AF ordering of the adjacent chains is achieved at low temperatures. In the hybrid MnBpy and $MnBpy_{0.5}$ Brannerites, the vanadate and manganese chains are connected, giving rise to inorganic layers. These are pillared by the organic ligand (see Fig. 30). In this respect, the interchain distances, from 4.964 Å in MnV_2O_6 to 5.471 Å in $MnBpy_{0.5}$ and 8.537 Å in MnBpy, are related to the Néel temperature, from 20 K in MnV_2O_6 to 7.5 and 4 K in $MnBpy_{0.5}$ and MnBpy, respectively.

The maxima observed at 7.5 and 4 K in the χ_m and $\chi_m T$ curves also indicate the establishment of 3D AF at low temperatures. The data above the maxima are well fitted to the Curie–Weiss law and also to a one-dimensional homogeneous $S = 5/2$ chain ($H = -JS_i + S_{i+1}$) with positive Weiss temperatures of 16.9 K for MnBpy and 16.3 K for $MnBpy_{0.5}$ and magnetic coupling of $J = 1.142(4)$ and $J = 1.516(7)$ K for MnBpy and $MnBpy_{0.5}$, respectively. These fittings are in good agreement with the F coupling of Mn(II) cations within the chains. The AF ordering is overcome at applied fields as low as 0.2 T for MnBpy and 0.4 T for $MnBpy_{0.5}$. In this sense, the specific heat measurements show λ type peaks at low temperatures, shifted to lower temperatures when higher fields are applied, in good agreement with AF ordering. The AF structure for MnBpy was determined by neutron diffraction, showing the AF ordering of F chains. Fig. 35(a) and (b) show the orientation of the manganese spins in the magnetic cell and in the crystal structure of MnBpy, respectively.

The ability of vanadium atoms to adopt different oxidation states takes an important role in the magnetic properties of HV. {M(Bpy)}(V_4O_{10}) (M = Ag(I), Cu(I)) $\mathbf{I^3O^1}$ compounds present $(V_4O_{10})^-$ reduced layers constructed from corner- and edge-sharing VO_5 distorted square base pyramids.[49] The layers can also be described as zigzag chains of edge-shared VO_5 square base pyramids corner-linked to the adjacent chains (see Fig. 20 section 3.2). In both crystal structures, the vanadium positions V(1) and V(2) belonging to the same zigzag chain have their oxidation states slightly reduced to +4.5, while vanadium atoms V(3) and V(4) exhibit higher valences of +5. Thus, the chains of partially reduced VO_5 polyhedra are structurally isolated from each other. The electric conductivity of both compounds exhibit positive temperature dependence that is consistent with semiconducting behaviour. The nonlinear relationship of $\log(\rho)$ *vs.* $1/T$ indicates that the thermally activated hopping is not characterized by a constant

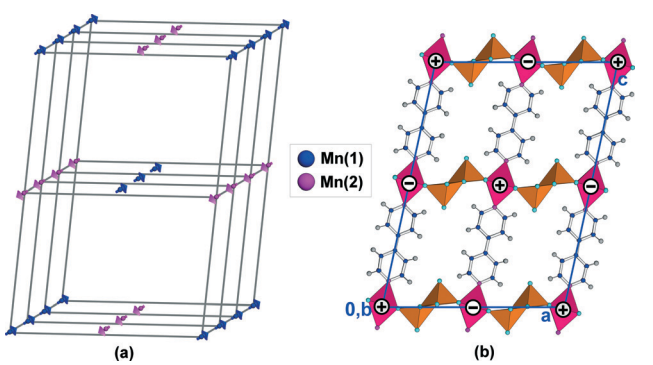

Fig. 35 (a) Magnetic ordering in $[\{Mn(4Bpy)\}(VO_3)_2]\cdot 1.16H_2O$. (b) Magnetic structure of $[\{Mn(4Bpy)\}(VO_3)_2]\cdot 1.16H_2O$. Reprinted from ref. 51 with permission of the American Chemical Society. Copyright (2010).

activation energy. The modelling of the electrical conductivity to the Mott variable-range hopping model indicates that the energetically favourable electron hopping also occurs between more remote V sites rather than solely nearest-neighbour V cations. The magnetic susceptibilities show strong temperature dependences consistent with random localization of unpaired electrons. The Curie–Weiss fits indicate negative Weiss temperatures of $\theta = -25$ and $\theta = -31$ K for Cu(I) and Ag(I) compounds, respectively. The Curie constants are close to that expected for one unpaired spin per formula ($C = 0.374$ emu K mol^{-1}). The magnetic data were also fitted to a Heisenberg linear AF chain model for V^{4+} ($S = 1/2$) with final values of $g = 1.81(2)$ and $J = -6.8(2)$ cm^{-1} for the Cu(I) compound and $g = 1.90(1)$ and $J = 9.01(8)$ cm^{-1} for the Ag(I) vanadate. These results suggest a gradual localization of the electrons along isolated vertex-shared chains of VO_5 pyramids at the lowest temperature.

Another interesting strategy is to combine magnetically active transition metal cations with reduced vanadate groups in the same crystal structure, giving rise to the competition between the magnetic properties related to the randomly or fully delocalized electrons of the reduced VOS and the unpaired electrons of the transition metal centres. Example of this are the reduced hybrid layered $\{M(pz)\}(V_4O_{10})$ (M = Zn(II), Co(II), Ni(II)) vanadates.[38] The crystal structure of these compounds can be envisioned as arising from the *in situ* intercalation and polymerization of cationic $\{M(pz)\}^{2+}$ chains between the $(V_4O_{10})^{-2}$ layers. Due to the mixed valence V^{4+}/V^{5+} of the $(V_4O_{10})^{-2}$ layers, the compounds exhibit electrical conductivity, with apparent activation energy values of 0.36, 0.46 and 0.59 eV for Co, Ni and Zn(II) vanadates, respectively. The average vanadium oxidation state is +4.5 and implies two unpaired electron per $(V_4O_{10})^{-2}$ unit. The observed Curie–Weiss constant for the Zn(II) vanadate (0.79(2) emu K mol^{-1}) is consistent with two randomly localized $S = 1/2$ spins per $(V_4O_{10})^{-2}$ unit. The magnetic susceptibility curve shows a maximum located at 22 K that provides unequivocal evidence of the presence of a single ground state and the formation of a spin gap at low temperatures. The V^{4+}/V^{5+} charge ordering seems to play an important role in the long range order AF transition of the Zn(II) hybrid reduced vanadate. The spin dimer analysis method within the extended Hückel approximation was employed to determine the possible spin lattices for the $(V_4O_{10})^{-2}$ layers and the AF spin–exchange interaction. The interaction energies suggest the possibility of the coexistence of both F and AF exchange within a triangular spin arrangement. The charge ordering to low temperatures could lead to magnetic structures showing both AF and F spin interactions or only AF order intra- and intermagnetic dimers. Fig. 36 shows the temperature dependence of magnetic susceptibility for $\{Zn(pz)\}(V_4O_{10})$. As the Zn(II) cation is diamagnetic, the AF coupling observed in the thermal susceptibility evolution is ascribed to the presence of V^{4+} cations in the crystal structure. The inset of Fig. 36 shows the possible arrangement of the V^{4+} cations within the $(V_4O_{10})^{2-}$ layers.

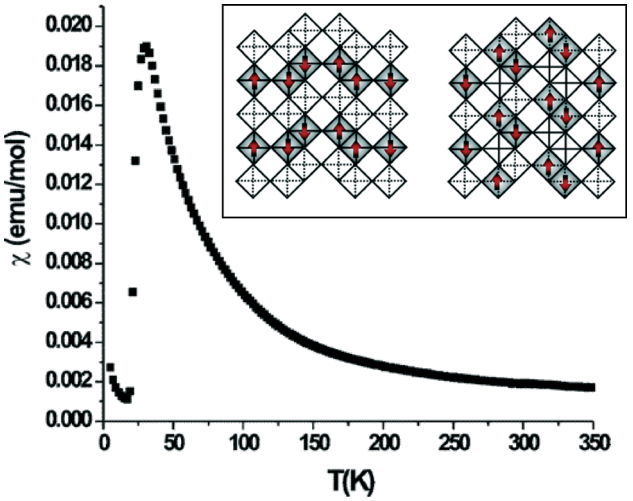

Fig. 36 Plot of magnetic susceptibility *versus* temperature for $\{Zn(pz)\}(V_4O_{10})$. The measuring field was 0.1 T. Inset: two possible spin lattices for the charge localization of V^{4+} sites (shaded) exhibiting both F and AF or only AF V^{4+}–V^{4+} interactions. Adapted from ref. 38 with permission of the American Chemical Society. Copyright (2013).

In the specific case of $\{Ni(pz)\}(V_4O_{10})$ and $\{Co(pz)\}(V_4O_{10})$, the χ_m values obtained for Ni(II) (1.72(3) emu K mol^{-1}) and Co(II) (4.302(4) emu K mol^{-1}) compounds take also into account the temperature-independent paramagnetism of the Ni(II) cation and the spin–orbit coupling effect of the Co(II) metal centres. The magnetic susceptibility curves for the Ni(II) and Co(II) compounds show no sharp peak at low temperatures, suggesting that there is no long range AF ordering, destroying the spin gap state. The ZFC/FC divergences below 10 K may indicate a spin glass ground state for both compounds.

Most of the HV constructed from dipodal ligands present magnetically isolated transition metal cations. The distance between the metal centres connected through the vanadate oxoanion and/or organic ligand is too long, hindering the magnetic coupling between the cations and giving rise to paramagnetic behaviours. However, when the distance between metal centres is short enough and the magnetic superexchange pathway does not involve many atoms, the magnetic interaction through the vanadate groups could lead to dimeric, one-dimensional coupling, and even three-dimensional long range AF ordering. Another strategy is to bridge the metal centres through short organic linkers that favours the magnetic coupling. In several HV, the magnetic metal–organic units are isolated by the vanadate groups, giving rise to cluster or one-dimensional magnetic coupling similar to that showed by purely metal–organic or coordination compounds. But the competition between the magnetic superexchange pathways within the metal–organic scaffolds and the inorganic framework could give rise to metamagnetic compounds. In these, the increase in the magnetic field favours the coupling of the metal centres through the vanadate groups instead of across the ligand, or *vice versa*, leading to field-induced magnetic transitions.

4.3 Catalytic and photocatalytic properties

It is well known that vanadium-based materials are active heterogeneous catalysts for several reactions. In fact, since the discovery of vanadate-dependent enzymes from various algae and terrestrial fungi, the coordination chemistry of this element has received increasing interest.[95] Moreover, recently several studies have revealed that HV could act as a visible light catalyst for water splitting or degradation of pollutants.[96]

Despite several examples in this section being focused on HV with chelating ligands, we consider that this is a very interesting starting point for future research on catalytic and photocatalytic studies on HV constructed from organic connectors.

As far as we are aware, the first catalytic test on HV was done with the family of $M(HAep)_2(VO_3)_4$ (M = Co(II), Ni(II), Cu(II), Aep = 1-(2-aminoethyl)piperazine) compounds. These isostructural $\mathbf{I^2O^0}$ materials possess a 2D crystal structure, constructed from inorganic layers based on metavanadate chains of VO_4 tetrahedra linked through metal centres. The coordination environment of the metal centres is completed by the chelating HAep ligand. The layers of the crystal structure are stacked, establishing hydrogen bonds with the adjacent layers along the [010] crystallographic direction.[97]

The activity of this HV was probed towards oxidation of sulfides. Various catalytic assays were performed with different oxidizing agents (H_2O_2 and TBHP) and substrates (methyl phenyl sulfide, ethyl butyl phenyl sulfide, *p*-chlorophenyl methyl sulfide and methyl *p*-tolyl sulphide).

Fig. 37 shows the kinetic profile of the studied catalysts for the oxidation of methyl phenyl sulfide with H_2O_2 as the oxidizing agent. The behaviour of all of the catalysts is very similar, reaching conversions between 83 and 64%, with selectivity rates towards the sulfoxide over 94%.

The second example of catalytic activity in HV was reported for the $[\{CoNi(H_2O)_2(Bpe)_2\}(V_4O_{12})]\cdot 4H_2O\cdot Bpe$ compound.[56] This was probed in the cyanosilylation reaction of aldehydes with trimethylsilyl cyanide (TMSCN) under solvent-free conditions. Benzaldehyde was used to fit the best starting conditions and to establish the conditions for different aldehydes. When using aromatic aldehydes, the conversion decreases in the order *p*-methylbenzaldehyde > benzaldehyde > *p*-fluorobenzaldehyde, in agreement with their corresponding electronic effects. When using an aliphatic aldehyde such as heptaldehyde, the reaction takes place faster than when using aromatic aldehydes. The catalyst loses progressively its efficiency in successive recycling runs. X-ray diffraction and IR studies show that despite the loss of crystallinity after the reactions, the compound maintains the layered crystal structure, as well as its basic initial building blocks such as $\{V_4O_{12}\}$ cycles, metal centres and Bpe organic ligands. However, the existence of extra bands in the IR spectra suggests that the active centres are blocked progressively by cyanide groups during the catalytic reactions.

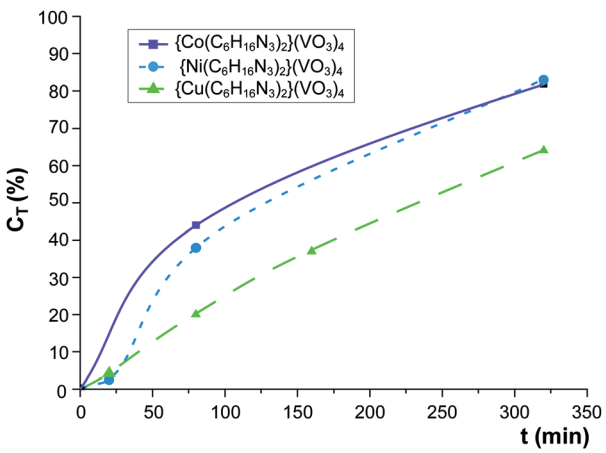

Fig. 37 Kinetic profile for the oxidation reaction of methyl phenyl sulfide with $M(HAep)_2(VO_3)_4$, M = Co^{2+}, Ni^{2+}, Cu^{2+}. Reproduced from ref. 97 with permission of The Royal Society of Chemistry.

Lin and Maggard have synthesized three silver vanadates with 4Bpy, Bpa and pyrazinedicarboxylate Pzc as ligands, whose formulas are: $[\{Ag(4Bpy)\}_4(V_4O_{12})]\cdot 2H_2O$ ($\mathbf{I^2O^1}$), $[\{Ag(Bpa)\}_4(V_4O_{12})]\cdot 4H_2O$ ($\mathbf{I^2O^2}$) and $\{Ag_4(2\text{-}Pzc)_2\}(V_2O_6)$ ($\mathbf{I^2O^3}$), respectively.[48] $[\{Ag(4Bpy)\}_4(V_4O_{12})]\cdot 2H_2O$ and $[\{Ag(Bpa)\}_4(V_4O_{12})]\cdot 4H_2O$ crystal structures are composed of neutral $\{Ag_4V_4O_{12}\}_n$ layers that are pillared by the organic ligands, 4Bpy or Bpa coordinated to the Ag(I) sites. The layers consist of isolated $\{VO_{12}\}$ rings that are linked together by eight Ag^+ cations per ring. The third compound is composed of a 3D $\{Ag_2(2\text{-}Pzc)^+\}_n$ metal–organic network that contains $\{VO_3^-\}_n$ double chains within its open channels.

On the other hand, Hu *et al.* have recently obtained a new silver(I) HV with 1,4-bis(*N*-imidazolyl)butane, Bbi, $[Ag(Bbi)][\{Ag(Bbi)\}_4\{Ag_3(V_4O_{12})_2\}]\cdot 2H_2O$.[65] The phase crystallizes in the triclinic space group $P\bar{1}$ and the most fascinating feature is the 1D chains containing $\{Ag_7\}$ clusters with Ag···Ag interactions based on dicyclic rings of $\{V_4O_{12}\}$.

All of these silver(I) vanadates show photocatalytic activity and were tested for the decomposition of methylene blue (MB) under ultraviolet and/or visible light. MB is commonly used as a representative of widespread organic dyes that contaminate textile effluents and are very difficult to decompose in waste streams. In Fig. 38, changes in the concentration of the aqueous MB solution *vs.* irradiation time under ultraviolet light are plotted. All of them are active for the decomposition of MB under UV light irradiation.

The photocatalytic rates of $\{Ag_4(2\text{-}Pzc)_2\}(V_2O_6)$ and $[Ag(Bbi)][\{Ag(Bbi)\}_4\{Ag_3(V_4O_{12})_2\}]\cdot 2H_2O$ are notably higher than those of $[Ag(4Bpy)]_4V_4O_{12}\cdot 2H_2O$ and $[\{Ag(Bpa)\}_4V_4O_{12}]\cdot 4H_2O$. $\{Ag_4(2\text{-}Pzc)_2\}(V_2O_6)$ is also active under visible light, decomposing 80% of MB after 3 h.

Some silver and manganese HV also exhibit photocatalytic properties. A synergistic effect between silver ions and vanadates allows tuning the band gap, improving their catalytic activity for the photocatalytic splitting of water or photocatalytic degradation of pollutants.

The first example of water splitting by a hybrid compound was reported recently by Luo and Maggard in $Mn(Bpy)(V_4O_{11})(Bpy)$

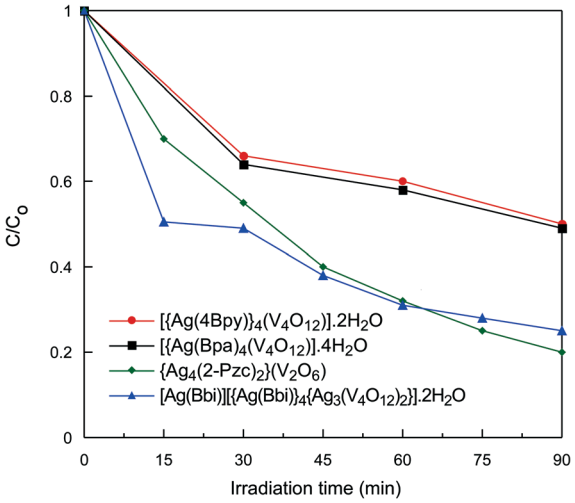

Fig. 38 Photocatalytic decomposition of MB solution under UV light with the use of hybrid silver(I) vanadates.

vanadate.[98] This compound was found to exhibit photocatalytic activity for the production of hydrogen, as well as for total water splitting into both hydrogen and oxygen. Photocatalytic tests were carried out with water in methanol solutions (Fig. 39(a) and (b)) and after coating the material with a 1% Pt co-catalyst (Fig. 39(c) and (d)). This HV is an effective photocatalyst, with production of hydrogen ranging from 16 μmol H_2 g^{-1} h^{-1} in 20% methanol solution to 71 μmol H_2 g^{-1} h^{-1} per Pt-coated samples under ultraviolet light.

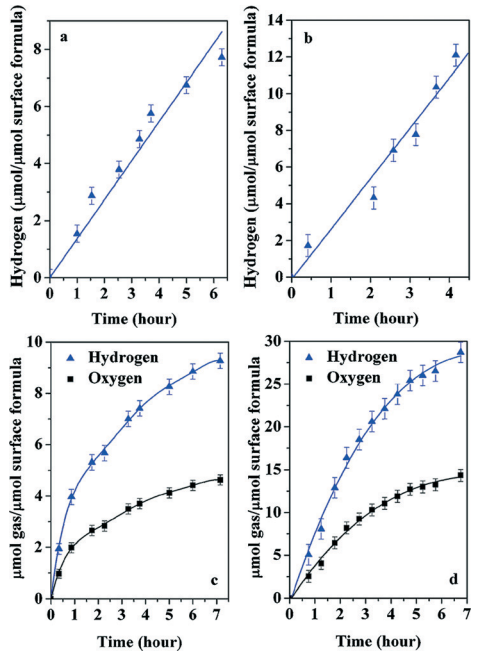

Fig. 39 Amount of hydrogen molecules per surface site of Mn(Bpy)(V_4O_{11})(Bpy) under visible light (420–800 nm) and different photocatalytic testing conditions: (a and b) with methanol as a scavenger or (c and d) with 1% Pt as a surface cocatalyst. Reprinted from ref. 98 with permission of the American Chemical Society. Copyright (2013).

Concluding remarks

The great structural diversity of transition metal hybrid vanadium oxides is clearly related to the ability of vanadium to adopt different coordination environments and to polymerize, giving rise to different vanadium structural subunits. The hydrothermal synthesis conditions influence drastically the obtained vanadium building blocks, promoting in some cases the partial or complete reduction of V^{5+} to V^{4+}. If at these points, the possibility to adopt a different coordination environment by the secondary transition metal centres, the diversity in metal–organic substructures, the rigidity/flexibility of the organic molecules, and the possibility of multiple modes of coordination for the mixed carboxylic–nitrogen donor ligands are added, the scope of possible structural archetypes becomes enormous, hindering the predictability of the obtained frameworks. But, due to these degrees of freedom, the complexity of the crystal chemistry of HV is amazing, sharing common characteristics with the classical inorganic–organic materials and present metal–organic frameworks.

Despite that the studies of the thermal responses of HV to the loss of guest and coordinated species are scarce, a great range of behaviours have been reported, mainly dependent on the crystal structures. It would be very interesting to study the thermal response of several reported HV constructed from flexible and rigid organic connectors. And more concretely, it would be very clarifying to determine the transformation mechanisms involved in the reversible removal and uptake of coordinated water molecules in HVs. Up to now, the V=O terminal bonds seems to take an important role in the formation of new metal–oxygen bonds after coordination water removal. Another possibility is to incorporate ligands with non-bonded donor atoms that could complete the coordination environment of the metal centre after the loss of coordinated species and/or metal centre that could adopt different coordination environments. Moreover, the crystal structure has to possess enough degree of flexibility to assume these strong atomic motions during the transformation.

With regard to the magnetic properties, different strategies have been proposed. The most important strategy is to obtain structural building blocks constructed from corner- or edge-sharing metal centre polyhedra, because the magnetic exchange through the VOS usually leads to AF coupling or ordering. Strategies such as mixing reduced VOS with metal centres linked through short organic linkers have allowed obtaining very interesting magnetic competitions within the same structure. A very interesting future scope could include hybrid vanadates constructed from short carboxylate ligands that could promote magnetic exchange between metal centres.

The use of short, long bipodal or multi-podal carboxylate-based ligands could enlarge greatly the crystal chemistry of this amazing family of hybrid materials, focusing on the specific properties and applications of the compounds.

A new amazing field of study is being developed by different research groups. The use of HV as catalysts and/or

photocatalysts is a very interesting research field for the green and effective degradation of pollutants. Another interesting and emerging research area is the splitting of water into H_2 and O_2, which is tested for several inorganic silver vanadates and is one of the promising fields for testing HV as new photocatalysts.

Acknowledgements

This work has been financially supported by the "Ministerio de Ciencia e Innovación" (MAT2010-15375) and the "Ministerio de Economía y Competitividad" (MAT-2013-42092-R) and the "Gobierno Vasco" (IT630-13), which we gratefully acknowledge. The authors thank the technicians of SGIker (UPV/EHU). R. Fernández de Luis thanks the MICINN (Madrid, Spain) for funding. E. S. Larrea and J. Orive thank the UPV/EHU for funding.

Notes and references

1 (*a*) A. F. Crönstedt, *Akad. Handl. Stockholm*, 1756, **17**, 120–132; (*b*) R. M. Milton, *US Pat.*, 2882243 and 2882244, 1959; (*c*) R. M. Barrer and P. J. Denny, *J. Chem. Soc.*, 1961, 971–972; (*d*) G. Férey, *C. R. Acad. Sci. Ser. IIC*, 1998, **1**, 1–13.

2 (*a*) S. T. Wilson, B. M. Lok, C. A. Messina, T. T. Cannan and E. M. Flanigen, *J. Am. Chem. Soc.*, 1982, **104**, 1146–1147; (*b*) M. Estermann, L. McCusker, C. Baerlocher, A. Merrouche and H. Kesseler, *Nature*, 1991, **352**, 320–323; (*c*) G. Ferey, *J. Fluorine Chem.*, 1995, **72**, 187–193; (*d*) S. Natarajan and S. Mandal, *Angew. Chem., Int. Ed.*, 2008, **47**, 4798–4828.

3 T. Rojo, J. L. Mesa, J. Lago, B. Bazán, J. L. Pizarro and M. I. Arriortua, *J. Mater. Chem.*, 2009, **19**, 3793–3818.

4 (*a*) Z.-E. Lin and G.-Y. Yang, *Eur. J. Inorg. Chem.*, 2010, **19**, 2895–2902; (*b*) M. E. Medina, M. Iglesias, N. Snejko, E. Gutierrez-Puebla and M. A. Monge, *Chem. Mater.*, 2004, **16**, 594–599; (*c*) N. Snejko, M. E. Medina, E. Gutierrez-Puebla and M. A. Monge, *Inorg. Chem.*, 2006, **45**, 1591–1594.

5 C. N. R. Rao, J. N. Behera and D. Meenakshi, *Chem. Soc. Rev.*, 2006, **35**, 375–387.

6 O. M. Yaghi, M. O'Keefee, N. W. Ockwig, H. K. Chae, M. Eddaoudi and J. Kim, *Nature*, 2003, **423**, 705–714.

7 P. J. Hargrman, R. C. Finn and J. Zubieta, *Solid State Sci.*, 2001, **3**, 745–774.

8 C. Janiak and J. K. Vieth, *New J. Chem.*, 2010, **34**, 2366–2388.

9 Z.-H. Yi, X.-B. Cui, X. Zhang, J. Yu, J. Lu, J.-Q. Xu, G.-D. Yang, T.-G. Wang, H.-H. Yu and W.-J. Duan, *Dalton Trans.*, 2007, 2115.

10 R. C. Finn, J. Sims, C. J. O'Connor and J. Zubieta, *J. Chem. Soc., Dalton Trans.*, 2002, 159.

11 C. M. Liu, Y.-L. Hou, J. Zhang and S. Gao, *Inorg. Chem.*, 2002, **41**, 140.

12 R. N. Devi and J. Zubieta, *Inorg. Chim. Acta*, 2003, **342**, 313.

13 P. J. Hargman and J. Zubieta, *Inorg. Chem.*, 2001, **40**, 2800.

14 C.-M. Liu, S. Gao, H.-H. Hu and Z.-M. Wang, *Chem. Commun.*, 2001, 1636.

15 (*a*) X. Qu, L. Xu, G. Gao, F. Li and Y. Yang, *Inorg. Chem.*, 2007, **46**, 4775–4777; (*b*) D. L. Long, A. J. Blake, N. R. Champness, C. Wilson and M. Schröder, *Angew. Chem., Int. Ed.*, 2001, **40**, 2443–2447.

16 M. Schindler, F. C. Hawthorne and W. H. Baur, *Chem. Mater.*, 2000, **12**, 1248–1259.

17 A. F. Wells, *Structural Inorganic Chemistry*, Clarendon Press, Oxford, 1984.

18 P. Y. Zavalij and M. S. Whittingham, *Acta Crystallogr., Sect. B: Struct. Sci.*, 1999, **55**, 627–663.

19 B. L. Ulická, F. Pavelcík and K. Huml, *Acta Crystallogr., Sect. C: Cryst. Struct. Commun.*, 1987, **43**, 2266–2268.

20 L. Shi-Xiong, L. Bi-Zhou and L. Shen, *Inorg. Chim. Acta*, 2000, **304**, 33–37.

21 D. Riou and G. Férey, *J. Solid State Chem.*, 1996, **124**, 151–154.

22 R. L. La Duca, R. S. Rarig and J. Zubieta, *Inorg. Chem.*, 2001, **40**, 607–612.

23 J. R. D. Debord, Y. Zhang, R. C. Haushalter, J. Zubieta and C. J. O'Connor, *J. Solid State Chem.*, 1996, **122**, 251–258.

24 R. L. La Duca, R. Ratkoski, R. S. Rarig and J. Zubieta, *Inorg. Chem. Commun.*, 2001, **4**, 621–625.

25 J.-Y. Xie and J.-G. Mao, *J. Mol. Struct.*, 2005, **750**, 186–189.

26 C.-M. Liu, Y.-L. Hou, J. Zhang and S. Gao, *Inorg. Chem.*, 2002, **41**, 140–143.

27 (*a*) A. K. Cheetham, C. N. T. Rao and R. K. Feller, *Chem. Commun.*, 2006, 4780–4795; (*b*) C. N. R. Rao, A. K. Cheetham and A. Thirumurugan, *J. Phys.: Condens. Matter*, 2008, **20**, 083202, (21pp).

28 (*a*) A. Thirumurugan, R. A. Sanguranath and C. N. R. Rao, *Inorg. Chem.*, 2008, **47**, 823–831; (*b*) M. J. Bialek, J. Janczak and J. Zon, *CrystEngComm*, 2013, **15**, 390–399; (*c*) T. Kurc, J. Janczak, J. Hoffmann and V. Videnova-Adrabinska, *Cryst. Growth Des.*, 2012, **12**, 2613–2624; (*d*) A. Thirumurugan, K. P. Swapan, M. A. Green and S. Natarajan, *J. Mater. Chem.*, 2003, **13**, 2937–2941.

29 I. D. Willians, T. S. Law, H. H.-Y. Sung, G.-H. Wen and X.-X. Zhang, *J. Solid State Chem.*, 2000, **2**, 47–55.

30 Z. Shi, L. Zhang, G. Zhu, G. Yan, J. Huar, H. Ding and S. Feng, *Chem. Mater.*, 1999, **11**, 3565–3570.

31 X. Wang, L. Liu, A. J. Jacobson and K. Ross, *J. Mater. Chem.*, 1999, **9**, 859–861.

32 I. D. Willians, T. S.-C. Law, H. H.-Y. Sung, G.-H. Wen and X.-X. Zhang, *Solid State Sci.*, 2000, **2**, 47–55.

33 B. F. Abrahams, M. G. Haywood and R. Robson, *Polyhedron*, 2007, **26**, 300–304.

34 G.-C. Ou, L. Jiang, X.-L. Feng and T.-B. Lu, *Dalton Trans.*, 2009, 71–76.

35 (*a*) J. Do and A. J. Jacobson, *Inorg. Chem.*, 2001, **40**, 2468–2469; (*b*) B.-Z. Lin and S.-X. Liu, *Polyhedron*, 2000, **19**, 2521–2527; (*c*) B.-Z. Lin and S.-X. Liu, *J. Chem. Soc., Dalton Trans.*, 2002, 865–869; (*d*) P. Y. Zavalij, F. Zhang and M. S. Whittingham, *Acta Crystallogr., Sect. B: Struct. Sci.*, 1999, **55**, 953–962; (*e*) Z. Shi, L. Zhang, G. Zhu, G. Yang, J. M. Hua, H. Ding and S. Feng, *Chem. Mater.*, 1999, **11**, 3565–3570.

36 Y.-Q. Jiang, Z.-H. Xu and Z.-X. Xie, *J. Coord. Chem.*, 2008, **61**, 1575–1581.

37 L.-M. Zheng, X. Wang, Y. Wang and A. J. Jacobson, *J. Mater. Chem.*, 2001, **11**, 1100–1105.
38 B. Yan, J. Luo, P. Dube, A. S. Sefat, J. E. Greedan and P. A. Maggard, *Inorg. Chem.*, 2006, **45**, 5109–5118.
39 E. S. Larrea, J. L. Mesa, J. L. Pizarro, M. I. Arriortua and T. Rojo, *J. Solid State Chem.*, 2007, **180**, 1149–1157.
40 (*a*) E. S. Larrea, Doctoral thesis, *New Transition Metal Hybrid Vanadates. Hydrothermal Synthesis, Structural Study and of their Spectroscopic and Magnetic Properties*, Universidad del País Vasco (UPV/EHU), 2009; (*b*) E. S. Larrea, J. L. Mesa and M. I. Arriortua, *Mater. Res. Bull.*, 2011, **46**, 845–849.
41 P. A. Maggard and P. D. Boyle, *Inorg. Chem.*, 2003, **42**, 4250–4252.
42 R. N. Devi, P. Rabu, V. O. Golub, C. J. O'Connor and J. Zubieta, *Solid State Sci.*, 2002, **4**, 1095–1102.
43 E. S. Larrea, J. L. Mesa, J. L. Pizarro, R. Fernández de Luis, J. Rodríguez Fernández, T. Rojo and M. I. Arriortua, *Dalton Trans.*, 2012, **41**, 14170–14179.
44 L. Yang, C. Hu, H. Naruke and T. Yanase, *Acta Crystallogr., Sect. C: Cryst. Struct. Commun.*, 2001, **57**, 799–801.
45 M. I. Khan, E. Yohannes, R. C. Nome, S. Ayes, V. O. Golub, C. J. O'Connor and R. J. Doedens, *Chem. Mater.*, 2004, **16**, 5273–5279.
46 R. Fernández de Luis, J. L. Mesa, M. K. Urtiaga, T. Rojo and M. I. Arriortua, *Eur. J. Inorg. Chem.*, 2009, 4786–4794.
47 R. Fernández de Luis, M. K. Urtiaga, J. L. Mesa, A. T. Aguayo, T. Rojo and M. I. Arriortua, *CrystEngComm*, 2010, **10**, 1880–1886.
48 H. Lin and P. A. Maggard, *Inorg. Chem.*, 2008, **47**, 8044–8052.
49 B. Yan and P. A Maggard, *Inorg. Chem.*, 2007, **46**, 6640–6646.
50 C.-D. Zhang, S.-X. Liu, L.-H. Xie, B. Gao, C.-Y. Sun and D.-H. Li, *J. Mol. Struct.*, 2005, **753**, 40–44.
51 R. Fernández de Luis, M. K. Urtiaga, J. L. Mesa, K. Vidal, L. Lezama, T. Rojo and M. I. Arriortua, *Chem. Mater.*, 2010, **22**, 5543–5553.
52 C.-C. Wang, *Acta Crystallogr., Sect. E: Struct. Rep. Online*, 2007, **63**, m2233.
53 R. Fernández de Luis, J. L. Mesa, M. K. Urtiaga, L. Lezama, L. M. I. Arriortua and T. Rojo, *New J. Chem.*, 2008, **32**, 1582–1589.
54 C.-C. Wang and C. Yin, *Z. Kristallogr. - New Cryst. Struct.*, 2008, **223**, 13–15.
55 R. Fernández de Luis, M. K. Urtiaga, J. L. Mesa, J. Orive Gómez de Segura, T. Rojo and M. I. Arriortua, *CrystEngComm*, 2011, **13**, 6488–6498.
56 R. Fernández de Luis, M. K. Urtiaga, J. L. Mesa, E. S. Larrea, T. Rojo and M. I. Arriortua, *Inorg. Chem.*, 2013, **52**, 2615–2626.
57 R. Fernández de Luis, M. K. Urtiaga, J. L. Mesa, E. S. Larrea, T. Rojo and M. I. Arriortua, *CrystEngComm*, 2012, **14**, 6921–6933.
58 R. Fernández de Luis, J. L. Mesa, M. K. Urtiaga, E. S. Larrea, T. Rojo and M. I. Arriortua, *Inorg. Chem.*, 2012, **51**, 2130–2139.
59 R. Fernández de Luis, J. Orive, E. S. Larrea, M. K. Urtiaga and M. I. Arriortua, *Cryst. Growth Des.*, 2014, **14**, 658–670.
60 X. Wang, H.-L. Hu, B.-K. Chen, G.-C. Liu and J. Li, *Z. Anorg. Allg. Chem.*, 2009, **635**, 2692–2696.
61 Y.-Q. Lan, S.-L. Li, X.-L. Wang, K.-Z. Shao, D.-Y. Du, Z.-M. Su and E.-B. Wang, *Chem. – Eur. J.*, 2008, **14**, 9999–10006.
62 X.-L. Wang, B.-K. Chen, G.-C. Liu, H.-Y. Lin and H.-L. Hu, *J. Organomet. Chem.*, 2010, **695**, 827–832.
63 Y.-F. Qi, D. Xiao, E. Wang, A. Zhang and X. Wang, *Aust. J. Chem.*, 2007, **60**, 871–878.
64 X. Wang, B. Chen, G. Liu, H. Lin, H. Hu and Y. J. Chen, *J. Inorg. Organomet. Polym. Mater.*, 2009, **19**, 176–180.
65 Y. Hu, F. Luo and F. Dong, *Chem. Commun.*, 2011, **47**, 761–763.
66 M. I. Khan, S. Deb and R. J. Doedens, *Inorg. Chem. Commun.*, 2006, **9**, 25–28.
67 L.-J. Zhang, Z.-J. Hu, Z. Zang and H.-Y. Gou, *Chin. J. Chem.*, 2007, **25**, 566–569.
68 X. Qu, L. Xu, F. Li, G. Gao and Y. Yang, *Inorg. Chem. Commun.*, 2007, **10**, 1404–1408.
69 X. Qu, L. Xu, G. Gao, F. Li and Y. Yang, *Inorg. Chem.*, 2007, **46**, 4775–4777.
70 Y.-F. Qi, C.-P. LV, Y.-G. Li, E.-B. Wang, J. Li and X.-L. Song, *Inorg. Chem. Commun.*, 2010, **13**, 384–387.
71 W. Ouellette and J. Zubieta, *Solid State Sci.*, 2007, **9**, 658–663.
72 W. Ouellette, E. Burkholder, S. Manzar, L. Bewley, R. S. Rarig and J. Zubieta, *Solid State Sci.*, 2004, **6**, 77–84.
73 R. N. Devi, P. Rabu, V. O. Golub, C. J. O'Connor and J. Zubieta, *Solid State Sci.*, 2002, **4**, 1095–1102.
74 R. S. Rarig Jr. and J. Zubieta, *Dalton Trans.*, 2003, 1861–1868.
75 P. J. Hargman, C. Bridges, J. E. Greedan and J. Zubieta, *J. Chem. Soc., Dalton Trans.*, 1999, 2901–2903.
76 J.-R. Li, Q. Yu, E. C. Sanudo, Y. Tao, W.-C. Song and X.-H. Bu, *Chem. Mater.*, 2008, **20**, 1218–1220.
77 (*a*) C.-L. Pan, J.-Q. Xu, K.-X. Wang, X.-B. Cui, L. Ye, Z.-L. Lu, D.-Q. Chu and T.-G. Wang, *Inorg. Chem. Commun.*, 2003, **6**, 370–373; (*b*) G. Li, Z. Shi, Y. Xu and S. Feng, *Inorg. Chem.*, 2003, **42**, 1170–1174.
78 T. S.-C. Law, H. H.-Y. Sung and I. D. Williams, *Inorg. Chem. Commun.*, 2000, **3**, 420–423.
79 L.-M. Zheng, T. Whitfield, X. Wang and A. J. Jacobson, *Angew. Chem., Int. Ed.*, 2000, **39**, 4528–4531.
80 J. Tao, X.-M. Zhang, M.-L. Tong and X.-M. Chen, *J. Chem. Soc., Dalton Trans.*, 2001, 700–771.
81 C.-L. Chen, A. M. Goforth, M. D. Smith, C.-Y. Su and H.-C. zur Loye, *Angew. Chem., Int. Ed.*, 2005, **44**, 6673–6677.
82 J. M. Ellsworth, M. D. Smith and H.-C. zur Loye, *Solid State Sci.*, 2008, **10**, 1822–1834.
83 J. Lu, E. Wang, J. Chen, Y. Qi, C. Hu, L. Xu and J. Peng, *J. Solid State Chem.*, 2004, **177**, 946–950.
84 D. Xiao, E. Wang, H. An, L. Xu and C. Hu, *J. Mol. Struct.*, 2004, **707**, 77–81.
85 D. Xiao, Y. Xu, Y. Hou, E. Wang, S. Wang, Y. Li, L. Xu and C. Hu, *Eur. J. Inorg. Chem.*, 2004, 1385–1388.
86 (*a*) R. N. Devi and J. Zubieta, *Inorg. Chim. Acta*, 2002, **3 38**, 165–168; (*b*) L.-M. Zheng, J.-S. Zhao, K.-H. Lii, L. Y. Zhang, Y. Liu and X.-Q. Xin, *J. Chem. Soc., Dalton Trans.*,

1999, 939–943; (*c*) C. Sun, E. Wang, D. Xiao, H. An and L. Xu, *J. Mol. Struct.*, 2007, **840**, 53–58; (*d*) D. Xiao, Y. Hou, E. Wang, Y. Li, J. Lu, L. Xu and C. Hu, *J. Mol. Struct.*, 2004, **691**, 123–131; (*e*) S. Natarajan, *Inorg. Chim. Acta*, 2003, **348**, 233–236.

87 Y. Lu, E. Wang, M. Yuan, Y. Li, L. Xu, C. Hu, N. Hu and H. Jia, *Solid State Sci.*, 2002, **4**, 449–453.

88 C.-M. Liu, D.-Q. Zhang, M. Xiong, M.-Q. Dai, H.-M. Hu and D.-B. Zhu, *J. Coord. Chem.*, 2002, **55**, 1327–1335.

89 R. Fernández de Luis, M. K. Urtiaga, J. L. Mesa, T. Rojo and M. I. Arriortua, *J. Alloys Compd.*, 2009, **480**, 54–56.

90 (*a*) J. Livaje, *Coord. Chem. Rev.*, 1998, **178**, 999–1018; (*b*) L. Bouhedja, N. Steunou, J. Maquet and J. Livage, *J. Solid State Chem.*, 2001, **162**, 315–321.

91 T. Chirayil, P. Y. Zavalij and M. S. Whittingham, *Chem. Mater.*, 1998, **10**, 2629–2640.

92 K. K. Nanda, L. K. Thompson, J. N. Bridson and K. J. Nag, *J. Chem. Soc., Chem. Commun.*, 1994, 1337–1341.

93 M. H. Zeng, B. Wang, X. Y. Wang, W. X. Zhang, X. M. Chen and S. Gao, *Inorg. Chem.*, 2006, **45**, 7069–7076.

94 (*a*) J. Cano, G. De Mundo, J. L. Sanz, R. Ruiz, J. Faus, F. Loret, M. Julve and A. Caneschi, *J. Chem. Soc., Dalton Trans.*, 1997, 1915–1924; (*b*) P. Vitoria, J. M. Gutiérrez-Zorrilla, A. Luque, P. Román, L. Lezama, F. J. Zuñiga and J. I. Beitia, *Inorg. Chem.*, 2003, **42**, 960–969.

95 (*a*) R. A. Shiels, K. Venkatasubbaiah and C. W. Jones, *Adv. Synth. Catal.*, 2008, **350**, 2823; (*b*) A. Zhang, J. Zhang, N. Cui, X. Tie, Y. An and L. Li, *J. Mol. Catal. A: Chem.*, 2009, **304**, 28; (*c*) D. E. Katsoulis, *Chem. Rev.*, 1998, **98**, 359; (*d*) G. Centi and F. Trifiro, *Appl. Catal., A*, 1996, **143**, 3; (*e*) Y. Idota, *Eur. Pat.*, 0 567 149 A1, 1993; (*f*) M. S. Whittingham, *J. Electrochem. Soc.*, 1976, **123**, 315; (*g*) S. Denis, E. Baudrin, F. Orsini, G. Ouvrard, M. Touboul and J.-M. Tarascon, *J. Power Sources*, 1999, **81–82**, 79; (*h*) Y. Ueda, *Chem. Mater.*, 1998, **10**, 2653; (*i*) L. Liu, X. Wang and A. J. Jacobson, *J. Mater. Res.*, 2009, **24**, 1901.

96 (*a*) M. Weyad, H. J. Hecht, M. Kiess, M. F. Liaud, H. Vilter and D. Schomburg, *J. Mol. Biol.*, 1999, **293**, 595; (*b*) J. N. Carter-Franklin, J. D. Parrish, R. A. Tchirret-Guth, R. D. Little and A. Butler, *J. Am. Chem. Soc.*, 2003, **125**, 3688; (*c*) D. Rechder, G. Santoni, G. M. Licini, C. Schilzke and B. Meier, *Coord. Chem. Rev.*, 2003, **237**, 53.

97 E. S. Larrea, J. L. Mesa, J. L. Pizarro, M. Iglesias, T. Rojo and M. I. Arriortua, *Dalton Trans.*, 2011, **40**, 12690.

98 L. Luo and P. A. Maggard, *Cryst. Growth Des.*, 2013, **13**, 5282–5288.

